Flame-sprayed Al-12Si Coatings as Damage Detection Sensors for Fibre-Reinforced Polymer Composites

by

Raelvim Gonzalez Henriquez

A thesis submitted in partial fulfillment of the requirements for the degree of

Doctor of Philosophy

in

Engineering Management

Department of Mechanical Engineering
University of Alberta

ABSTRACT

In this thesis, a characterization of flame-sprayed aluminium-12silicon (Al-12Si) coatings as an electrical structural health monitoring (SHM) sensor for fibre-reinforced polymer composite (FRPC) structures is presented. Flame-sprayed Al-12Si coatings were deposited onto FRPC tubes and laminates. The effect of the flame-sprayed Al-12Si coating on the failure behaviour of FRPC tubulars was evaluated by internal pressurization tests with hydraulic oil, and mitigation of the mechanical degradation effects due to the flame spray deposition on the performance of FRPC tubes was achieved. The application of the classical laminate model to describe the mechanical behaviour of flame spray coated FRPC laminates under uniaxial loads was evaluated considering the flame-sprayed Al-12Si coating as an isotropic lamina. An electrical SHM sensor for uniaxial FRPC structures was developed based on the changes of electrical behavior of the porous Al-12Si coatings under applied load. Tensile tests were performed on cross-ply and unidirectional coated FRPC laminates to evaluate the electromechanical response of the flame-sprayed SHM sensor (FS SHM sensor). The development of a descriptive framework for damage detection in FRPC laminates based on electrical resistance change was accomplished in tandem with the analysis of the cost structure of the proposed FS SHM sensor at the current development stage. The characterization of flame-sprayed Al-12Si coatings as electrical SHM sensors provided a macroscopic description of the electro-mechanical behaviour of the novel metal-FRPC structure and established the limitations to structural damage detection induced by strain. Further technical improvements in the sensitivity of the FS SHM sensor to detect matrix damage at low strain level may be realized by considering the effect of microstructural porosity and morphology on the electrical properties of the Al-12Si coating. The economic analysis of the proposed FS SHM sensor revealed the relatively high cost-effectiveness of this approach to damage detection in FRPC structures and assessed the initial and operational cost factors required for potential technology development and competitive implementation of the proposed FS SHM sensor in uniaxial FRPC structures.

PREFACE

Chapter 2 of this thesis document includes output from research collaborations from Mr. Sayed Hossein Ashrafizadeh in the sections on surface preparation methods of polymer-based substrates and thermal spray process parameters. Also, Mr. Adrian Lopera-Valle was a collaborator in the research conducted on potential thermal system applications of thermal-sprayed metal coatings deposited on polymer-based substrates. The purpose of the collaboration was to enable the drafting of a review article on the thermal spray metallization of polymer-based materials.

The work presented in the Chapter 3 of this thesis document has been published in a peer-reviewed journal as:

- R. Gonzalez, A. McDonald, P. Mertiny, Effect of flame-sprayed Al-12Si coatings on the failure behaviour of pressurized fibre-reinforced composite tubes, Polym. Test. 32 (8) (2013) 1522-1528.

Mr. Garrett Melenka provided technical assistance and conducted digital image correlation analysis as part of the work presented in Chapter 4. The research study presented in the Chapter 5 of this thesis document has been published in peer-reviewed conference proceedings as:

- R. Gonzalez, P. Mertiny, A.G. McDonald, Damage detection framework for fiber-reinforced polymer composites using Al-12Si flame-sprayed coatings, in: CANCOM 2015 Conference, Edmonton, AB, Canada, 2015, pp. 1 -8.

Equipment operation for FRPC experimental tests presented in Chapter 3, 4, and 5 was accomplished with assistance from technician Mr. Bernie Faulkner of the Machine Shop in the Department of Mechanical Engineering. In conducting the economic analysis presented Chapter 6, Dr. Christopher Dennison and Mr. Robert Butz provided guidance and technical assistance with the experimental apparatus of the Fibre Bragg grating sensor and Dr. Peter Flynn was involved with the cost model formulation and manuscript composition.

All authors contributed to the development of the aforementioned papers. I conducted the research work under the guidance of Dr. Pierre Mertiny and Dr. André McDonald in their roles as research supervisors.

ACKNOWLEDGEMENTS

This work would not have been possible without the support and guidance of my supervisors, Dr. Pierre Mertiny and Dr. André McDonald. I am appreciative of their supervision and counsel in managing this research project. Also, I would like to recognize Dr. Ben Jar, Dr. Christopher Dennison, and Dr. Peter Flynn for taking the time to meet with me and provide excellent advice.

I acknowledge professors, friends, and colleagues in the department of Mechanical Engineering at the University of Alberta for instilling in me the thirst for knowledge. Special thanks to Mr. Bernie Faulkner in the Machine Shop of the Department of Mechanical Engineering for technical support and motivation. In addition, I would like to express my gratitude towards my patient wife Elena for being supportive of my decision to further my education and offering endless encouragement.

RGH

TABLE OF CONTENTS

LIST OF TABLES

LIST OF FIGURES

Chapter 1 Introduction

1.1 Background and motivation

Fiber-reinforced polymer composite (FRPC) structures consist of reinforcing fibres embedded in a polymer matrix, as shown in Fig. 1.1 [1]. This material configuration can provide enhanced mechanical properties (i.e., high specific strength, high specific stiffness) with respect to single-phase structures (e.g., metals). The reinforcing fibre in FRPC structures is usually the phase with the highest mechanical strength. Under increasing loads, matrix failure often precedes fibre failure in the FRPC. As a result, the FRPC may exhibit multi-stage failure features and withstand higher loads beyond initial damage and loss of matrix integrity.

In engineering applications, FRPC structures are used increasingly to improve load-bearing performance and reduce long-term maintenance costs. Examples of structural applications of FRPC materials include airfoils and oil/gas pipes [2-4]. Although FRPC materials can be utilized to provide high specific strength, high specific stiffness, and enhanced corrosion resistance to structures, early damage detection represents an obstacle to their wider adoption in industrial sectors where abrasive wear and cracking is problematic [5-8]. Structural Health Monitoring (SHM) is the process of implementing a non-destructive damage assessment for infrastructure integrity [9]. Two different stages are identified in a SHM system: (i) Continuous damage detection on demand (Diagnosis), and (ii) Damage assessment and management (Prognosis). This work is focused on the first stage of the SHM system, considering the development and characterization of a damage detection sensor for FRPC structures.

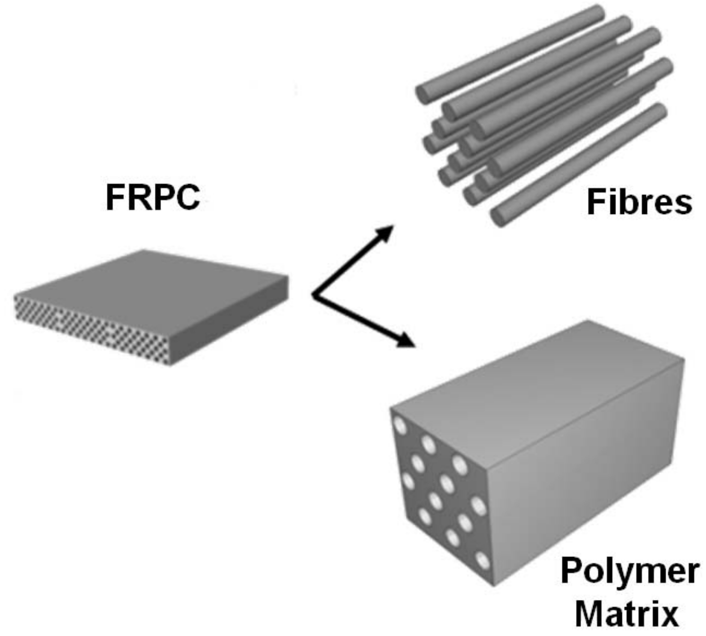

Figure 1.1: Schematic of a FRPC material phases: a) fibres and b) matrix [Adapted from: [1]]

Damage detection in a FRPC structure is relatively complex due to the anisotropy exhibited in the fibre-matrix ensemble [10] and the limited availability of long-term data on the mechanical behaviour of in service components. Also, cumulative structural damage in FRPC structures may affect their mechanical performance and total life cycle cost [11]. Although several non-destructive techniques have been developed for damage detection in FRPC structures, including ultrasonic scanning, X-radiography, and pulsed thermography [12], these methods are not suitable for remote real-time monitoring due to the prohibitive cost and technical requirements for constant implementation or deployment onsite, or both. Improving damage detection range and system economics has been the focus of previous studies on non-destructive inspection methods for FRPC materials [13, 14]. Distinctively, SHM systems provide continuous damage assessment of the FRPC structure [9], rather than localized structural testing on a scheduled basis.

Currently, proposed electrical SHM systems for FRPC structures are based on signal transmission using either the matrix or the fibres as the conductive medium. Electrical signal transmission through the fibres of a FRPC (i.e., carbon fibres or optical fibres) is conditioned by: (i) the properties of the reinforcing fibres and their orientation and (ii) the density of the fibres within the matrix. As a result, multiple local sensors may be required to detect matrix damage in FRPC structures [15], and functional failure detection may be hindered in some FRPC structures in which the fibres remain intact under initial damage conditions (i.e., leakage in FRPC pressure vessels and pipes due to matrix cracking). In contrast, matrix-based signal transmission methods have been developed to detect damage in FRPC structures using electrically conductive fillers mixed in the polymer matrix (i.e., carbon nanotubes) [3, 16]. However, the electrical conductivity of the resulting polymer matrix (~10^{-2} S/m) is several orders of magnitude lower than that of metals (~10^{7} S/m), which significantly reduces electrical signal transmission efficiency and range, and increases power consumption and operating costs.

The deposition of an electrically conductive layer may allow a novel approach for damage detection in the FRPC structure, provided that strain in the FRPC substrate affects the conduction of charge through the conductive coating. To that end, the use of thermal spray processes to deposit metal coatings onto polymer-based materials has received increasing attention in recent years [17-21]. Thermal spraying encompasses a group of coating processes in which a heat source is used to melt and accelerate powdered particles, prior to their deposition onto component substrates, as shown in Fig. 1.2 [22]. As a result of the high-temperature thermal deposition process, mechanical degradation of the FRPC substrate may occur. Three types of residual thermal stresses have been identified due to thermal spray deposition: (i) tensile quench stress from rapid cooling during solidification of the powdered particles; (ii) compressive peening stress due to impact of the high-velocity spray particles; and (iii) thermal mismatch due to the relative difference in heat transfer and thermal expansion properties between the coating and the substrate [23].

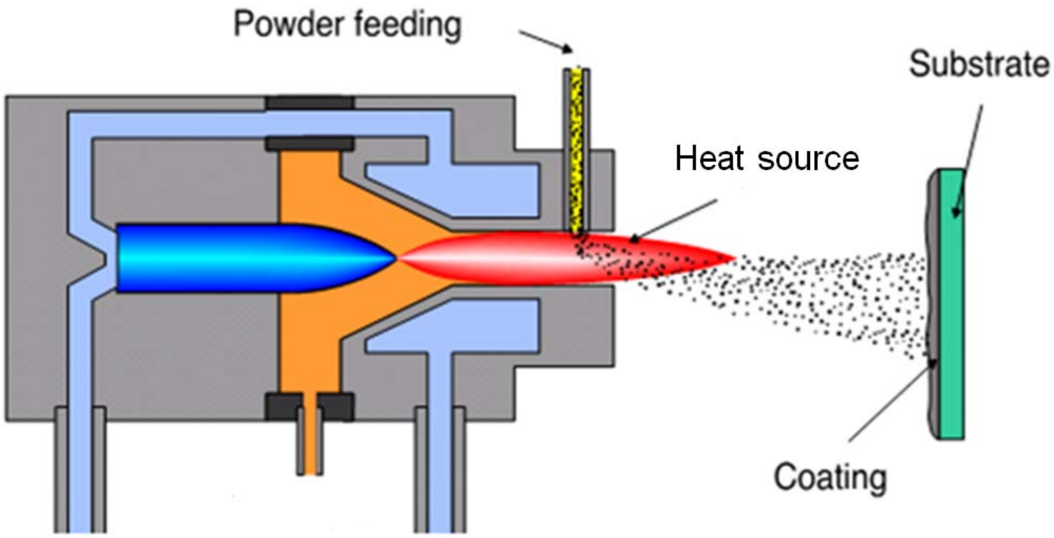

Figure 1.2: Schematic of the thermal spray process [Adapted from: [22]]

While high-temperature thermal spray processes such as plasma spraying have been investigated for creating metal coating-polymer structures [24, 25], limited studies are available that focus on the deposition of metals onto FRPC structures using lower temperature and lower cost thermal spraying processes, such as flame spraying [26]. Flame spraying is an additive manufacturing process in which the combustion of gaseous fuels produces a flame that melts and accelerates powder particles for coating deposition. A picture of the flame spray process is shown in Fig. 1.3.

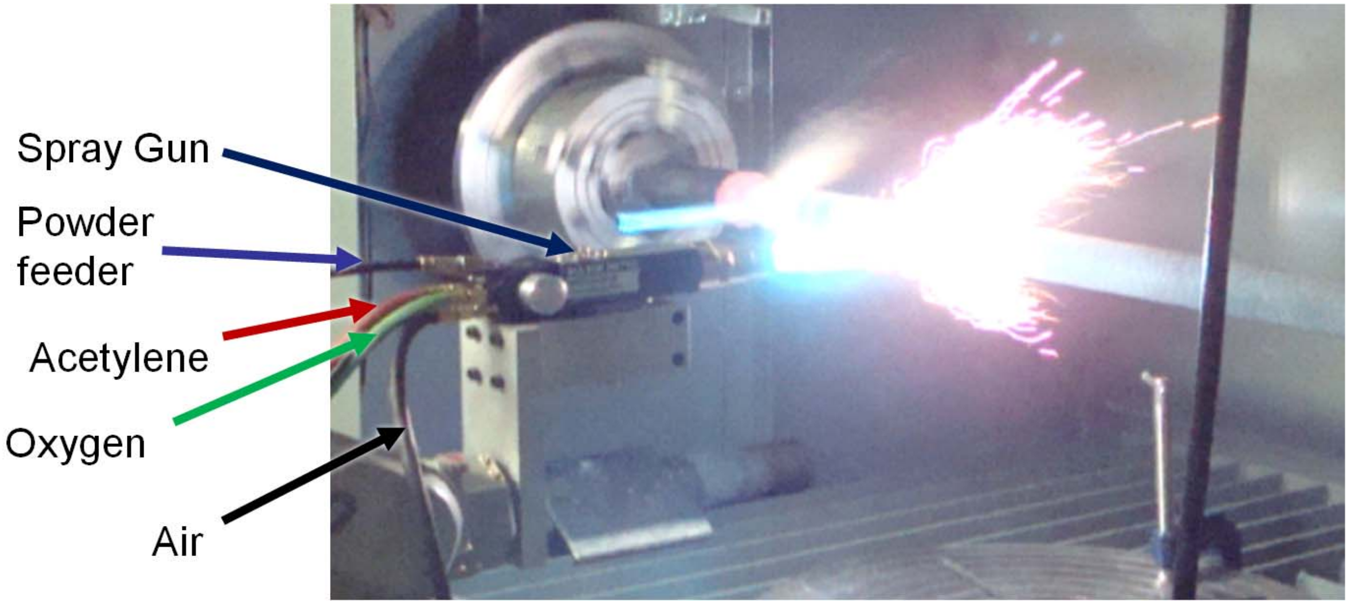

Figure 1.3: Flame spray deposition of a metal coating onto a FRPC pipe

Thermal-sprayed metal coatings can provide functional advantages to FRPC structures, such as customized electrical and thermal conduction properties in airfoil deicing systems [17, 27] and electrically conductive FRPC pipes [19]. However, scant literature exists on the electrical characterization of the resulting metal-FRPC structure [17-19]. Currently, limited studies describe the ability of thermal-sprayed coatings to conduct electrical charges, and no comprehensive study exists on the potential functional applications of this approach, such as in structural health monitoring of FRPC substrates.

Structural heath monitoring of FRPC structures using functional flame-sprayed metal coatings constitutes a novel and state-of-the-art approach to non-destructive inspection methods for detecting in-service damage. Furthermore, the use of the flame spraying process exerts a relatively low thermal load on FRPC substrates, in comparison to other high-temperature deposition processes (i.e., plasma spraying) [26], and provides flexibility to deposit metal coatings in various patterns and dimensions. The fabrication of damage detection SHM sensors for FRPC substrates via electrical signals through flame-sprayed metal coatings was first suggested by Huonnic, *et al.* [19], in which low melting point aluminium coatings were deposited and characterized in terms of electrical resistance. Flame-sprayed aluminium-12silicon (Al-12Si) represents an alternative material system for electrical applications and exhibits a lower melting temperature (577°C) compared to that of pure aluminium (660°C), which can limit matrix decomposition and mechanical degradation in FRPC substrates [28, 29]. With these characteristics, a SHM sensor using flame-sprayed Al-12Si coatings deposited onto FRPC structures shows potential advantages for adaptable and non-localized damage detection using electrical signals. In addition, the relative portability and low electric power requirements of the flame spray system can facilitate the fabrication of the SHM sensor on-site, in contrast with more energy-intensive thermal spray technologies, such as electric arc, plasma, or cold spraying. Therefore, the characterization of flame-sprayed Al-12Si coatings as an electrical conductor for damage detection in FRPC substrates and the investigation of the economics of this approach constitute a novel and unique research development, and may provide a potentially cost-effective solution to meet SHM requirements in metal-FRPC structures. The illustration of this research concept is shown in Fig. 1.4.

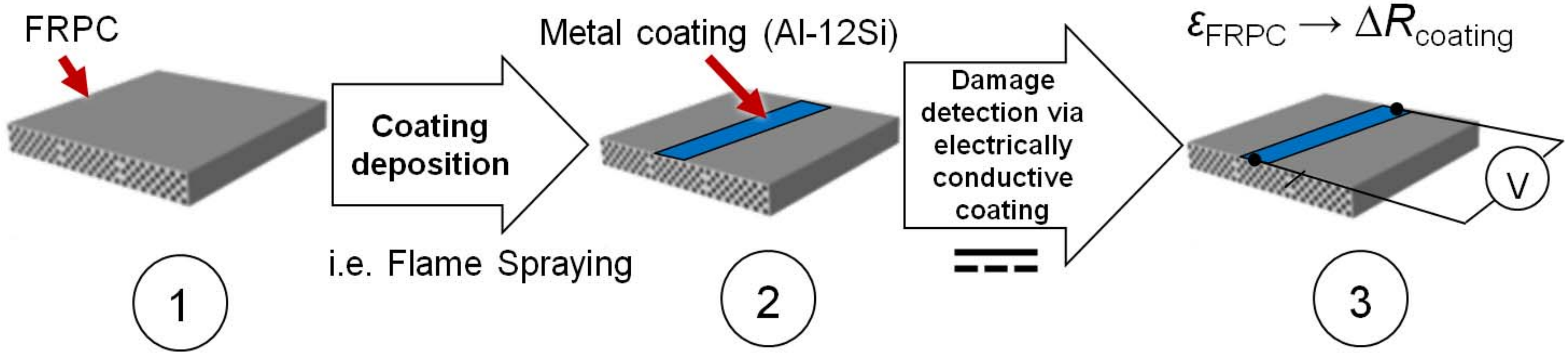

Figure 1.4: Research concept for a SHM sensor based on the electrical resistance changes of flame-sprayed Al-12Si coating (ΔR) due to axial strain in the FRPC substrate ($\varepsilon_{\mathrm{FRPC}}$)

1.2 Objectives

The objectives of the research project presented in this thesis document were to:

1. Develop a methodology to deposit flame-sprayed Al-12Si coatings onto FRPC substrates.
2. Evaluate the effect of flame spray deposition of Al-12Si coatings on the leakage behaviour of as-sprayed FRPC tubes.
3. Characterize the mechanical behaviour of flame spray coated FRPC laminates under axial strain and the mechanical properties of the Al-12Si coating.
4. Develop a damage detection SHM sensor based on flame-sprayed Al-12Si coatings deposited onto uniaxial FRPC structures.
5. Evaluate the potential to perform damage detection in uniaxial FRPC laminates by monitoring the change in electrical resistance of flame sprayed Al-12Si coatings under applied axial strain.
6. Perform an economic analysis of the potential flame-sprayed SHM sensor.

1.3 Organization of the thesis document

The structure of the present thesis document includes several chapters, which consist of the specific methodology developed to deposit flame-sprayed

Al-12Si coatings onto FRPC specimens. Following the Introduction in Chapter 1, Chapter 2 provides a literature review of thermal spray metal deposition onto FRPC substrates. Chapter 3 presents the evaluation of the effects of flame-sprayed Al-12Si coatings on the leakage behaviour of FRPC tubes. Chapter 4 includes the application of the classical laminate model to characterize the mechanical behaviour of flame spray coated FRPC structures for axial loads. Chapter 5 includes the development of a damage detection framework for uniaxial FRPC structures using flame-sprayed Al-12Si coatings. The economic analysis of the developed flame-sprayed SHM sensor is presented in Chapter 6. Finally, Chapter 7 presents the conclusions and proposed future work that may be extended from this research project.

Chapter 2 Review of Thermal Spray Metallization of Polymer based Structures*

2.1 Introduction

Thermal spraying is a material deposition process whereby a heat source is used to increase the temperature of feedstock particles that are accelerated in a fluid stream through a spray nozzle or torch, for consolidation upon impact on a substrate. The thermal spray deposition process is characterized by heat, mass, and momentum transfer phenomena [30-32]. These phenomena are functions of the thermal spray process parameters [31] and affect the properties and structure of the resulting thermal-sprayed coatings [30]. The thermal energy is transferred from the thermal spray gas, flame, or plasma to the substrate by gas convection and the impingement of solid or molten particles [26]. The kinetic energy of the impacting particle is used to overcome surface tension energy, deform the particles, and/or is converted to heat due to viscous dissipation or adiabatic shear instabilities during flattening to form a splat [33-35]. As a result of the thermal

---

* A version of this chapter is scheduled for submission to *Surface and Coatings Technology* in September 2015.

spray deposition onto the substrate, a lamellar structure of splats develops into a coating layer, which exhibits different physical properties from those of the coating bulk material [30]. These differences in properties can be the result of phase changes during the deposition process, residual stresses in the solidified splats, and the presence of porosities and other microstructural defects within the coating [36]. Thermal spray deposition has been performed using different particle-substrate material systems, including metal particle and polymer-based substrates [26, 31, 37-40].

Thermal spray deposition of metal particles onto polymer-based structures has gained increasing attention through studies on the metallization of fibre-reinforced polymer composite (FRPC) [17-19, 41-43], polymer matrix composite (PMC) [44, 45], and thermoset substrates [21, 46-50]. Even though polymer-based materials have high specific strength and corrosion resistance [5, 42], potential flammability [51, 52], low operational temperatures [42], and electrical conductivity limit their applicability in industry. The deposition of metal particles onto polymer-based substrates has been investigated to improve the thermal and electrical properties of the resulting metal-polymer system [19, 27, 45, 46, 53, 54]. Thermal-sprayed metal coatings can be engineered to provide friction coefficient adaptation, dimensional control, dimensional restoration, and enhanced electromagnetic and thermal properties to polymer-based substrates in service [31, 36, 42]. Also, the thermal spray process allows deposition of coatings on to various substrate geometries and the ability to recoat damaged coatings [26].

However, thermal degradation of the polymer-based substrate and formation of char may occur, and depends on the temperature of the metal particles and high-temperature gases during thermal spray deposition [29].

The objective of this chapter is to present a review of the current knowledge of the thermal spray deposition of metals onto polymer-based substrates and the potential applications of the metal-polymer ensemble structure. The concepts associated with the thermal spray process technology for coating deposition onto polymer substrates, including, surface preparation, temperature distribution, evaluation and characterization of metal coatings deposited onto polymer-based substrates will be discussed.

2.2 Process description and technologies

2.2.1 Thermal spray metallization of polymer based structures

Thermal spray metallization of polymer-based structures is defined as the application of thermal spray processes to deposit metals onto a polymer substrate. Thermal spray deposition can be accomplished by embedment or adhesion of metal particles onto the polymer-based substrate in the form of deformed splats, as illustrated in Fig. 2.1 [55]. The deposition of the metal splats is affected by the velocity and temperature of the impacting particles, the roughness and temperature of the substrate surface, and the relative angle between the particle trajectory and the substrate [26, 36], among others. The deposited metal particles may embed into relatively softer polymer substrates, such as nylon, polyurethane, and polyethylene [46, 56, 57]. Alternatively, the particles may deform and interlock upon contact with the polymer substrate surface, as shown in previous studies involving epoxy [19, 41] and pre-treated polyurethane [43].

The microstructure and physical properties of metal coatings deposited onto polymers are influenced, in part, by the kinetic energy of the sprayed particles and the temperature of the fluid stream in which the deposited particles were entrained, which is usually a gas [31, 37]. Current thermal spray metallization processes of polymer-based substrates can be classified into four categories according to the primary energy source used for particle acceleration and heating [31, 32, 58]. They are (i) cold spraying, which consists of kinetic-based deposition of metal or metal alloy particles at relatively low temperatures, (ii) flame spraying, comprising particle deposition using a combustion flame jet, (iii) electric arc wire spray, which utilizes an electric discharge from electrodes around a carrier gas stream to generate a thermal jet, and (iv) plasma spraying, involving ionized gas jets generated by either direct current (DC) or radio-frequency (RF) current. Each of the thermal spray processes will generate different magnitudes of energy in the fluid that is used to heat and accelerate the particles for deposition. Figure 2.2 shows the approximate range of gas temperature and particle impact velocity of different thermal spray metallization processes [26, 31].

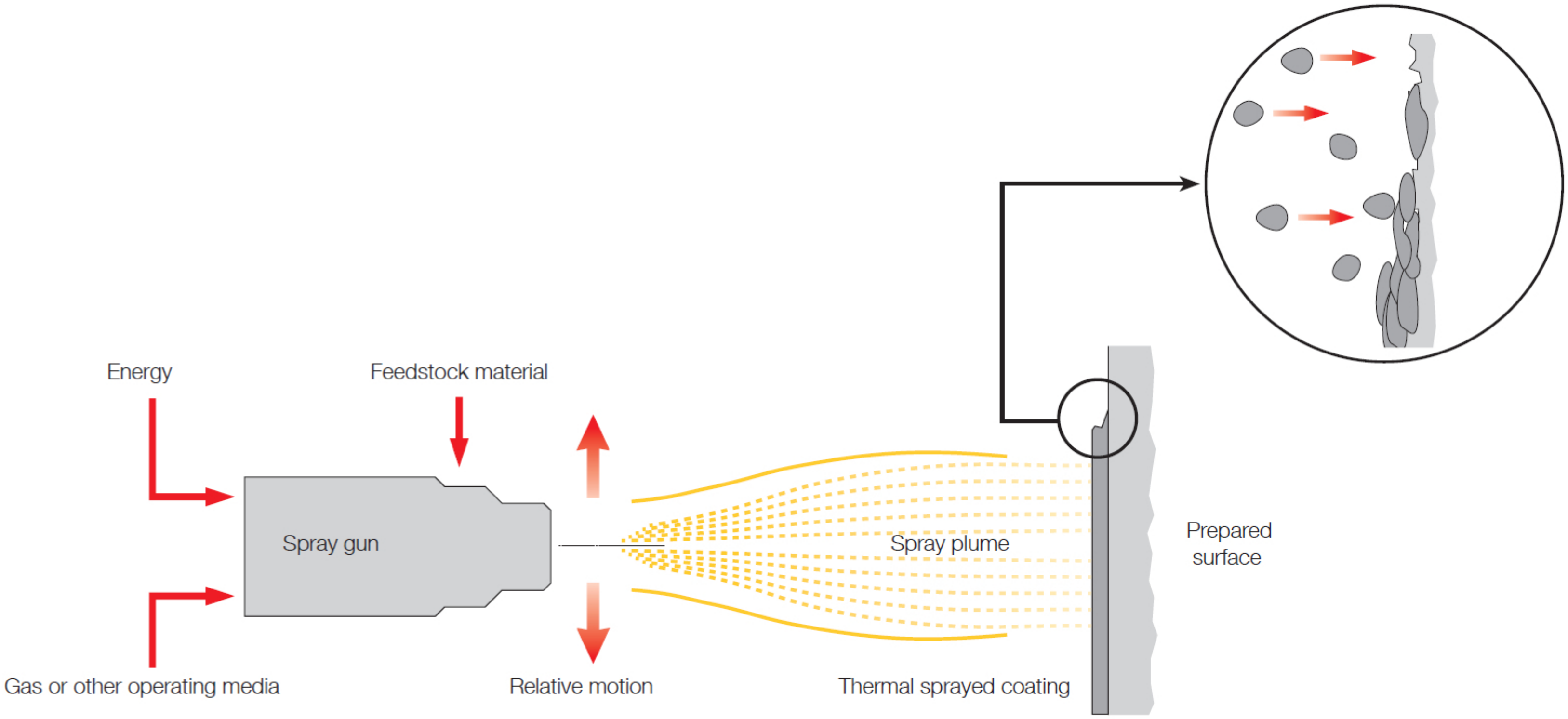

Figure 2.1: Schematic of the thermal spray process [55]

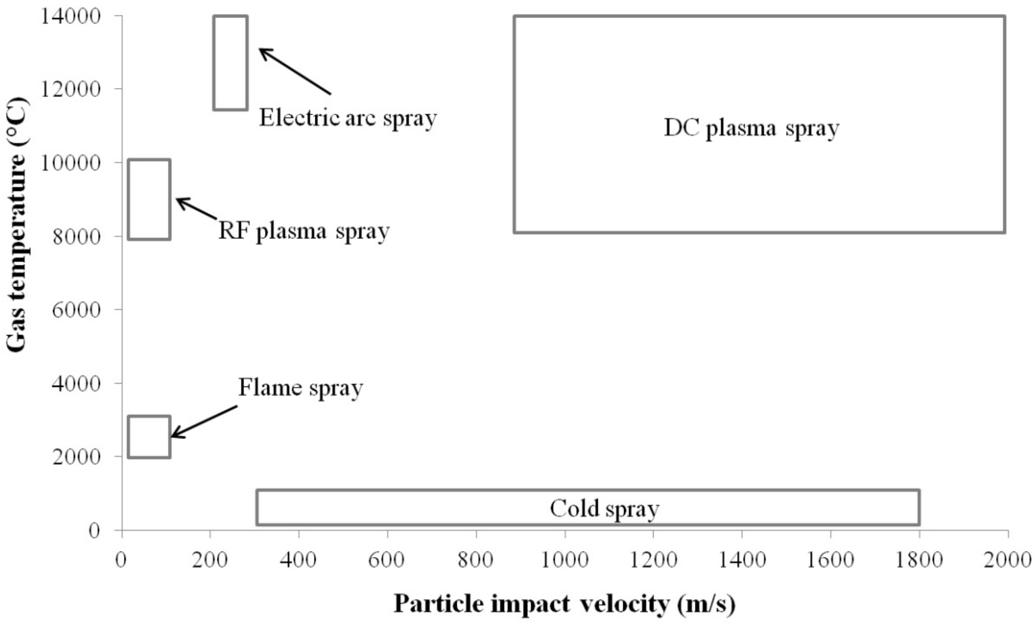

Figure 2.2: Gas temperature and particle impact velocity map of several thermal spray metallization processes [26, 31]

2.2.2 Cold spraying

Cold spraying is a relatively low-temperature thermal spray process where solid-state particles are accelerated through a nozzle to high velocities (300 – 1200 m/s), and the coating is formed as a result of plastic deformation and interlocking of the deformed particles upon impact [31, 37]. Cold spray deposition is predominantly based on using the kinetic energy of the impacting particles to promote solid-state plastic deformation and adiabatic shear instability heating, since melting of the feedstock powder material does not occur. However, softening of the impacting particles may develop due to the temperature rise upon impact and deformation of the ductile metal particles [34, 35]. Cold-sprayed particles deform plastically upon impact on the substrate at a critical velocity that overcomes rebounding and substrate erosion and produces adhesion [37, 46, 56]. The process parameters of the cold spray process include nozzle geometry, nozzle stand-off distance (distance between the nozzle and the substrate surface), feedstock material, and carrier gas temperature and pressure. Cold spraying is typically performed using a convergent–divergent De Laval nozzle [37], which accelerates the carrier gas stream to high velocity through expansion of compressed gases.

Although the mechanism of cold spray deposition on polymers is a topic of active research, cold spray metallization has been achieved on polymer-based materials [37]. Cold spray metallization of polymers has been found to be suitable for ductile metals with relatively low melting temperature and mechanical strength such as aluminium (Al) and tin (Sn) [37, 44, 59, 60]. The limited thermal energy required in the cold spray metallization of polymers may forestall potentially deleterious effects in as-sprayed parts, such as the accumulation of residual thermal stresses, metal oxidation, and undesired chemical reactions [37, 61]. As a result, cold-sprayed metal coatings may be suited for applications related to surface protection [17, 62] and engineering [37, 46-48, 59] of temperature-sensitive polymer structures with low heat capacity. On the other hand, limited heating of the powder particles by the carrier gas can increase the plasticity of the metal particles [46], which would, in turn, reduce the critical velocity required for cold spray deposition and particle adhesion [37]. Alternatively, previous studies have used low temperature to promote cold-spray deposition of Al onto polyamide 66 (PA66) [47], copper (Cu) onto polyvinyl chloride (PVC) [21], Al onto polycarbonate [49], titanium onto polyetheretherketone (PEEK) [48], and Al onto 30% carbon fibre-reinforced polyetheretherketone (PEEK 450CA30) substrates [44].

Based on the gas flow velocity during the spray deposition process, three types of cold spray processes can be used for metallization of polymers [17, 31, 37, 60]:

a) Low-pressure cold spray (LPCS), in which the gas pressure is below 1 MPa and the particle velocities usually range between 300 and 600 m/s [37]. The lower kinetic energy of the particles in the LPCS process can reduce the deposition efficiency of the metallization process since critical velocities of the impacting particles may not be achieved [31, 63]. In general, the thermal spray deposition efficiency is determined as the ratio between the weight of the deposited material and feedstock particles sprayed in a given time [64, 65].
b) High-pressure cold spray (HPCS), in which a carrier gas with low molecular weight such as nitrogen or helium is utilized and particles velocities are between 800 and 1400 m/s [31, 37]. Typical upstream gas pressures range between 1 and 4 MPa [31, 37, 59].

c) Pulsed gas dynamic spraying, in which the carrier gas stream oscillates by way of a series of fixed-frequency shock waves [66]. The shock waves propagate abrupt increments of pressure and temperature in the carrier gas stream that are higher than those of conventional cold spray systems, which produces impacting particles with higher velocities [37].

The higher kinetic energy of cold-sprayed metal particles can also induce structural damage to the polymer-based structures at the expense of coating fabrication. Robitaille *et al.* [17] reported limited substrate damage as a result of the deposition of zinc (Zn) coatings onto exposed carbon fibre/epoxy composites using the pulsed-gas dynamic cold spray process. In another study, erosion of polyamide-6 and PMC substrates was observed as a result of cold spray deposition of Cu particles at high pressure [59].

Alternatively, HPCS has been used to embed metal particles into polymer-based substrates without the formation of a continuous coating. Embedment of Cu particles deposited into polyurethane and high density polyethylene (HDPE) substrates has shown potential for antifouling applications [46, 56, 57]. Cold-sprayed embedment studies reported to date have utilized Cu deposition particles and thermoplastic substrates, with carrier gas temperature that ranges between 100 and 400°C.

2.2.3 Flame spraying

Flame spraying is a thermal spray process in which the combustion of fluid fuels produces a flame jet that melts and accelerates the feedstock material for deposition onto the substrate. The combustion gases are usually acetylene and oxygen, though air may also be added for cooling purposes [39]. The feedstock particles are propelled toward the substrate through a nozzle by the flow of a carrier gas, which is usually an inert gas such as argon. The feedstock material can be in the form of powder, wire, rod, or cord. The flame temperature should be sufficiently high to ensure the melting of the feedstock material [31]. The flame spray process usually exhibits gas temperatures between 2000 and 3000°C [26, 67], whereas the particle impact velocity is usually below 100 m/s [31]. The flame spray process parameters include nozzle geometry, nozzle stand-off distance from the substrate, carrier gas pressure, feedstock material, and combustion gas flow ratio.

Previous studies [42, 68] have shown that flame-sprayed metal coatings can provide functional advantages to polymer-based structures. These functional advantages include enhancement of electrical and thermal conduction properties. Although the flame spray process has been identified as a relatively inexpensive thermal spray metallization process for polymers [42], the flame-sprayed metal coatings contain levels of higher porosity and, therefore, lower mechanical strength compared to those coating deposited by cold and plasma spraying [26].

Consequently, deposition by flame spraying may require careful execution and optimization of spray parameters to develop suitable and cost-effective functional metal coatings on polymer-based structures. Flame spray deposition of metal coatings onto polymer-based substrates is constrained by the sensitivity of the substrate to the impact of high–temperature, semi-molten, and molten particles [54]. In addition, heat transfer studies indicate that a significant thermal load can be exerted during flame spray metal deposition on to polymer-based substrates [43].

Flame spray metallization of polymer-based substrates has been investigated using Al and aluminium-12silicon (Al-12Si) powders, the latter consisting of 88 wt.% aluminium and 12 wt.% silicon. Voyer *et al.* [20, 54] showed that the surface conductivity of Al coatings deposited onto polyester textile substrates increased proportionally to the coating thickness, while the flexibility of the polymer fabric was retained and was unchanged. Boyer *et al.* [68] characterized flame-sprayed Al-12Si coatings deposited onto polyurethane substrates. It was found that Al-12Si coatings with satisfactory bonding and electrical conductivity can be deposited onto polyurethane elastomer up to a threshold coating thickness. Beyond the threshold coating thickness, spalling (peeling) of the metal coating from the substrate occurred. Therefore, flame-sprayed coatings can be used to modify the electrical properties of the polymer substrate, provided that the deposition process does not compromise the structural integrity of as-sprayed structures.

Other studies have focused on the mechanical behaviour of the flame-sprayed metal coatings deposited onto polymer-based substrates. Huonnic *et al.* [19] studied the effect of flame-sprayed Al coatings deposited onto grit-blasted basalt and glass fibre composite tubes with a $[\pm 60°_3]_T$ fibre architecture. Significant damage to the FRPC structure was reported as a result of the flame spray metal deposition process. Subsequent studies [41, 42] utilized a garnet sand interlayer between the FRPC substrate and the flame-sprayed metal particles to protect the temperature sensitive substrate from the flame and particle impingement forces.

2.2.4 Electric arc wire spraying

Electric arc wire spraying is a thermal spray process whereby the heat generated in an electric arc discharge melts feedstock wires to form droplets, which are accelerated in a gas stream through a nozzle, for deposition onto the substrate [31, 69]. Two feedstock wires with opposing polarity converge at the nozzle outlet at a constant speed to generate the electric arc discharge. The electric arc wire spray process can generate gas temperatures in excess of 5000°C [69], whereas particle impact velocities are usually below 300 m/s [31]. Feedstock wires can be made of metals or metal-cored wires [31]. The process parameters of the electric arc wire spray process are arc gun geometry, electrical current input, arc gun stand-off distance from the substrate, carrier gas pressure, and wire material and feed rate [69, 70].

The electric arc wire spray process has been utilized to deposit Zn and Al particles onto polymer-based substrates. Liu *et al.* conducted two studies [71, 72] on the arc wire spray deposition of Zn and Al bond coatings (bond-coats) on to PMC substrates. In these studies, it was found that the metal bond-coat allowed the deposition of a harder and more thermally resistant top coating. Limited research is available on electrical arc metallization of polymer-based substrates, and recent studies have focused on the fabrication and characterization of bond-coats using low melting temperature materials such as Al and Zn. On the other hand, it should be noted that no studies to date have been reported on powder arc spray deposition of metal coatings onto polymer-based substrates.

2.2.5 Plasma spraying

Plasma spraying is a thermal spray process whereby an ionized gas jet melts and propels the feedstock powder for deposition onto the substrate. The plasma jet consists of a carrier gas that is expanded through a nozzle to create a sub- or supersonic flow [32, 73] while being heated to the ionized gas state by DC arc or RF discharges [32]. Argon, nitrogen, helium, and hydrogen may be used to produce the plasma jet, which reaches a temperature up to 14,000°C [55, 58]. Particle impact velocities associated with the plasma spray process are usually between 160 and 2000 m/s [26, 31]. The process parameters of the plasma spray process include torch geometry, electrical current input, torch stand-off distance from the substrate, plasma gas flow rate, and feedstock material [31]. Plasma spraying is a unique process compared to the other thermal spray processes due to the higher gas temperatures achieved by the plasma jet, which allow the deposition of metals with high melting temperatures.

Plasma spray metallization of polymers has been performed using air plasma spraying (APS). The APS process has been used to deposit Al, Zn, and Cu coatings onto PMCs [25, 45, 72, 74, 75]. Plasma-sprayed Al and Zn bond-coats deposited onto PMCs exhibited similar or higher shear adhesion strength compared to that of similar coatings deposited by electric arc wire spraying [72]. On the other hand, it has been noted that the high thermal load exerted by the plasma spray process on the polymer-based substrates can degrade the substrates [37, 72]. Therefore, careful execution of plasma spray metallization of PMCs should be considered to avoid structural degradation of the substrate.

Limited studies have been conducted on the plasma spray deposition of electrically conductive metals onto polymer-based substrates. Beydon *et al.* [75] and Ganesan *et al.* [74] reported the APS deposition of Cu layers onto PMCs using chemical and mechanical surface preparation of the substrate. Alternatively, Huang *et al.* [45] and Guanhong *et al.* [25] studied the deposition of Al bond-coat onto PMCs. In these studies, the research focus was on the fabrication and mechanical characterization of the metal deposits, as opposed to the investigation of the electrical properties of as-sprayed substrates. In industry, deposition of coatings on to polymer-based air foils for application as de-icing elements has been undertaken [18]. However, in an effort to protect intellectual property, the authors of the study did not disclose the spray parameters that were used to fabricate the coatings.

2.3 Surface preparation of polymer-based substrates

Preparation of the substrate for thermal spraying is essential to promote the adhesion of the impacting particles. The surface preparation process increases the roughness of the substrate surface and promotes the formation of a mechanical bond between the impacting particles and the substrate [76]. Grit blasting is the most common method for roughening the substrate prior to thermal spray deposition. During the grit blasting process, the roughness of the surface increases as a result of the erosion and material removal caused by the impact of high velocity hard grit medium. The application of grit blasting as a pre-treatment technique for thermal spraying is not limited to metal substrates and has been employed to roughen polymer-based substrates. Liu *et al.* [71] grit-blasted PMC substrates prior to plasma spray deposition, in order to promote the adhesion and fabrication of Zn coatings. Huonnic *et al.* [19] used grit-blasted glass and basalt FRPC tubes to promote the formation of Al coatings. Guanhong *et al.* [25] grit-blasted PMC substrates to promote the deposition of Al bond-coats using APS. Although grit blasting allowed the successful deposition and adhesion of metal coatings in previous studies, this process may not be a suitable method for brittle polymer substrates susceptible to cracking and localized fracture under the impact of high velocity grit media.

Damage induced in the substrate by grit blasting can adversely affect the mechanical properties of polymer-based structures. The results of the study by Huonnic *et al.* [19] suggested that grit blasting of FRPC tubes can decrease the burst pressure of the composite pipes by compromising the integrity of the reinforcing fibres of the composite. The degree of damage is dependent upon the velocity of the blasting media, which is a function of the control parameters of the grit blasting unit and physical properties of the blast media. Liu *et al.* [71] showed that the level of damage in a polymer substrate is likely to increase at higher pressures of the carrier air of the blasting medium due to the higher velocity of the impacting particles. On the other hand, difficulties associated with the grit blasting of polymer-based substrates are not limited to the risk of structural damage. Soft and flexible elastomers, such as polyurethane that exhibit high elongation at yield may cause the grit medium to rebound from the surface as it deforms elastically under the load of the impinging medium. Consequently, grit blasting of polymer-based substrates may not be suitable for surface pre-treatment prior to the thermal spray process and alternative methods may be warranted.

The addition of a granular material on the surface of the polymer substrate is an alternative method that has been used to increase the roughness of the substrate surface, in lieu of grit-blasting. Gonzalez *et al.* [41] roughened the surface of FRPC tubes by the addition a layer of garnet sand prior to the flame spray deposition of Al-12Si coatings. In contrast to results reported by Hounnic *et al.* [19], where the grit blasting process was employed, this technique did not alter the strength of the FRPC tubes and the internal pressure required to cause fracture and damage of the coated FRPC specimens remained unchanged from that of the uncoated FRPC specimens. Figure 2.3 shows a cross-section image of a Ni-20Cr coating and the sand layer added onto the FRPC substrate [77, 78]. The addition of a ceramic granular material, with its low thermal conductivity, also provides a barrier to heat transfer from the high-temperature flame and particles, protecting the polymer substrate from high-temperature degradation during the thermal spray process [41]. Also, Robitaille *et al.* [17] suggested that the granular layer can be added to the substrate surface during the curing process of the polymer substrate. In this study, a layer of Cu particles was added onto the FRPC substrate during the curing process to enable the deposition of Zn coatings. After the addition of this layer, the Zn coating was successfully fabricated onto the FRPC substrate without inducing any damage to the fibres. The idea of incorporating granular material on the surface of the polymer substrates during the curing process has also been employed for deposition of conductive coatings onto elastomers such as polyurethane. Boyer *et al.* [68] roughened the polyurethane surface by the addition of Cu particles during the curing process. It was found that flame-sprayed Al-12Si particles interlocked with the Cu particles to form a continuous electrically conductive coating. In another study conducted by Ashrafizadeh *et al.* [50, 79], the use of the same powder as that of the spraying powder was suggested to roughen the polyurethane substrate to ensure consistency between the roughening agent and the deposited particles.

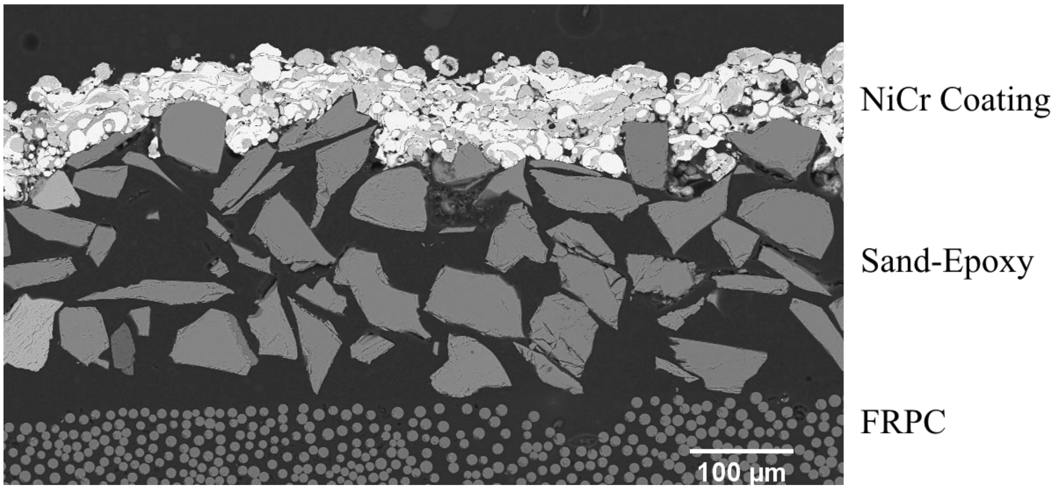

Figure 2.3: Backscattered scanning electron microscope (SEM) image of the cross section of a flame sprayed Ni-20Cr coating deposited onto a fibre-reinforced polymer composite (FRPC) [77, 78]

2.4 Thermal spray process parameters

The properties of thermal-sprayed coatings are a function of the spraying parameters. Thermal spray parameters can be considered as the process inputs that affect the particle velocity, particle temperature, and substrate temperature. The substrate temperature is of particular importance when depositing on substrates with a low heat capacity, such as polymer-based materials. In this case, the spraying parameters not only affect the morphology of the final deposited coating, they also affect the level of damage that the substrate might experience during the thermal spraying process.

Thermal spray processes allow for different ranges of deposition parameters (see, for example Fig. 2.2). The appropriate selection of the thermal spray process parameters should be considered in the context of thermal spray metallization of polymer-based materials. Liu *et al.* [72] showed that the arc spraying process is not suitable for metal coating deposition onto polymer substrates given that the tip of the feeding wire must be heated beyond its melting point to form droplets for deposition. Therefore, the control on the temperature of the arc-sprayed particles is limited compared to that of other thermal spraying processes such as flame spraying, in which the temperature of the spray plume can be controlled independently to avoid over-heating the impinging metal particles.

Table 2.1 summarizes the process parameters of thermal spray metallization processes for polymer-based structures. Values of these parameters should be selected based on the physical properties of the sprayed particles, the required temperature and velocity for particle deposition, and the substrate heat capacity. Consequently, spraying parameters such as the electric current input in plasma and arc spraying, and fuel and oxygen feeding rates in flame spraying should be apt to ensure that the produced thermal load will not compromise the integrity of the polymer substrates. Guanhong *et al.* [25] studied the effect of the plasma spray current on the quality of the coatings deposited onto polymer substrates. It was shown that the use of high current in plasma spraying for deposition of Al bond-coat caused cracking of the coating due to the introduction of excessive heat into the substrate. These cracks, coupled with localized delamination of the coating, decreased the adhesion strength of the final alumina top coating. Other spraying parameters such as air cooling and modifying the stand-off distance between the thermal spray heat source and the substrate can be employed for further process control. It has been found that the stand-off distance influences the metal coating deposition onto polymer-based substrates [20, 54]. Shorter stand-off distances led to shorter in-flight time of the metal particles and, therefore, they had higher impact velocity and temperature and reduced oxide content. On the other hand, shorter stand-off distances produce a higher heat flux into the substrate, increasing the temperature within that substrate [80]. This increases the risk of imposing excessive thermal load onto heat sensitive substrates such as polymer-based materials. As a result, setting the stand-off distance to very low values is not recommended for thermal spray deposition onto polymer-based materials, unless temperature control methods such as air cooling are used.

Table 2.1: Process parameters of thermal spray processes

Thermal spray process	Spray parameters
Cold spraying	• Feedstock powder • Nozzle geometry • Powder feed rate • Carrier gas pressure • Gas temperature • Stand-off distance
Flame spraying	• Feedstock powder • Nozzle geometry • Powder feed rate • Carrier gas pressure • Fuel gas flow rate • Oxygen flow rate • Compressed air pressure • Stand-off distance
Electric arc wire spraying	• Arc gun geometry • Wire material • Wire feed rate • Electrical current • Compressed air pressure • Stand-off distance
Plasma spraying	• Nozzle geometry • Feedstock powder • Powder feed rate • Electrical current • Plasma gas flow rate • Compressed air pressure • Stand-off distance

The injection of compressed air during the thermal spraying process is an effective method to cool the substrate and limit thermal damage induced by the thermal spray deposition process. As shown by Floristan *et al.* [81], air cooling was utilized to reduce the thermal load on the substrate and prevent the coating from cracking during plasma spraying of TiO_2-NiCrAlY onto glass substrates. The addition of compressed air can protect the substrate from residual-stress induced cracking by reducing the thermal load and temperature within the substrate. Also, the compressed air can increase splat deformation and decrease the porosity of the coating by increasing the impact velocity of the deposited droplets [81]. Ashrafizadeh *et al.* [50] studied the effect of the addition of compressed air to the flame spray nozzle for deposition of Al-12Si coatings on polyurethane substrates. It was shown that the addition of compressed air decreased the coating porosity and resulted in a reduction in the electrical resistance of the deposited coatings. The authors also showed that temperature control within the substrate was possible by reducing the stand-off distance while increasing the pressure and flow rate of the compressed air. As a result of using shorter stand-off distances, denser coatings with higher electrical conductivity were fabricated. In another study, Voyer *et al.* [20, 54] utilized air cooling of the substrate during deposition of flame-sprayed Al coatings onto polymer-based substrates. It was shown that by introducing cool air and optimizing the spraying parameters, the stand-off distance could be reduced without imposing any evident thermal damage to the polymer-based substrate. This technique allowed the fabrication of metal coatings with improved thermal conductivity at shorter stand-off distances.

Similar to other thermal spray metallization processes, cold spray parameters play an important role on the final characteristics of the deposited coating and possible mitigation of damage of the polymer-based substrate. Ganesan *et al.* [21] explored the feasibility of the cold spray process for the deposition of Cu coatings onto PVC substrates. It was shown that the gas temperature affects the coating deposition efficiency, possibly due to the thermal softening of the PVC substrate. In a subsequent study, Ganesan *et al.* [82] evaluated the effect of substrate type on the deposition efficiency of Cu particles. It was found that the brittle epoxy substrate exhibited a lower coating deposition efficiency compared to that of the PVC. Fracture of the epoxy substrate was observed during cold spray deposition, whereas the soft PVC substrate allowed the penetration of impacting particles, which resulted in higher deposition efficiency [82]. The thermal softening of the substrate caused by the impact of the high velocity particles during cold spray deposition of Al and Cu powders has also been reported by Zhou *et al.* [44]. The softening of the substrate was found to be responsible for the penetration of Al particles into the substrate [44]. Thus, depending on the mechanical properties of the substrate and the cold spray parameters, the particles with high velocity either rebound from or penetrate into the substrate [56]. Gardon *et al.* [48] utilized cold spraying to deposit titanium coatings onto bio-compatible PEEK substrates. Due to the softening of the substrate, the titanium particles penetrated (anchored) into the substrate in the absence of coating build-up. A balance between the carrier gas temperature and the thermal softening of the substrate was experimentally found to allow the deposition of titanium coatings onto polymer-based substrates. Another study conducted by Lupoi *et al.* [59] showed that Cu and Al powder particles are not suitable for cold spray metallization of polymer-based substrates using nitrogen as the cold spray gas. The high density of Cu particles led to high impact energy and erosion of the polymer substrate. Fabrication of Al coatings was unattainable since the required critical velocity for cold spray deposition of Al particles was not achieved for the given substrate and process parameters. On the other hand, tin (Sn), with lower specific weight and melting temperature was successfully deposited onto a variety of polymer-based substrates [59]. Therefore, the carrier gas temperature has a significant effect on the deposition of cold-sprayed metal coatings onto polymer-based substrates. If the gas temperature is not sufficiently high so as to soften the impacting powder, the high velocity, rigid particles may either penetrate or erode the substrate upon impact. However, introducing excessive heat during the cold spray deposition process can soften the substrate and limit the particle impact energy that remains available for particle deformation, adiabatic shear instability heating, and ultimate adhesion. Thus, knowledge of the particle velocity and substrate temperature distribution during the cold spray deposition process can facilitate the experimental approach to find optimum spray parameters for the deposition of metal coatings onto polymer-based substrates.

2.5 Potential applications

2.5.1 Electrical conductive structures

The fabrication of electrically conductive thermal-sprayed metal coatings onto polymers has gained attention as a fabrication technique for electrical sensors [53, 68, 83, 84]. However, the development of suitable thermal-sprayed electrically conductive coatings for engineering applications is currently an area of research [85]. Several fundamental studies [19, 68, 86-88] have shown that the porous structure of metal thermal-sprayed coatings result in electrical properties that differ from that of the bulk metal. Even though Ohmic resistive behaviour can be observed in thermal-sprayed metal coatings, such as Ni-Al [89] and Al-12Si [83], the porosity and morphology of the coating strongly affect the ability of thermal-sprayed metal coatings to conduct electrical charges. For instance, Sampath *et al.* [86] reported that dense cold-sprayed Cu coatings can exhibit a 25% increase in electrical resistivity with respect to that of the bulk Cu, while the resistivity of porous plasma-sprayed Cu coatings can increase by 300 - 400%. Therefore, the development of thermal-sprayed metal coatings that are tailored to have electrical performance that approach those of the bulk metal requires precise control of the process parameters and knowledge of the cross-property relationships, such as porosity and electrical resistivity.

Limited studies exist on the electrical characterization of thermally sprayed metal coatings deposited onto polymer-based structures for functional applications. Voyer *et al*. [20, 54] studied the deposition of electrically conductive Al coatings onto polyester fabrics deposited via the flame spraying process. Optimal flame spray deposition resulted in coatings that were 75 - 100 μm thick with a surface conductivity (reciprocal of sheet resistance) of up to 500 Siemens. It was found that an electrically conductive Al coating can be fabricated without compromising the flexibility of the polyester fabric. Huonnic *et al.* [19] deposited flame-sprayed Al coatings onto cured glass and basalt FRPC tubes and measured the electrical resistance and resistivity of the metal layer to characterize the quality of the deposits. A minimum of two flame spray torch passes was required to produce a uniform and electrically continuous metal layer on the polymer-based tubes. No evidence of phase changes or oxidation was observed in the flame-sprayed coatings. However, the values of electrical resistivity of the porous Al coating were measured to be 6×10^{-7} Ω-m and 8×10^{-7} Ω-m, which are one order of magnitude greater than the resistivity of annealed Al alloys (3×10^{-8} Ω-m). In another study, Gonzalez *et al.* [83] studied the electrical behaviour of flame-sprayed Al-12Si coatings for damage detection in cross-ply FRPC. The change in the electrical resistance of the Al-12Si coating was measured during the application of a linear tensile load to the coated FRPC specimens. It was found that the change in resistance across the Al-12Si coating due to early matrix damage in the cross-ply FRPC was limited, but increased significantly as a result of fiber-dominated damage and delamination in the substrate.

2.5.2 Thermal systems

Typical thermal properties of the polymer-based materials do not allow for efficient heat conduction through the material. Thermal-sprayed metal coatings can contribute to the enhancement of the conduction of heat in polymer-based material structures. For instance, Therrien *et al.* [42] utilized flame-sprayed Al-12Si coatings on glass FRPC substrates to study the heat conduction efficiency along the surface area of as-sprayed polymer-based plates. Al-12Si-coated samples were heated up with a resistance heating wire while thermocouples were used to measure the temperature distribution on the coated and uncoated sides of the polymer. This study found that the high thermal conductivity of the Al-12Si coating allows a more efficient conduction of heat to the surface of FRPC plates.

Additionally, methods that protect polymers from the adverse effects of high temperature are also required in the aerospace industry. Huang *et al.* [45] fabricated a multilayer Al-YSZ thermal barrier coating onto quartz FRPC using APS. An Al bond layer and YSZ top layer were successfully deposited onto the polymer composite and the thermal shock resistance of the coating was evaluated. It was found that thermal spray deposition of an Al bond-coat with an YSZ top layer can serve as a thermal barrier to protect the polymer-based structure.

Prevention of ice accretion on the surface of polymer-based structures is another potential application of the metal coatings that are thermally sprayed onto polymer substrates. Ice accretion is the formation and accumulation of ice due to exposure to a super-cooled fluid. Rooks [18] proposed the use of plasma spraying in the fabrication of resistive heater elements for ice protection of the leading edge portion of the main rotor blade of a military helicopter. Lopera-Valle *et al.* [77, 78] investigated the possible application of flame-sprayed nickel-chromium-aluminium-yttrium (NiCrAlY) and nickel-chromium (NiCr) coatings deposited onto FRPC structures for de-icing applications. Electrical current was applied to coated samples to increase the surface temperature by resistive (Joule) heating. The surface temperature profiles of the coatings were measured under free and forced convection conditions at different ambient temperatures, ranging from -25°C to 23°C. It was found that at ambient air temperatures below 0°C, the surface temperature of the coating, and in some cases, that of the FRPC remained above 0°C for both the forced and free convection conditions. In addition, there was a nearly homogeneous temperature distribution over the coating surface. This suggested that flame-sprayed coatings may be used as heating elements to mitigate ice accretion on polymer-based structures, without the presence of areas of localized high temperatures [77, 78]. An existing implementation is the PMC wing de-icing system integrated into the Boeing 787 Dreamliner [27]. However, limited studies are available on thermal spray metallization of PMCs for aerospace applications [90].

2.6 Conclusions

Polymer-based materials can exhibit excellent mechanical and physical properties, such as enhanced resistance to corrosion, resistance to wear, and high strength-to-weight ratio. However, the low thermal and electrical conductivities of polymer-based materials limit their use in electrical charge conduction applications and elevated temperature environments. Metallization of polymer-based materials by the deposition of metals is a possible means to augment their effective thermal and electrical conductivities. Also, the deposited metal coatings can provide new functionality for the new metal-polymer system such as resistive (Joule) heating applications.

One of the main challenges with thermal spraying on polymer materials is the inability to control the substrate temperature during the deposition process since most polymers have low thermal conductivity and heat capacity and may degrade or experience significant changes in properties at high temperatures. The review of different thermal spray deposition processes demonstrated that cold spraying, flame spraying, electric arc wire spraying, and plasma spraying have been employed in previous studies for the metallization of polymer materials. Although these processes can expose the polymer substrates to high heat loads, which depends on the spraying parameters and feedstock material, successful metal deposition onto polymer materials can be achieved. The use of compressed air cooling and deposition of low melting temperature metals as bond-coat prior to deposition of the final top coating were introduced as two methods to control the thermal load on the polymer-based substrate from the spray torch.

Based on previous studies on pre-treatments of the polymer surface, grit blasting of polymer materials may not be the optimal pre-treatment option for thermal spray metallization due to the risk of inducing structural damage in the polymers. Roughening of the substrate by the inclusion of powder materials on the surface of the polymer substrates, either during the curing process or by an adhesive agent, was recommended. The protection provided to the polymer-based substrate by the low thermal conductivity roughening agent from the heat load during thermal spray metallization was briefly discussed. However, fundamental study and analysis in this area is needed and future research is required.

Improvement of thermal and electrical conductivities of the polymers has been the focus for deposition of the metal coating onto polymer-based substrates in most studies. On the other hand, it has been shown that the combination of the metal coating and the polymer can produce a material system that is capable of being employed in novel applications. The applications discussed in published studies included the use of the deposited coating as a heating element for de-icing purposes, antifouling, and electrical conduction. Overall, future work is needed in these areas to establish and test the possible novel applications of metal deposits onto polymer-based substrates.

Chapter 3 Effect of Flame-sprayed Al-12Si Coatings on the Failure Behaviour of Pressurized Fibre-reinforced Composite Tubes*[28]

3.1 Introduction

The fabrication of metal-polymer using thermal spraying has received increasing attention in recent years. Thermal spraying encompasses a group of coating processes in which a heat source is used to melt and accelerate powdered particles, prior to their deposition onto components. Limited literature exists on functional metallic coatings deposited on fibre-reinforced polymer composite (FRPC) substrates [17, 19], which requires satisfactory cohesion and adhesion of thermal sprayed particles.

Surface preparation affects the adhesion of the thermal-sprayed particles to the substrate and conditions the quality of thermal spray deposits. Theoretical and

---

* A version of this chapter was published in *Polymer Testing* 32 (8) (2013) 1522-1528.

experimental studies have shown that large contact surface areas and roughened surface topography promotes mechanical interlocking between the coating and the substrate in metal-polymer structures [91, 92]. However, surface roughening by grit blasting can damage the polymer substrate [19, 71], thus compromising the structural integrity of fibre-reinforced polymer composites.

Mechanical degradation of the metal-polymer structure can also occur due to the thermal spraying processes involving high temperatures. Thermal spraying may generate residual stresses in the material in three ways: (i) tensile quench stress from rapid cooling during solidification of the powdered particles; (ii) compressive peening stress due to impact of the high-velocity spray particles; and (iii) thermal mismatch due to the relative difference in heat transfer and thermal expansion properties between the coating and the substrate [23]. While high temperature thermal spray processes like plasma spraying have been investigated for deposition onto polymers [24, 25], limited studies are available that focus on the deposition of metals onto fibre-reinforced composites using low temperature and low cost thermal spraying processes, such as flame spraying. Flame spraying, a form of thermal spraying, is an additive manufacturing process in which a relatively low temperature flame is utilized to perform layered coating deposition of molten and semi-molten particles onto the substrate.

Flame spray deposition of metallic coatings can reduce the mechanical strength of FRPC structures. A preliminary study by Huonnic, *et al.* [19]

considered the mechanical effect of flame-sprayed aluminium particles deposited onto grit-blasted basalt and glass fibre composite pipes. The pipes were created by filament winding, a cost-effective fabrication process by which multiple fibre strands are consolidated around a mandrel with controlled fibre orientation and tension to create high performance pipes and pressure vessels in a relatively automatic manner [93, 94]. Damage to the fibre-reinforced polymer matrix composite structure occurred as a result of depositing the metal coating [19]. It was found that grit blast roughening supported the adhesion of the flame-sprayed aluminium coatings onto glass and basalt composite pipes at the expense of mechanical strength of the pipes.

From the perspective of practical applications, it is important to mitigate mechanical degradation effects due to thermal spraying on polymers while promoting satisfactory adhesion of the thermal-sprayed coatings onto the substrate. Many studies on composite materials have focused on the damage mechanisms that occur when fibre-reinforced composite structures are subjected to mechanical loading [95-99]. Moreover, it has been found that the leakage behaviour of pressurized composite structures is associated with complex damage patterns of the polymer matrix [98], in which leakage points are not necessarily correlated with surface strain patterns [100]. The leakage failure of a filament-wound fibre composite subjected to internal pressurization is the result of progressive through-thickness microcrack paths, with the most likely damage initiation sites being the fibre/matrix interface and the inter- and intra-ply voids

[101]. However, knowledge about leakage behaviour of filament-wound polymer matrix composites coated by thermal spraying is limited.

In this chapter, garnet sand was incorporated as a surface roughening agent onto filament-wound tubes to enhance the mechanical properties of the outer thermosetting resin layer, as suggested by Melo, *et al*. [102], and to prevent possible thermal degradation during the flame spray deposition of aluminium-12silicon (Al-12Si) coatings. The objective of this work was to evaluate the effect of flame spraying Al-12Si on the leakage behaviour of garnet-sand roughened fibre-reinforced composite tubes at room temperature.

3.2 Experimental method

Preliminary data from four coated and four uncoated specimens were utilized to perform an initial statistical sample size computation using a power level (1 - β) of 80%, a critical probability (significance level), α of 0.05, and an allocation ratio, A of 1. The group sample size, n, was estimated using the following inequality, in terms of *t*-statistics [103]:

$$n \geq \frac{\left(t_{\nu,1-\alpha/2} + t_{\nu,1-\beta}\right)^2 \cdot \left(s_1^2 + s_2^2\right)}{\left|\bar{x}_1 - \bar{x}_2\right|^2}, \tag{1}$$

where s_1 and s_2, respectively, denote standard deviations of the initial coated and uncoated samples, $\bar{x}$ is the sample average, and the number of degrees of freedom, *v*, is given by the Welch–Satterthwaite equation for two unknown population variances [104]. It was found that a minimum of nine specimens each for the coated and uncoated sample groups were necessary for statistical analysis, assuming normally distributed leakage and burst pressures [103].

3.2.1 Filament winding

Nineteen fibre-reinforced epoxy composite tubes were fabricated using a four-axis filament winding system (WMS-4 axis, McClean-Anderson, Schofield, WI, USA) and a 38.1 mm (1.5 inch) diameter steel mandrel. Five E-glass fibre strands (Advantex type 30, Owens Corning, Toledo, OH, USA), each with a linear density of 1.1 g/m, were impregnated in a drum-type bath with the EPON 826-EPICURE 9551 epoxy system (Hexion Specialty Chemicals, Columbus, OH, USA), which consists of a liquid diglycidyl ether of bisphenol-A epoxy resin and a non-MDA (methylene dianiline) proprietary polyamine curing agent. A schematic of the filament winding process is shown in Fig. 3.1 [105]. Fibre strands were incorporated into helical bands to create a $[\pm 60°_2]_T$ winding architecture. The angle-ply lay-up of ±60° is common for pressurized composite piping, which usually incorporates winding angles between 55 and 70° [93]. The resin bath was kept at a constant temperature of 30°C, and each fibre strand was under a controlled tension of 15.56 N (3.5 lb). A layer of 80-grit (~165 μm) garnet sand was manually sprinkled on top of the resin-wet fibre material and consolidated during the curing process, which was performed at 80°C for 1 h and at 120°C for 2.5 h. Garnet sand serves as an inexpensive roughening agent to: (i)

Promote adhesion of the molten Al-12Si particles [28], (ii) Enhance the mechanical properties of the outer thermosetting resin layer [102], and (iii) Reduce thermal degradation of the polymer-based substrate during the flame spray deposition process. The internal diameter and nominal wall thickness of the composite tubes were determined to be 38.1 mm and 1.5 mm, respectively. The cured composite tubes were removed from the winding mandrels and cut into 190 mm long specimens. Random allocation of the specimens across the flame spray deposition group (strictly randomized experimental design) [106] was performed to reduce statistical confounding and equalize manufacturing factors during filament winding.

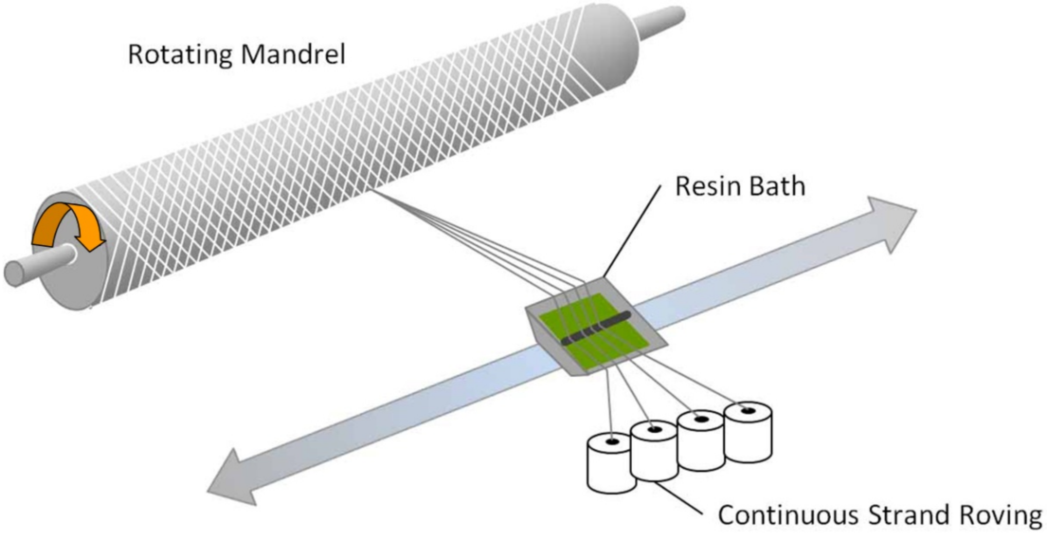

Figure 3.1: Schematic of the filament winding process for FRPC fabrication [Adapted from [105]]

3.2.2 Flame spraying

A spheroidal and gas-atomized Al-12Si powder consisting of aluminium alloyed with 12 wt.% silicon, and particle size of 45 μm to 90 μm (52C-NS, Sulzer Metco, Westbury, NY, USA) was deposited onto filament-wound specimens using an oxy-acetylene flame spray torch (6P-II, Sulzer Metco, Westbury, NY, USA). The torch was attached to a Motoman robot arm (HP20, Yaskawa Electric Corporation, Fukuoka, Japan) to deposit a thin metallic coating over the garnet-sand-roughened composite tubes. No grit blasting of the substrate was performed prior to powder deposition.

The Al-12Si powder was injected into the flame spray torch by a volumetric powder feed unit (5MPE, Sulzer Metco, Westbury, NY, USA) using argon as the carrier gas at a pressure of 515 kPa (60 psig) and 0.4 m^3/h (15 standard cubic feet per hour), which resulted in a powder flow meter reading of 90 on the powder feed unit. During flame spray deposition, a mixture of 8 NLPM (normal liters per minute) of acetylene and 25 NLPM of oxygen was utilized to generate a combustion flame from the flame spray torch. The torch travelled linearly and parallel to the specimen axis at a distance of 93 mm from the substrate (stand-off distance) and performed two passes at 31 mm/s, while the tube rotated at 600 revolutions per minute, as shown in Fig. 3.2. Ten tubular specimens were flame-sprayed with Al-12Si. Nine other tube specimens remained uncoated and were used as control samples in the internal pressurization tests.

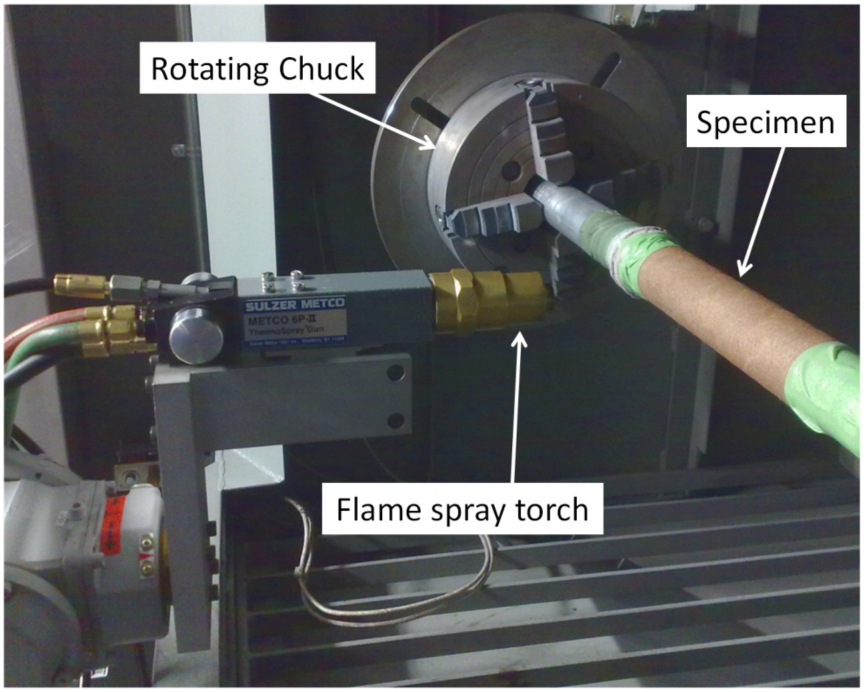

Figure 3.2: Experimental assembly for flame-sprayed Al-12Si coating deposition

3.2.3 Internal pressurization tests

The internal pressurization tests were executed by bonding each fibre-reinforced composite tube to two aluminium end connections using a high performance adhesive (DP-460, 3M, St. Paul, MN, USA). This created an effective 89 mm gauge section, as shown in Fig. 3.3. A schematic of the internal pressurization apparatus is shown in Fig. 3.4 [99]. An internal bladder was placed inside each tube. The bladder and the annulus formed by the bladder and the inner tube wall were filled with hydraulic fluid (Esso NUTO H-46, Imperial Oil Limited, Calgary, AB, Canada). The hydraulic oil inside the specimen was mixed with a UV dye and constituted the secondary fluid illustrated in Fig. 3.4, which allowed fluid loss observations.

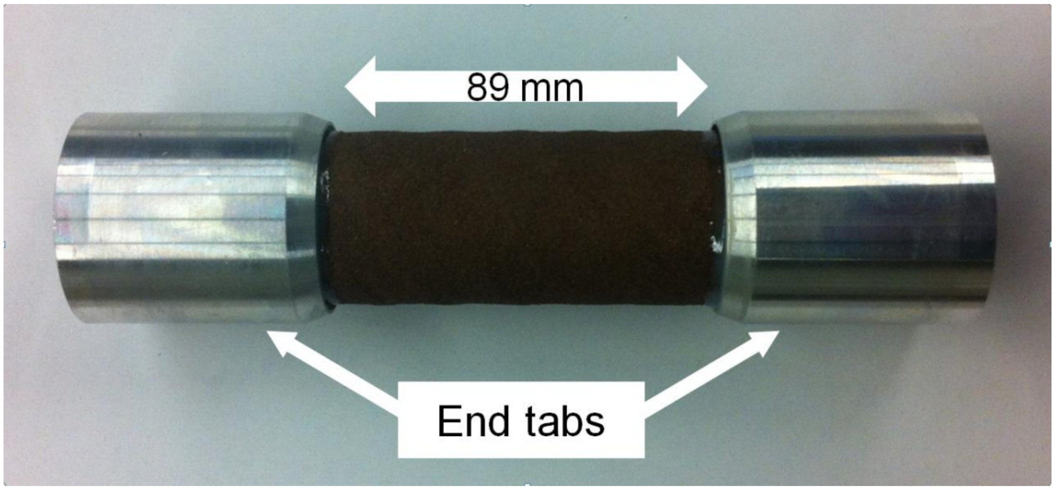

Figure 3.3: Internal pressurization test specimen

Mechanical testing was performed in a multi-axial loading system under stress control [99, 107]. A monotonic pressure vessel loading condition with a ratio of hoop-to-axial stress of [2H:1A] was utilized. System control and measurements were accomplished by employing a personal computer and an analog controller (MTS 458, MTS Systems Corporation, Eden Prairie, MN, USA) to record internal pressure, internal fluid volume loss, and applied axial load. Hoop (σ_H) and axial (σ_A) stresses were determined by using Eqs. (2) and (3) [97] to confirm that a hoop-to-axial stress ratio of [2H:1A] was applied during the internal pressurization tests:

$$\sigma_{\mathrm{H}} = \frac{d_{\mathrm{i}} \cdot P'_{\mathrm{i}}}{2 \cdot (d_0 - d_{\mathrm{i}})}, \quad (2)$$

$$\sigma_{\mathrm{A}} = \frac{4 \cdot F}{\pi \cdot (d_0^2 - d_{\mathrm{i}}^2)} + \frac{P'_{\mathrm{i}} \cdot d_{\mathrm{i}}^2}{(d_0^2 - d_{\mathrm{i}}^2)}, \quad (3)$$

where P'_{i} is the internal pressure, F is the applied axial force, d_0 is the outer diameter of the tube specimen, and d_{i} is the inner diameter of the tube specimen. The internal pressure was applied inside the bladder at a constant rate of 4.63 kPa/s. At leakage failure, hydraulic fluid penetrated through the tube wall causing the bladder to expand until the bladder touched the specimen inner wall, thus sealing the interior of the tube and allowing further pressurisation. The pressure vessel test continued until ultimate structural failure (burst) of the specimen occurred. Post-processing of the resulting fluid loss data was performed by subtracting the tangent line approximation of the volume-pressure function for values below the leakage pressure in order to account for the compressibility and expansion characteristics of the hydraulic system [98]. The corrected fluid loss through the tube was obtained by this post-processing procedure, which allowed characterization of the leakage events. A leakage failure threshold was set at a fluid loss of 2,000 mm^3 to define the leakage pressure at which the specimen was no longer deemed able to contain fluid [19, 97]. Burst failure was characterized by a sudden, abrupt decrease in internal pressure [108].

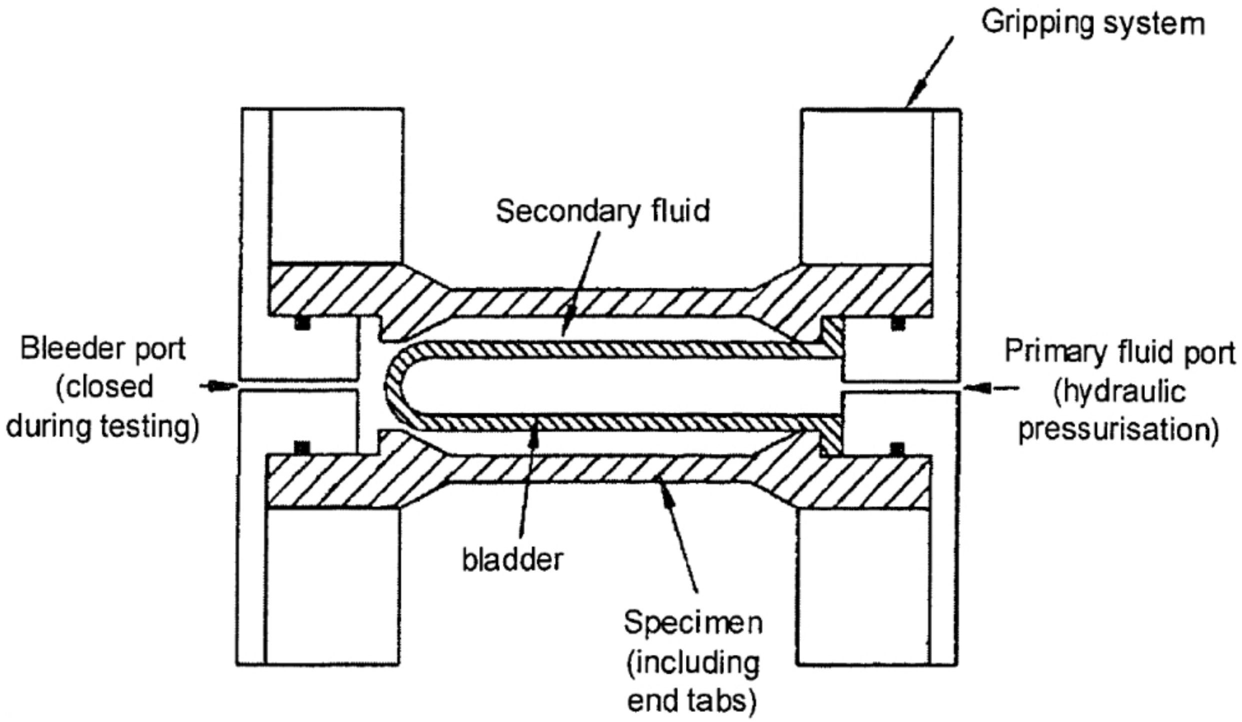

Figure 3.4: Cross-sectional schematic view of the apparatus used to perform internal pressurization tests, showing the test specimen and the bladder [Adapted from [99]]

3.3 Results and discussion

3.3.1 Scanning electron microscopy

One randomly selected flame-sprayed tubular specimen was cut perpendicularly to the cylinder axis to expose its cross section. A 10-mm wide section was mounted and polished to a 1-µm finish for microscopy. A Scanning Electron Microscope (SEM) (Zeiss EVO MA15 Scanning Electron Microscope, Carl Zeiss, Toronto, ON, Canada) was utilized to produce a backscattered SEM image of the mounted specimen cross section, as shown in Fig. 3.5. based on SEM images, the flame-spayed Al-12Si coating exhibited a thickness of approximately 200 µm (0.2 mm).

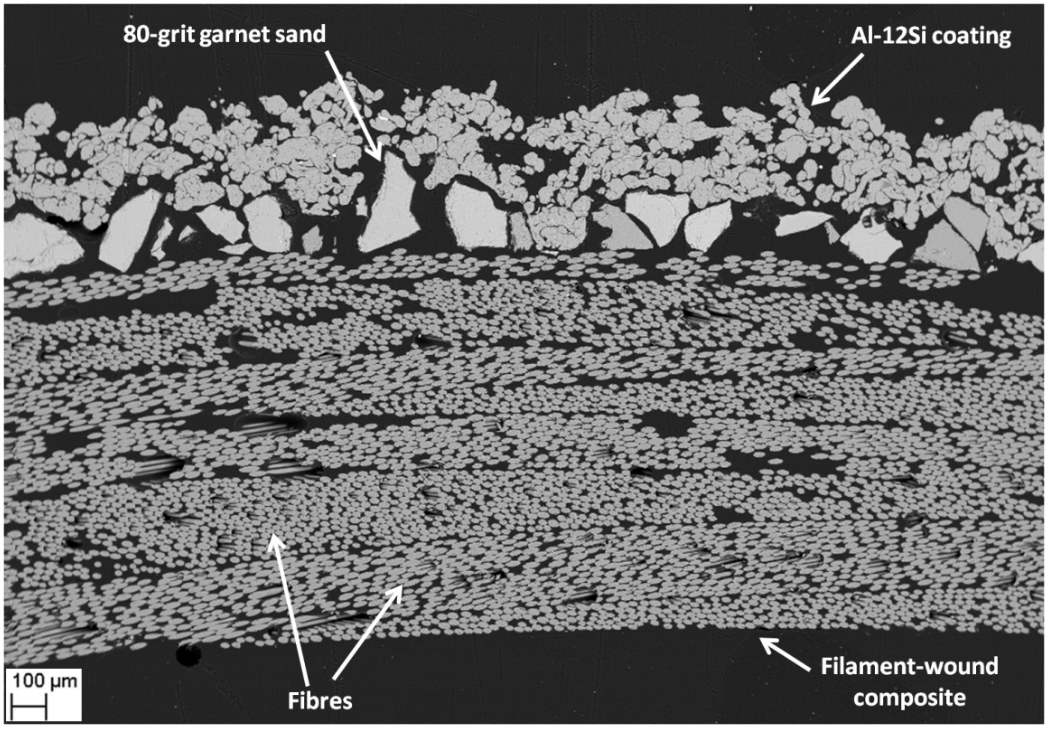

Figure 3.5: Backscattered SEM image of the cross section of a flame-sprayed Al-12Si coating on a fibre-reinforced composite

3.3.2 Leakage behaviour

The leakage behaviour was examined at room temperature in order to prevent any variations in the permeability characteristics of the FRPC tube due to temperature-induced viscosity variations of the hydraulic fluid [98]. The [2H:1A] stress ratio imposes tension and considerable in-plane shear stress on the polymer matrix of samples with a $[\pm 60°_2]_T$ fibre architecture, leading to an increasing density of transverse matrix cracks and, ultimately, specimen leakage [19, 109].

Figure 3.6 shows leakage curve data for flame-sprayed (designated as C1, C2, ... , C9) and uncoated (designated as U1, U2, ... , U9) specimens obtained during pressure vessel tests. The characteristic leakage behaviour of the uncoated and coated specimens followed an s-shaped leakage curve during the pressure vessel tests, which relates fluid loss and internal pressure. No leakage was observed until a pressure threshold that was between 7,000 and 10,000 kPa was exceeded. Therefore, below an internal pressure of 7,000 kPa, the corrected fluid loss from the tubes was zero, as shown in Fig. 3.6. Depending on the specimen, as the internal pressure was increased beyond 7,000 to 10,000 kPa, leakage failure was followed by considerable fluid loss and eventually final burst failure. The transition point between the high fluid loss rate and the low fluid loss rate regimes indicated the moment at which the internal bladder came in contact with the specimen inner walls (Fig. 3.4). Ultimate structural failure (burst) of the specimen occurred at the point of maximum internal pressure on the leakage curve (see Fig. 3.6).

The standard error of the mean is included with the sample size (*n*) used for all the averages values henceforth in this study [110]. The linear relationship between applied pressure and time was confirmed using the experimental data of all the FRPC tube specimens, with a maximum elapsed time at bursting of 5,386 s (approximately 90 minutes). The average leakage time in coated FRPC tubes was 1,901 ± 39 s ($n = 9$), which was higher than that shown by uncoated samples, at 1,883 ± 28 s ($n = 9$). Average burst times for coated and uncoated specimens were

4,819 ± 103 s ($n = 9$) and 4,755 ± 139 s ($n = 9$), respectively. The slight differences in leakage and burst times may indicate that additional barriers against microcrack propagation and fluid loss may have been provided by the flame-sprayed Al-12Si coating and the garnet sand layer.

The damage features observed in the uncoated and the flame-sprayed specimens were similar. Leakage damage was characterized by the appearance of small oil droplets on the surface of the composite tubes as a result of cracks in the polymer matrix, which is an agreement with the observations by Huonnic, *et al.* [19]. Previous research has indicated that transversal crack development and propagation in the ±60° filament-wound tubes is related to in-plane shear strains, and leakage failure is predominantly a result of the coalescence of internal matrix microcracks [109]. Ultraviolet (UV) imaging was used to illustrate a characteristic leakage pattern of UV-dyed hydraulic oil at the onset of specimen leakage. The surface leakage pattern depended on the evolving matrix damage and resulting fluid permeability of the tube wall, but usually started with helical microcracks along the fibre orientation, as shown in Fig. 3.7. Figure 3.8 shows that, as the internal pressure increased, extensive matrix cracking developed throughout the composite structure, followed by localized rupture of the fibres and ultimate structural failure.

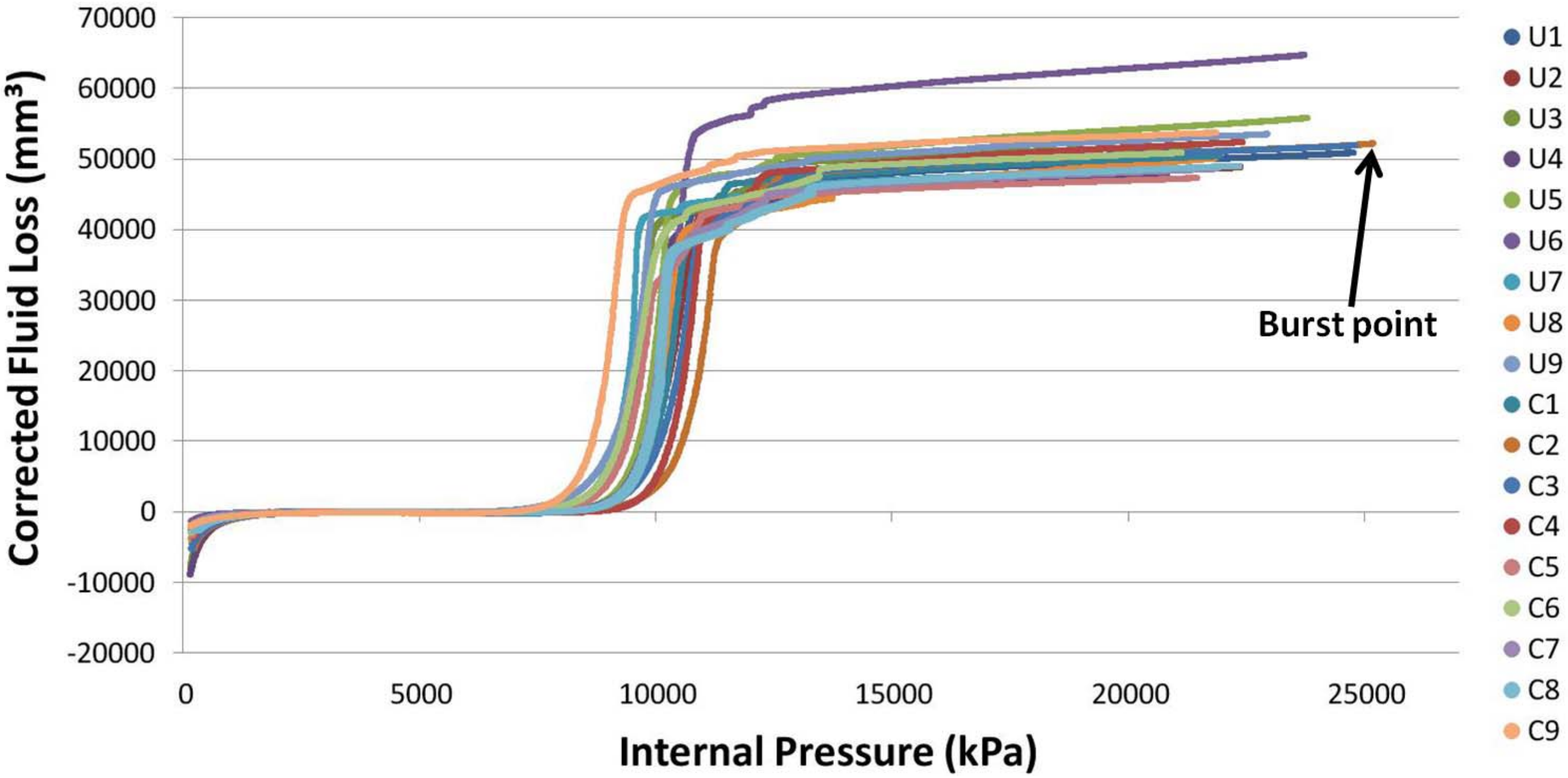

Figure 3.6: Leakage behaviour of coated (C) and uncoated (U) specimens under pressure vessel loading

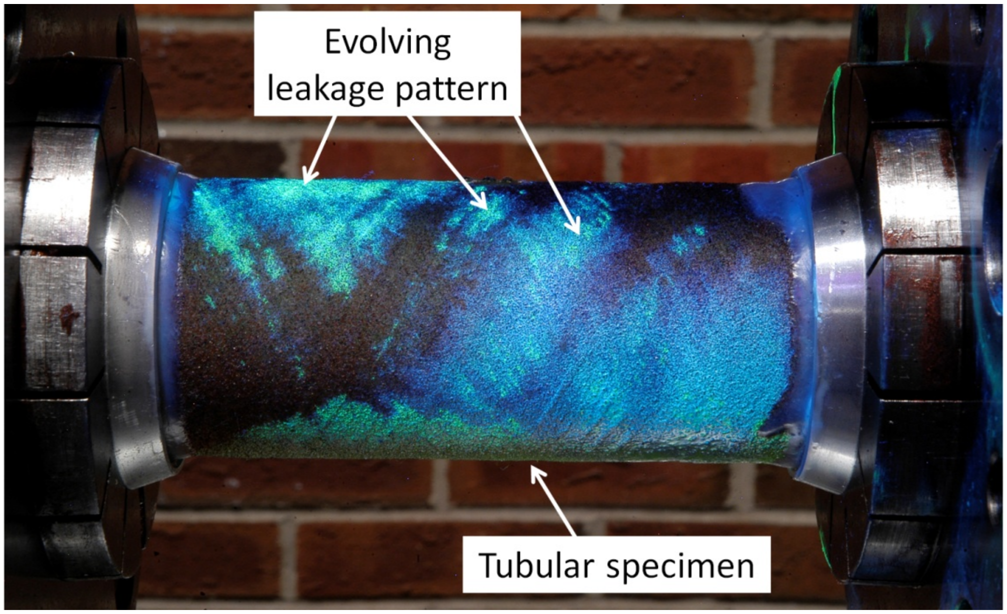

Figure 3.7: Ultraviolet (UV) image of the leakage pattern of UV-dyed hydraulic oil at the onset of fluid loss

Figure 3.8: Fibre-reinforced composite tube after structural failure (burst)

Figure 3.9 shows the leakage and burst pressures of each sample that was investigated in this study. The average leakage pressure of coated FRPC tube specimens was 9,000 ± 189 kPa ($n = 9$). The uncoated FRPC tube specimens exhibited an average leakage pressure of 8,895 ± 130 kPa ($n = 9$). Similarly, the average burst pressure of the coated specimens were 22,527 ± 482 kPa, whilst that of the uncoated specimens was 22,211 ± 647 kPa. The results of leakage and burst pressure values suggest that no appreciable reduction in the leakage and burst pressure values exist due to the flame spray deposition of Al-12Si coatings onto FRPC tubes covered with garnet sand. In contrast, mechanical degradation of the FRPC substrate was reported by Huonnic, *et al*. [19], who used grit blasting and flame spraying on antisymmetric $[\pm 60°_3]_T$ tubular specimens. In the study by Huonnic, *et al*., the coated FRPC tubes exhibited leakage pressures that were 16% lower than those of the uncoated FRPC tubes, while the burst pressures were 35% lower [19].

Leakage and burst strengths of $\pm\theta$ filament-wound tubes is influenced by the geometry of the specimen, including the wall thickness, as shown in Eqs. (2) and (3). However, the increase in wall thickness due to flame spray deposition of the Al-12Si coating may not directly translate into higher leakage and burst strength if accompanied by structural damage during surface preparation [19] or heat flux propagation from the thermal spray process into the fibre-reinforced polymer tubes [29]. Heat flux to the polymer matrix during flame spraying may be inhibited by providing an insulating layer and decreasing the deposition temperature. The garnet sand layer provided a low-cost insulation barrier to heat transfer to the polymer matrix during the flame spraying process. This is expected since the thermal conductivity of garnet sand is low and is of the order of 1 $Wm^{-1}K^{-1}$ [111]. In addition, Al-12Si is an eutectic system with a melting point (577°C) that is lower than that of pure aluminium (660°C), which may limit matrix decomposition and composite degradation in FRPC tubes by allowing lower working temperatures at greater stand-off distances to the flame spray torch during coating deposition (Fig. 3.2).

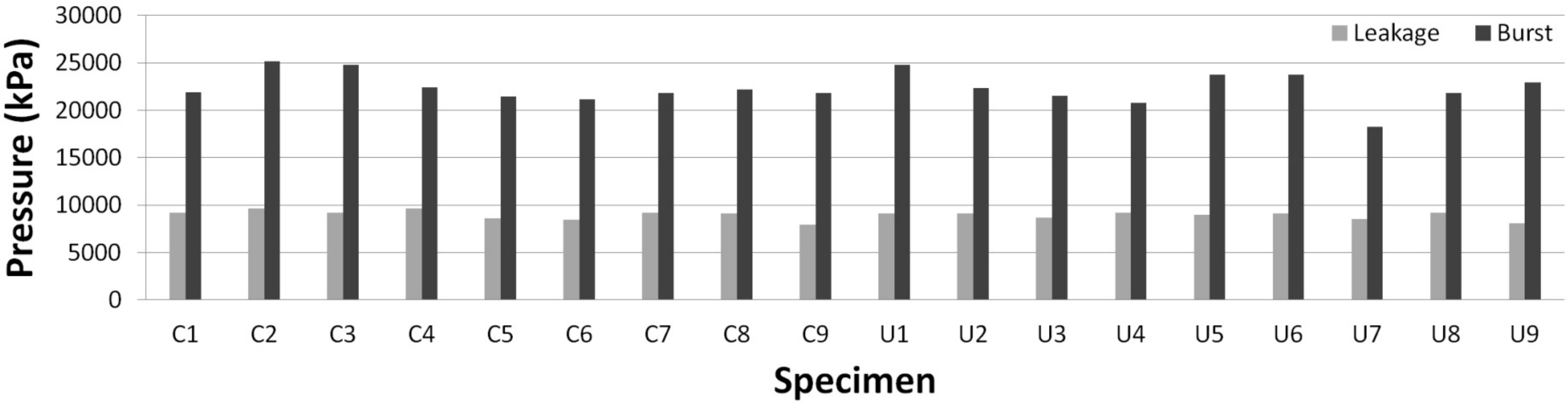

Figure 3.9: Internal pressure values for sprayed (C) and uncoated (U) specimens at the leakage threshold and burst point

3.3.3 *t*-tests with coated and uncoated FRPC tube specimens

t-tests were performed to evaluate the statistical difference in the mean leakage pressure values of the uncoated and coated samples. One-tailed *t*-tests were performed using nine Al-12Si coated and nine uncoated specimens in order to evaluate the effect of the deposition of Al-12Si coating on the leakage and burst pressures. Based on statistical sample information, *t*-tests evaluate the difference in the sample averages of two normal populations to infer the equality or relative inequality in the respective population means. Standard statistical assumptions for *t*-tests with unequal variances and a significance level of $\alpha = 0.05$ were used in the evaluation of the coated and the uncoated FRPC sample sets [112]. The significance level of $\alpha = 0.05$ is conventional in experimental studies based on statistical inference [113, 114]. The normality of the leakage and burst pressure data was confirmed using a residual normal probability (Q-Q) plot. As shown in Fig. 3.10, the normal probability plot of residuals exhibited an approximately linear trend with respect to the theoretical quantiles of the normal probability distribution, which was verified by obtaining a coefficient of determination $r^2 = 0.9073$ for simple linear regression, thus validating the assumptions of the *t*-tests [104, 115, 116].

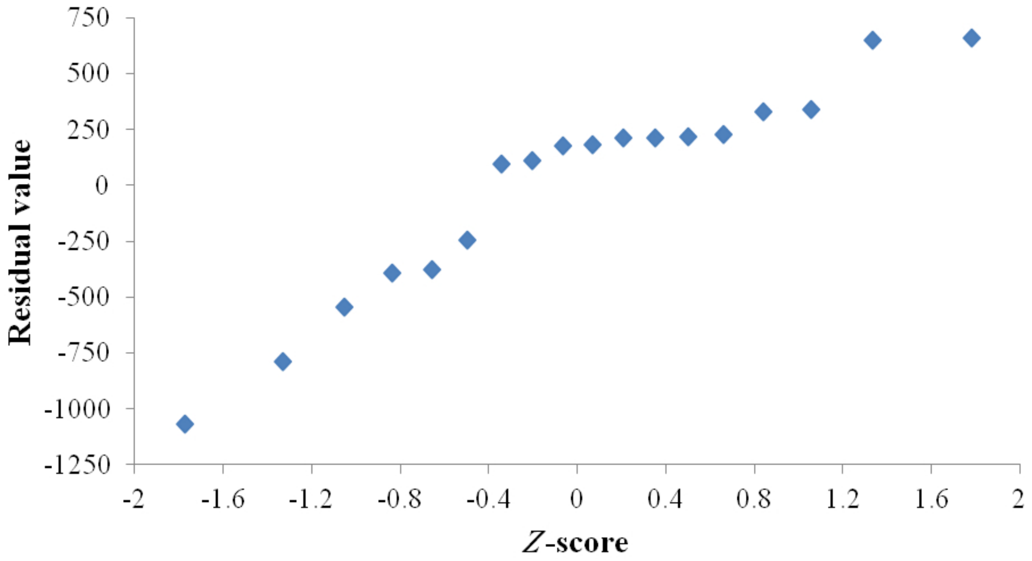

Figure 3.10: Normal probability plot showing the relationship between the mean leakage pressure residuals of coated and uncoated FRPC tubes and the theoretical quantiles of the normal probability distribution, *Z*-score

One-tail *t*-tests were conducted to determine the *p*-values, by assessing whether the average leakage and burst pressures of the Al-12Si flame-sprayed sample group were significantly greater than those of the uncoated group, at a critical probability (significance level) of $\alpha = 0.05$. The *p*-value is the probability of obtaining the observed pressure values, assuming that there was no effect due to the flame spray deposition of the Al-12Si coating and the mean pressure values for the Al-12Si coated and uncoated populations were equal. Since the critical probability value used in this study was $\alpha = 0.05$, it follows that a significant difference would be present only if a *p*-value equal to or less than 0.05 was obtained.

The one-tailed leakage pressure *t*-test yielded a *p*-value of 0.327, which was greater than $\alpha = 0.05$, indicating, statistically, that the deposition of Al-12Si coating does not affect the leakage pressure of tubular specimens. The *p*-value of the one-tailed burst pressure *t*-test was determined to be 0.350, a value that was also greater than $\alpha = 0.05$. Therefore, the statistical results of the *t*-tests suggest that mean leakage and burst pressures of Al-12Si flame-spray coated specimens were equal to those of the uncoated specimens.

Since statistical analysis showed that no reduction in the leakage or burst pressure values of Al-12Si flame-sprayed FRPC tube specimens occurred, it is expected that FRPC pipes and pressure vessels can be flame-sprayed with suitable metals with no mechanical degradation to the structure.

3.4 Conclusions

The effect of flame spray deposition of Al-12Si coatings on the leakage and burst pressures of FRPC tubes covered with garnet sand was investigated in this study. Suitable flame spray parameters were utilized to deposit an Al-12Si coating onto garnet sand roughened specimens. The application of garnet sand allowed for adhesion of Al-12Si coatings onto filament-wound tubes and provided insulation against heat transfer to protect the composite pipe fibres.

Pressurization tests showed that the average leakage pressure and average burst pressure values of flame-sprayed coated FRPC tube specimens were about 1% higher than those of uncoated FRPC tube specimens. *t*-tests were conducted using internal pressurization data in order to evaluate statistically the effect of Al-12Si deposition on leakage and burst pressure values. By using a significance level of $\alpha = 0.05$, one-tailed *t*-tests confirmed that there was no reduction in the pressure values due to Al-12Si deposition. Strong statistical evidence suggests that Al-12Si flame-sprayed FRPC tubes possess equal leakage and burst pressure values to those of unsprayed FRPC tubes. The combination of an additional garnet sand layer and a low-melting-temperature Al-12Si eutectic system limited the heat transfer to the polymer matrix of the fibre-reinforced composite during flame spraying, and hindered mechanical degradation of as-sprayed specimens.

Chapter 4 Application of the classical laminate model to flame spray coated fibre-reinforced polymer composites[*]

4.1 Introduction

The Classical Laminate Theory (CLT) can be considered as an extension of the Kirchhoff–Love plate theory of homogeneous plates to include in-plane loads in multi-laminar composite structures [117]. Even though the CLT constitutes a widely accepted macromechanical method to characterize the elastic behaviour of fibre-reinforced polymer composite (FRPC) structures [118-120], its application usually requires the definition of the mechanical properties of each lamina (layer) to obtain the stiffness of the resulting multi-laminar plate or laminate. Therefore, the deposition of coatings onto FRPC laminates may be considered from the perspective of structural stiffness and the CLT.

The deposition of thermal-sprayed metal coatings onto FRPC laminates has gained increased attention as a method to provide structural functionality [17,

---

[*] A version of this chapter is scheduled for submission to *Experimental Mechanics* in September 2015.

19]. Thermal spraying encompasses a group of coating deposition processes in which a heat source is used to melt and accelerate powdered particles, prior to their deposition onto the substrate. Since mechanical degradation of the metal-FRPC structure can occur due to the thermal spray process [19, 41], the use of a relatively low temperature and low cost thermal spray deposition process, such as flame spraying, is of interest. Flame spraying is a thermal spray process in which a relatively low temperature flame, formed from the combustion of a fuel in oxygen, is utilized to deposit a thin coating of molten particles onto a substrate. Moreover, the utilization of the relatively low temperature flame spray process in tandem with low melting point materials, such as aluminium-12silicon (Al-12Si), may limit mechanical degradation of FRPC structures [41].

The macroscopic mechanical behaviour of a flame-sprayed Al-12Si coating deposited onto FRPC laminates may be characterized as that of an isotropic lamina [121]. Moreover, the elastic modulus of the flame-sprayed Al-12Si coating influences its fracture behaviour under applied loads [122]. The elastic modulus of a dense, homogeneous, and isotropic material is independent from the microstructural features and is determined by the volume fraction of the phases present and their respective elastic moduli [123]. In contrast, the mechanical properties of flame-sprayed Al-12Si coating can significantly differ from those of the bulk material [26, 124-127] and may be difficult to predict using analytical and numerical models of the porous medium [128]. Even though the mechanical properties of flame-sprayed Al-12Si coating can be estimated experimentally via indentation tests [129-131], tensile tests may provide a direct measurement of the effective elastic properties of the coating, such as the Young's modulus and the Poisson ratio, when it is in the form of a lamina. Tensile testing of thermal-sprayed films [125, 132, 133] allows the direct estimation of the macroscopic mechanical properties of thermal-sprayed deposits and avoids the potential limitations of localized indentation methods for evaluation, which can be affected the substrate properties and require multiple measurements for the characterization of macroscopic material volumes [58, 134].

In this chapter, the characterization of flame spray coated uniaxial FRPC structures exhibiting a symmetric laminate architecture is considered. The objectives of this work were to: (1) assess of the mechanical properties of the flame-sprayed Al-12Si coating lamina and (2) evaluate the accuracy of the CLT model in predicting the stiffness of the coated FRPC laminate.

4.2 Stiffness of uniaxial FRPC laminates

The classical laminate theory [117, 119] of FRPC laminates provides a framework for development of load-strain constitutive relations in static equilibrium. The load-strain constitutive relations of a uniaxial FRPC laminate of dimensions b in width and l in length can be studied using a global coordinate system of x, y, and z mutually orthogonal axes aligned to the orthotropic directions under in-plane loads, as shown in Fig. 4.1. Each lamina may be construed of different materials and exhibit oriented and continuous fibres at an arbitrary in-plane angle θ with respect to the reference in-plane global axis (x or y). The reference global x-axis is henceforth used in this study, which corresponds to the direction of applied axial loads. As shown in Fig. 4.1, the local coordinate system of a lamina consist of three mutually orthogonal axes: an axis 1 along the direction of the fibres, an axis 2 transversal to the direction of the fibres and parallel to the lamina mid-plane, and an axis 3 through-the-thickness of the lamina.

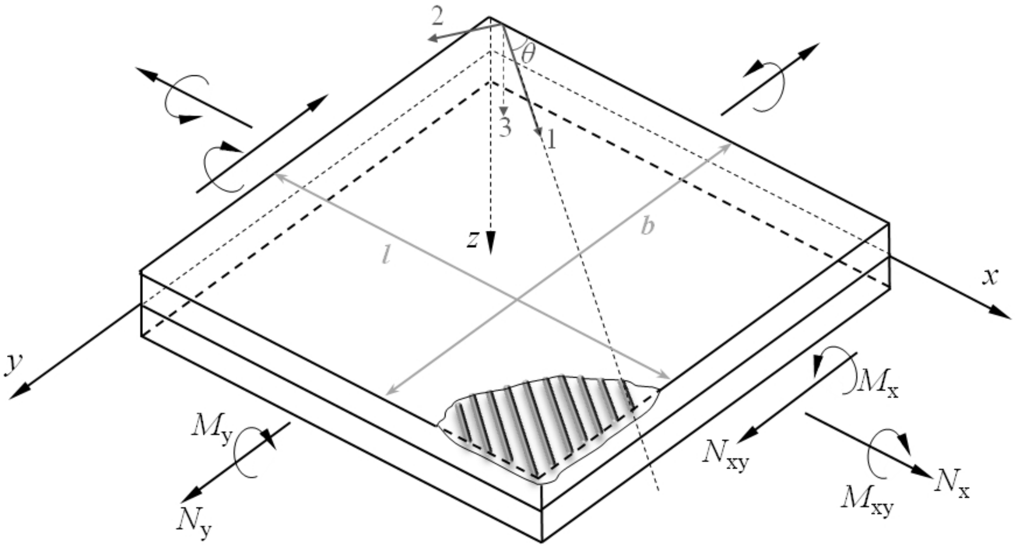

Figure 4.1: Schematic of the in-plane loads for a uniaxial FRPC laminate showing the global coordinate system of x, y, and z mid-plane axes and the top lamina local coordinate system of 1, 2, and 3 axes

Conventionally, the in-plane loads (forces and moments) applied to the FRPC laminate are normalized in order to obtain the laminate distributed loads per unit of width, which are defined as follows and in reference to Fig. 4.1 [119, 135]:

$$N_{\mathrm{x}} = \int_{-h/2}^{h/2} \sigma_{\mathrm{x}} dz \ , \tag{4}$$

$$N_{\mathrm{y}} = \int_{-h/2}^{h/2} \sigma_{\mathrm{y}} dz \ , \tag{5}$$

$$N_{\mathrm{xy}} = \int_{-h/2}^{h/2} \tau_{\mathrm{xy}} dz \ , \tag{6}$$

$$M_{\mathrm{x}} = \int_{-h/2}^{h/2} z\sigma_{\mathrm{x}} dz \ , \tag{7}$$

$$M_{\mathrm{y}} = \int_{-h/2}^{h/2} z\sigma_{\mathrm{y}} dz \ , \tag{8}$$

$$M_{\mathrm{xy}} = \int_{-h/2}^{h/2} z\tau_{\mathrm{xy}} dz \ , \tag{9}$$

where z is the coordinate in the laminate mid-plane z-axis and the subscript of the normal stress σ and shear stress τ correspond to the Cauchy stress tensor components in the directions of the coordinate system of x, y, and z axes. The FRPC laminate distributed axial forces, N_{x} and N_{y}, shear force, N_{xy}, bending moment, M_{x}, and twisting moment, M_{xy}, can be related to the resulting Cauchy strain (engineering strain) components, $\varepsilon_{\mathrm{x}}^{0}$, $\varepsilon_{\mathrm{y}}^{0}$, and γ_{xy}^{0} , and deflection curvatures, κ_{x}, κ_{y}, and κ_{xy}, in the mid-plane of the FRPC with respect to the x-y-z coordinate system as follows [119, 135]:

$$\begin{bmatrix} N_{\mathrm{x}} \\ N_{\mathrm{y}} \\ N_{\mathrm{xy}} \\ M_{\mathrm{x}} \\ M_{\mathrm{y}} \\ M_{\mathrm{xy}} \end{bmatrix} = \begin{bmatrix} A_{11} & A_{12} & A_{16} & B_{11} & B_{12} & B_{16} \\ A_{12} & A_{22} & A_{26} & B_{12} & B_{22} & B_{26} \\ A_{16} & A_{26} & A_{66} & B_{16} & B_{26} & B_{66} \\ B_{11} & B_{12} & B_{16} & D_{11} & D_{12} & D_{16} \\ B_{12} & B_{22} & B_{26} & D_{12} & D_{22} & D_{26} \\ B_{16} & B_{26} & B_{66} & D_{16} & D_{26} & D_{66} \end{bmatrix} \begin{bmatrix} \varepsilon_{\mathrm{x}}^{0} \\ \varepsilon_{\mathrm{y}}^{0} \\ \gamma_{\mathrm{xy}}^{0} \\ \kappa_{\mathrm{x}} \\ \kappa_{\mathrm{y}} \\ \kappa_{\mathrm{xy}} \end{bmatrix} = \begin{bmatrix} \mathbf{A} & \mathbf{B} \\ \mathbf{B} & \mathbf{D} \end{bmatrix} \begin{bmatrix} \varepsilon_{\mathrm{x}}^{0} \\ \varepsilon_{\mathrm{y}}^{0} \\ \gamma_{\mathrm{xy}}^{0} \\ \kappa_{\mathrm{x}} \\ \kappa_{\mathrm{y}} \\ \kappa_{\mathrm{xy}} \end{bmatrix}, \tag{10}$$

where **A**, **B**, and **D** are the 3 x 3 extensional, coupling, and bending stiffness matrices, respectively. The constitutive CLT model in Eq. (10) describes a linear relationship between global in-plane loads and deformations in the FRPC laminate, which is based on the following assumptions [117, 119, 136]:

- A straight and perpendicular line to the mid-plane of the FRPC laminate remains straight and perpendicular to the mid-plane during deformation ($\gamma_{\mathrm{xz}}^{0} = \gamma_{\mathrm{yz}}^{0}$=0),
- Linear elasticity, orthotropy, and macroscopic homogeneity is exhibited by each lamina,
- The FRPC laminate thickness is small compared to the width and the length of the sample (usually 10 - 15%),
- Displacements in the *x*, *y*, and *z* directions are continuous and small compared to the FRPC laminate thickness,
- No slippage occurs between the lamina interfaces during deformation,
- The FRPC laminate mid-plane is in a plane stress state ($\sigma_{\mathrm{z}} = \tau_{\mathrm{yz}} = \tau_{\mathrm{xz}} = 0$)

In order to define the terms of the stiffness matrix in Eq. (10), a general FRPC laminate of thickness h_{L} and stacking sequence of k = 1,2,..., g laminae is considered. Figure 4.2 shows a schematic cross-section of the general FRPC architecture showing the stacking sequence of k = 1,2,...,g laminae of thickness h_k to form a laminate of thickness h_{L}. In reference to Fig. 4.2, the terms of the **A**, **B**, and **D** matrices can be calculated as follows [135]:

$$A_{ij} = \sum_{k=1}^{g} [(\overline{Q}_{ij})]_k h_k \ , \quad i = 1,2,6; \quad j = 1,2,6 \ , \tag{11}$$

$$B_{ij} = \sum_{k=1}^{g} [(\overline{Q}_{ij})]_k h_k \underline{z}_k \ , \quad i = 1,2,6; \quad j = 1,2,6 \ , \tag{12}$$

$$D_{ij} = \sum_{k=1}^{g} [(\overline{Q}_{ij})]_k \left(h_k \underline{z}_k^2 + \frac{h_k^3}{12} \right), \quad i = 1,2,6; \quad i = 1,2,6 \ , \tag{13}$$

where h_{k} is the thickness of the k-th lamina, $\underline{z}_k$ is the z coordinate (positive or negative) of the centroid of the k-th lamina from the mid-plane of the FRPC laminate, and $\overline{Q}_{ij}$ (i,j = 1,2,6 and $\overline{Q}_{ij} = \overline{Q}_{ji}$) are the transformed reduced stiffness constants of each orthotropic lamina [119]. For each lamina (k = 1,2,..., g) in the general FRPC laminate structure shown in Fig. 4.2, the transformed reduced stiffness constants $\overline{Q}_{ij}$ (i,j = 1,2,6 and $\overline{Q}_{ij} = \overline{Q}_{ji}$) are a function of the lamina reduced stiffness coefficients Q_{ij} (i,j = 1,2,6 and $Q_{ij} = Q_{ji}$) and the in-plane angle θ with respect to the global x-axis [119] (Fig. 4.1). Using the coordinate system shown in Fig. 4.1, the transformed reduced stiffness constants $\overline{Q}_{ij}$ (i,j = 1,2,6 and $\overline{Q}_{ij}=\overline{Q}_{ji}$) are defined as:

$$\overline{Q}_{11}=Q_{11}\cos^4(\theta)+Q_{22}\sin^4(\theta)+2(Q_{12}+2Q_{66})\sin^2(\theta)\cos^2(\theta)\,, \tag{14}$$

$$\overline{Q}_{12}=(Q_{11}+Q_{22}-4Q_{66})\sin^2(\theta)\cos^2(\theta)+Q_{12}(\cos^4(\theta)+\sin^4(\theta)), \tag{15}$$

$$\overline{Q}_{22}=Q_{11}\sin^4(\theta)+Q_{22}\cos^4(\theta)+2(Q_{12}+2Q_{66})\sin^2(\theta)\cos^2(\theta)\,, \tag{16}$$

$$\overline{Q}_{16}=(Q_{11}-Q_{12}-2Q_{66})\cos^3(\theta)\sin(\theta)-(Q_{22}-Q_{12}-2Q_{66})\sin^3(\theta)\cos(\theta)\,, \tag{17}$$

$$\overline{Q}_{26}=(Q_{11}-Q_{12}-2Q_{66})\sin^3(\theta)\cos(\theta)-(Q_{22}-Q_{12}-2Q_{66})\cos^3(\theta)\sin(\theta)\,, \tag{18}$$

$$\overline{Q}_{66}=(Q_{11}+Q_{22}-2Q_{12}-2Q_{66})\sin^2(\theta)\cos^2(\theta)+Q_{66}(\sin^4(\theta)+\cos^4(\theta)), \tag{19}$$

$$Q_{11}=\frac{E_1}{1-\nu_{12}\nu_{21}}\ , \tag{20}$$

$$Q_{12}=\frac{\nu_{12}E_2}{1-\nu_{12}\nu_{21}}\ , \tag{21}$$

$$Q_{22}=\frac{E_2}{1-\nu_{12}\nu_{21}}\ , \tag{22}$$

$$Q_{66}=G_{12}\ , \tag{23}$$

where E_1 is the Young's modulus in the axis 1 direction of the lamina (along the orientated fibres), E_2 is Young's modulus in the axis 2 direction of the lamina, G_{12} is the in-plane shear modulus, and ν_{12} and ν_{21} are the major and minor Poisson ratios of the lamina in the local 1-2-3 coordinate system, respectively. The existence of different Young's moduli (E_1 and E_2) and Poisson ratios (ν_{12} and ν_{21})

is a consequence of the orthotropic mechanical properties of each lamina [119, 135].

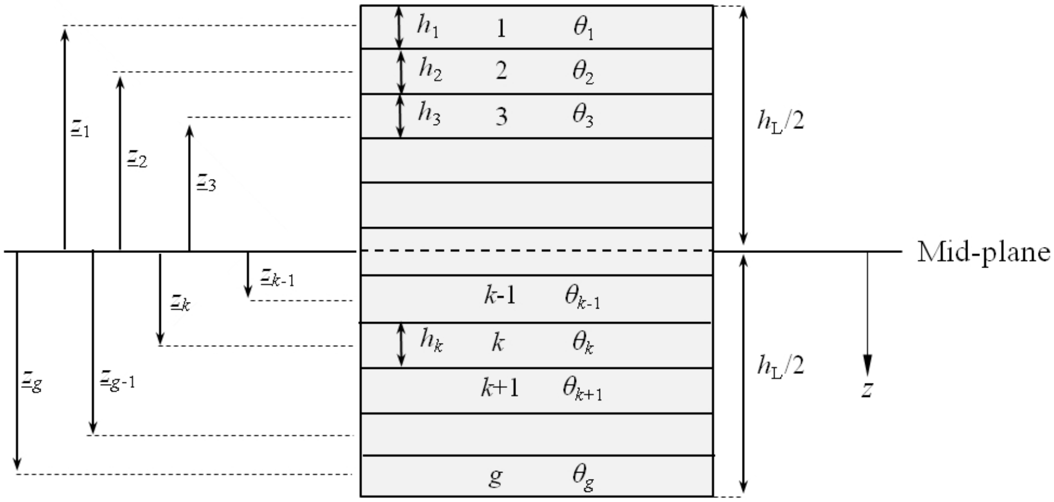

Figure 4.2: Schematic cross-section of the general FRPC architecture showing the stacking sequence of k=1,2,...,g laminae of in-plane angle θ_k and thickness h_k, which results in a laminate structure of total thickness h_L

Based on the constitutive CLT model presented in Eq. (10), a flame-sprayed Al-12Si coating layer of thickness, h_c, width, b, and length, l, may be envisaged as an isotropic lamina [121] (equivalent to an orthotropic lamina with $E_1 = E_2$ and $v_{12} = v_{21}$) as part of the coated FRPC laminate structure. If symmetric coating deposition is performed onto the FRPC laminate, then the flame-sprayed Al-12Si layers would correspond to lamina 1 and g in Fig. 4.2.

Considering a flame spray coated and symmetric FRPC laminate in which the material, in-plane angle, and thickness of the laminae are the same above and below the mid-plane, no coupling between forces and bending moments exists [119, 135]. This results in all terms of the **B** coupling matrix being equal to zero in Eq. (10). The term coated s-FRPC is henceforth used in this study to refer to a symmetric FRPC laminate in which the top and bottom laminae constitute flame-sprayed Al-12Si coatings, as illustrated in Fig. 4.2. Assuming the mid-plane shear strain γ_{xy}^{0} is negligible, the mechanical behaviour of the coated s-FRPC under uniaxial tension along the x axis ($N_y = N_{xy} = M_x = M_y = M_{xy} = 0$) can be expressed as:

$$N_x = A_{11}\varepsilon_x^0 + A_{12}\varepsilon_y^0 \ , \tag{24}$$

$$N_y = 0 = A_{12}\varepsilon_x^0 + A_{22}\varepsilon_y^0 \ , \tag{25}$$

or

$$N_x = \left(A_{11} - \frac{(A_{12})^2}{A_{22}} \right)\varepsilon_x^0 = \alpha\varepsilon_x^0 \ , \tag{26}$$

where A_{11}, A_{12}, and A_{22} are terms of the extensional stiffness matrix **A** in Eq. (10) and Eq. (11), and α is the uniaxial laminate stiffness of the coated s-FRPC along the x-axis, which is defined as the ratio between the laminate distributed load N_x and the mid-plane laminate axial strain ε_x^0 (Fig. 4.1). As shown in Eq. (10), the bending stiffness matrix **D** does not influence the mechanical behaviour of coated s-FRPC under uniaxial tension, since no moments loads (M_x, M_y, M_{xy}) are applied to the laminate.

Using Eq. (11), Eq. (26), and Eqs. (14) - (16) reveals that the uniaxial laminate stiffness of the coated s-FRPC, α, is a function of the reduced stiffness constants (i,j = 1,2 and $Q_{ij} = Q_{ji}$) of the flame-sprayed Al-12Si coating and FRPC substrate. Also, the determination of the value of α from substrate and coating parameters using the CLT model in Eq. (26) can be evaluated experimentally by tensile testing of the coated s-FRPC specimen along the x-axis. It is conceivable to consider the inversion problem and determine the value of one of the reduced stiffness constants of a lamina in the flame-sprayed FRPC substrate, i.e. Q_{11}, Q_{12}, or Q_{22}, from the measured value of α and Eq. (26) if the remaining reduced stiffness constants, laminate architecture (Fig. 4.2), and geometric parameters (l, b, h_k ($k = 1,2,...,g$)) of the coated s-FRPC are known [137]. As shown in Eqs. (14)-(16), further reduction of the inversion problem for the coated s-FRPC structure in Eq. (26) can be achieved by measuring α through tensile tests with all fibre-reinforced laminae oriented at an in-plane angle of $\theta = 0°$ or $\theta = 90°$ with respect to the x-axis (which yields sin(θ) and cos(θ) equal to 0 or 1) since the stiffness of the isotropic flame-sprayed Al-12Si coating remains constant for all values of θ [119].

Considering the tensile testing of coated s-FRPC specimens oriented at an in-plane angles of $\theta = 0°$ and $\theta = 90°$, it is possible to construe two independent equations using the measured values of α in tandem with Eq. (26). Using the relationship $Q_{12} = v_{12} \cdot Q_{22}$ from Eqs. (21) and (22), the two independent equations of the coated s-FRPC specimens can be expressed as:

$$N_{\mathrm{x}} = \left(2Q' h_{\mathrm{c}} + Q_{11} h_{0^\circ} - \frac{(2v' Q' h_{\mathrm{c}} + v_{12} Q_{22} h_{0^\circ})^2}{2Q' h_{\mathrm{c}} + Q_{22} h_{0^\circ}} \right) \varepsilon_{\mathrm{x}}^{0} = \alpha_1 \varepsilon_{\mathrm{x}}^{0}, \tag{27}$$

for [0°$_g$] laminate architectures of k=1,2,...,g laminae (Fig. 4.2), and

$$N_{\mathrm{x}} = \left(2Q' h_{\mathrm{c}} + Q_{22} h_{90^\circ} - \frac{(2v' Q' h_{\mathrm{c}} + v_{12} Q_{22} h_{90^\circ})^2}{2Q' h_{\mathrm{c}} + Q_{11} h_{90^\circ}} \right) \varepsilon_{\mathrm{x}}^{0} = \alpha_2 \varepsilon_{\mathrm{x}}^{0}, \tag{28}$$

for [90°$_g$] architectures (k = 1,2,...,g), where α_1 is the uniaxial laminate stiffness of the coated s-FRPC of [0°$_g$] architecture, α_2 is the uniaxial laminate stiffness of the coated s-FRPC of [90°$_g$] architecture, Q' is the reduced stiffness constant of the flame-sprayed Al-12Si coating, v' is the Poisson ratio of the flame-sprayed Al-12Si coating, h_{c} is the thickness of the flame-sprayed Al-12Si coating, h_{0° is the thickness of the laminae oriented at an in-plane angles of $\theta = 0°$, h_{90° is the thickness of the laminae oriented at an in-plane angles of $\theta = 90°$, v_{12} is the major Poisson ratio of the flame-sprayed FRPC substrate, and Q_{11} and Q_{22} are the reduced stiffness constants of the flame-sprayed FRPC substrate defined in Eq. (20) and Eq. (22), respectively.

In Eqs. (27) and (28), the value of Q' and v' may be measured from tensile tests with flame-sprayed Al-12Si films using Digital Image Correlation (DIC) [132, 134, 138-140]. Assuming that the major Poisson ratio of the flame-sprayed FRPC substrate v_{12} can be estimated independently (e.g., via a separate experimental procedure), the system of equations shown in Eqs. (27) and (28) is an inversion problem which can be solved using the coated s-FRPC tensile data and geometric parameters to determine the values of the reduced stiffness constants Q_{11} and Q_{12} of the flame-sprayed FRPC substrate. An estimate of the v_{12} value in Eq. (27) and Eq. (28) may be obtained by DIC measurements during tensile tests of the substrate after exposure to flame-sprayed Al-12Si particles. The solution to the inversion problem given by Eqs. (27) and (28) provides a description of the mechanical behaviour of coated s-FRPC specimens of general h_L thickness based on the CLT model (Fig. 4.2 and Eq. (26)), which can be evaluated using experimental results with different laminate architectures and geometric dimensions for validation purposes.

4.3 Experimental method

4.3.1 Fiber-reinforced polymer composite fabrication

Symmetric FRPC laminates of $[0°_8]$, $[90°_8]$, $[90°_2/0°_2]_S$, and $[0°_{10}]$ architectures were created by manual lay up of E-glass prepreg plies (Cycom 1003, Cytec Engineered Materials, Woodland Park, NJ, USA). Fibre-reinforced polymer laminates of $[90°_2/0°_2]_S$ and $[0°_{10}]$ architectures were fabricated for experimental validation purposes. Curing of the prepreg laminates was performed in an oven at 166 °C for one hour. The cured laminates were cut to produce rectangular FRPC specimens of dimensions l=254 mm in length and b=25.4 mm in width, as per ASTM standard D3039 [141]. A designated 50.8 mm gauge length was set in the midsection of the FRPC specimen. Seven [$0°_8$], three [$90°_8$], four [$0°_{10}$], and four [$90°_2/0°_2$]$_S$ FRPC specimens were produced. Two 25.4 mm x 25.4 mm samples of each laminate architecture were randomly selected during the cutting of the FRPC specimens. The fibre volume fraction V_f of each laminate architecture was estimated using the average weight of the sample before and after burnout of the matrix phase inside an oven set at 540 °C for 4 hours, as per the following formula:

$$V_{\mathrm{f}} = \frac{\dfrac{m_{\mathrm{f}}}{\rho_{\mathrm{f}}}}{\dfrac{m_{\mathrm{f}}}{\rho_{\mathrm{f}}} + \dfrac{m_{\mathrm{m}}}{\rho_{\mathrm{m}}}}, \tag{29}$$

where m_f and m_m are the masses, and ρ_f and ρ_m are the densities of the fibre and matrix, respectively. A high strength epoxy adhesive (Scotch Weld DP460 Off White, 3M, St. Paul, MN, USA) was applied onto the FRPC specimen to bond tensile grips and incorporate a layer of sprinkled 80-grit (~165 µm) garnet sand, as shown in Fig.4.3. The garnet sand was used as an inexpensive roughening agent to promote adhesion of the spray-deposited Al-12Si particles and mitigate thermal degradation of the polymer-based substrate [83, 102, 142]. Preparation steps involving the tensile grips and the garnet sand were performed on the two opposite sides of each FRPC specimen in preparation for flame spraying of Al-12Si particles.

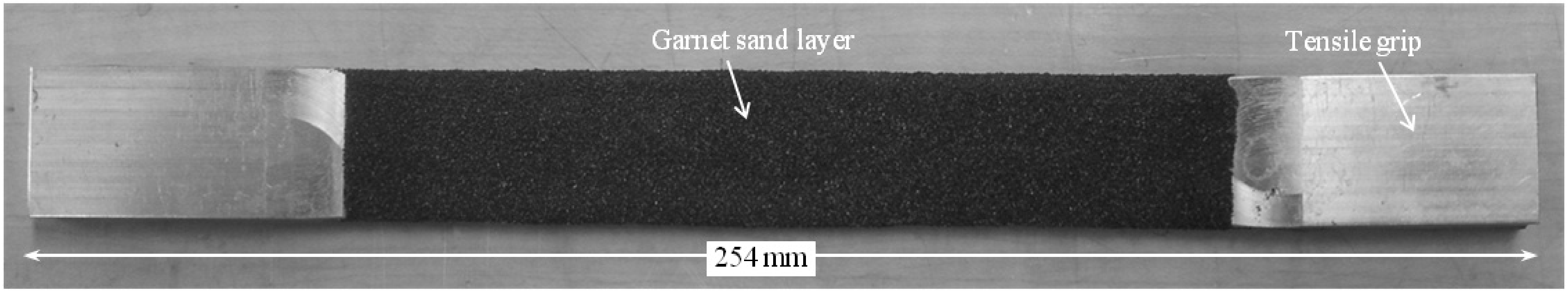

Figure 4.3: Prepared FRPC for flame spraying of Al-12Si particles

4.3.2 Flame spraying of Al-12Si particles

An oxy-acetylene flame spray torch (6P II, Oerlikon Metco, Winterthur, Zürich, Switzerland) was attached to a Motoman robot arm (HP20, Yaskawa Electric Corporation, Fukuoka, Japan) and used to generate a combustion flame from a mixture of 8 NLPM (normal liters per minute) of acetylene and 25 NLPM of oxygen. A spheroidal aluminium-12silicon (Al-12Si) powder, consisting of aluminium particles ranging from 45 µm to 90 µm in diameter (52C NS, Oerlikon Metco, Winterthur, Zürich, Switzerland), was injected into the flame spray torch using a volumetric powder feed unit (5MPE, Sulzer Metco, Westbury, NY, USA). Injection of the Al-12Si particles into the flame spray torch was performed using argon as the carrier gas, at a pressure of 515 kPa (60 psig) and 0.4 m^3/h (15 standard cubic feet per hour), which resulted in a powder flow meter reading of 90 on the powder feed unit. Flame spraying of Al-12Si particles was performed to deposit the coatings on to the FRPC specimens and to create spray-formed and free-standing flame-sprayed Al-12Si films.

4.3.2.1 Flame-sprayed FRPC specimens

Flame spraying of FRPC specimens allowed the fabrication of $[0°_8]$ FRPC specimens exposed to the flame spray and coated s-FRPC specimens. An aluminium tape (438, 3M, St. Paul, MN, USA) was used to cover the garnet sand roughened surface of three randomly selected $[0°_8]$ FRPC specimens. The aluminium tape acted as a barrier to prevent the deposition of Al-12Si particles onto the substrate while exposing the prepared [$0°_8$] FRPC specimen to the flame spray, as shown in Fig.4.4. The FRPC specimen was fixed to a support plate at room temperature using thermal spray tape (170 10S Red, Green Belting Industries, Mississauga, ON, Canada). Fifteen FRPC specimens remained devoid of the aluminium tape barrier, which allowed the fabrication of coated s-FRPC specimens. Flame spraying of the FRPC specimen was performed at a stand-off distance of 150 mm from the flame spray torch. The flame spray torch travelled linearly and parallel to the length of the FRPC specimen and performed horizontal deposition passes at 500 mm/s, with vertical steps of 7 mm between each pass. Three deposition passes were executed with a 5-minute cooling period between consecutive passes. Flame spraying of Al-12Si particles was performed on the two opposite sides of the FRPC specimen. Figure 4.5 illustrates a coated s-FRPC specimen and flame spray exposed [$0°_8$] FRPC specimen.

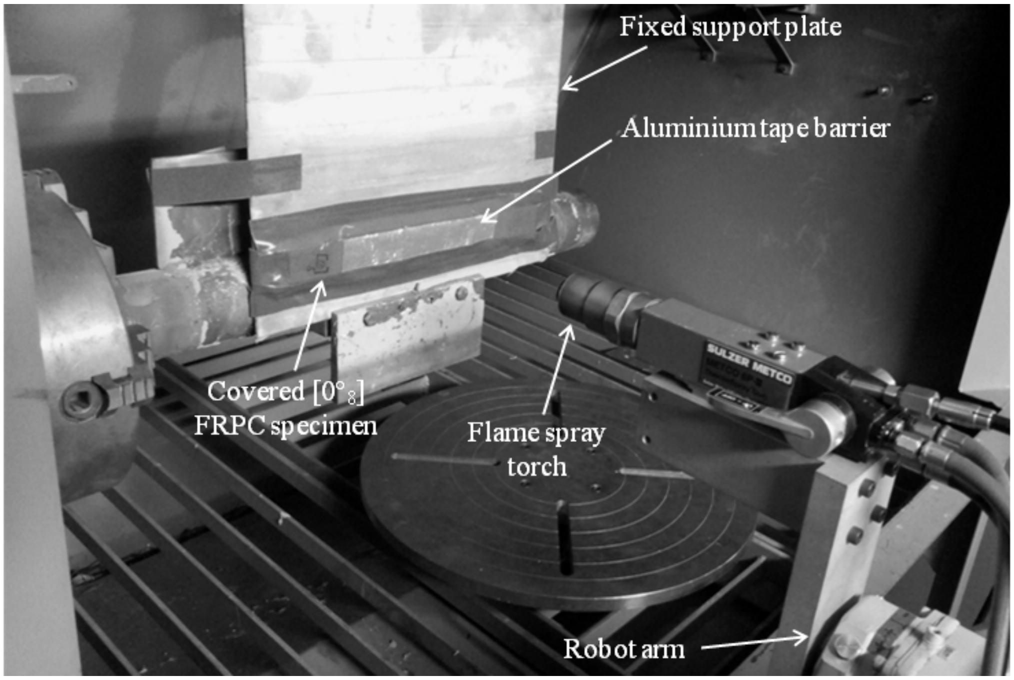

Figure 4.4: Experimental assembly for exposing the prepared [0°$_8$] FRPC specimen to flame-sprayed Al-12Si particles

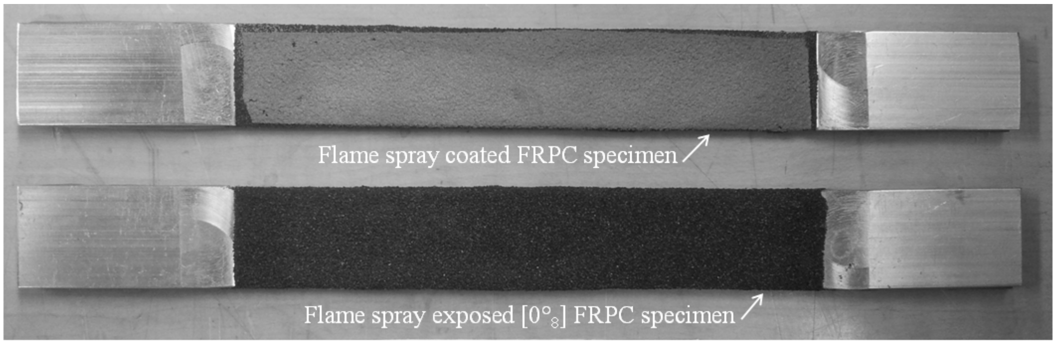

Figure 4.5: Illustration of FRPC specimens post-flame spraying of Al-12Si particles, including a coated s-FRPC specimen and a flame spray exposed [0°$_8$] FRPC specimen

4.3.2.2 Flame-sprayed Al-12Si films

Three metal plates were covered with thermal spray tape and used to assemble a mould for the fabrication of spray-formed free-standing flame-sprayed Al-12Si films, as shown in Fig. 4.6. The mould had two deposition grooves for film fabrication using identical process parameters to those utilized to flame spray Al-12Si onto FRPC specimens. The deposition groove allowed for the consolidation of flame-sprayed Al-12Si particles to form a dimensioned free-standing film of l = 101.5 mm (4 inches) in length and b = 6.35 mm (0.25 inches) in width, as per ASTM Standard E8/E8M [143]. As shown in Fig. 4.6(a), a removable divider block separated the two deposition grooves to facilitate the extraction of the flame-sprayed Al-12Si films. As shown in Fig. 4.6(b), separation of the two smaller plates of the mould exposed the flame-sprayed Al-12Si film laid onto the thermal spray tape. Acetone was applied to clean the specimen and reduce the interfacial friction between the thermal spray tape surface and the flame-sprayed Al-12Si film. Careful extraction of the flame-sprayed Al-12Si film was performed using a laboratory spatula. Four flame-sprayed Al-12Si films were fabricated. Paper sheet tensile grips (Premium copy paper #99115, Grand&Toy, Toronto, ON, Canada) were bonded to opposite sides of three flame-sprayed Al-12Si films, as shown in Fig. 4.7. A designated gauge length of 25.4 mm remained exposed in the midsection of the flame-sprayed Al-12Si film. The paper sheet midsections located next to the gauge length of the flame-sprayed Al-12Si film were cut with detail scissors prior to the application of tensile loads.

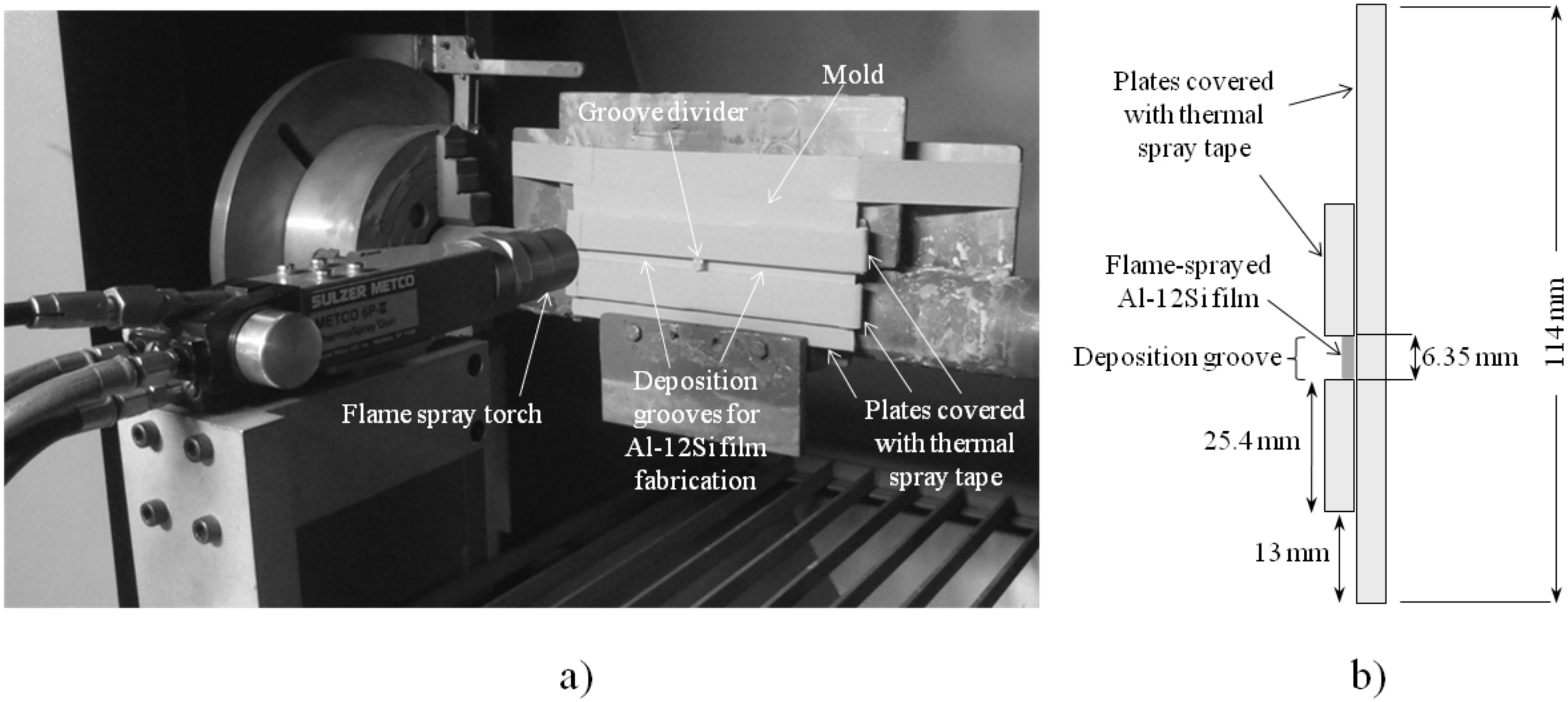

Figure 4.6: Experimental assembly for fabrication of free-standing flame-sprayed Al-12Si films, showing a) the support fixture elements and b) a schematic side view of the flame-sprayed Al-12Si film consolidated onto the mold

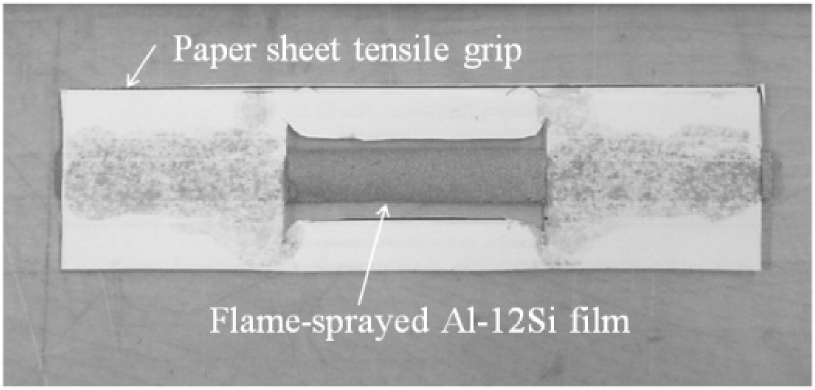

Figure 4.7: Free-standing flame-sprayed Al-12Si film bonded to paper sheet grips

4.3.3 Tensile testing

4.3.3.1 Flame-sprayed Al-12Si films

A 500-N capacity mechanical testing equipment (Synergie 400, MTS, Eden Prairie, MN, USA) was utilized to apply tensile loads to the flame-sprayed Al-12Si films at room temperature. Monotonic loading of the flame-sprayed Al-12Si films were performed at a rate of 0.05 mm/min. The experimental assembly that was used to perform tensile tests on the flame-sprayed Al-12Si films is shown in Fig. 4.8. The axial and transversal strains of the flame-sprayed Al-12Si film were measured simultaneously using the DIC technique [139, 144] with no speckle pattern applied to the surface of the flame-sprayed Al-12Si film. Images of the tensile specimen were recorded using a high resolution camera (piA2400-17gm, Basler AG, Ahrensburg Germany) equipped with a 50 mm camera lens (NVM-50, Navitar Inc., Rochester, NY, USA). As shown in Fig 4.8(b), a 25 mm extension tube (CML25 C-Mount Extension Tube, ThorLabs, Newton, NJ, USA) was used to reduce the working distance between the Al-12Si film and the camera lens. Sample images of the flame-sprayed Al-12Si film were acquired at a rate of 1 image per second until structural failure of the specimen occurred. The effective resolution of the DIC apparatus was estimated at 0.01% strain. The collected image sequences were processed using a commercial software package (DaVis version 8.1.1 StrainMaster 3D, LaVision GmbH, Gottingen, Germany) to measure displacement and strain fields in the flame-sprayed Al-12Si film surface using a 64 x 64 correlation window. Processing of the tensile and DIC data provided the applied load, F, and strains, ε_x^0 and ε_y^0, in the gauge section of the Al-12Si film at a frequency of 2 Hz.

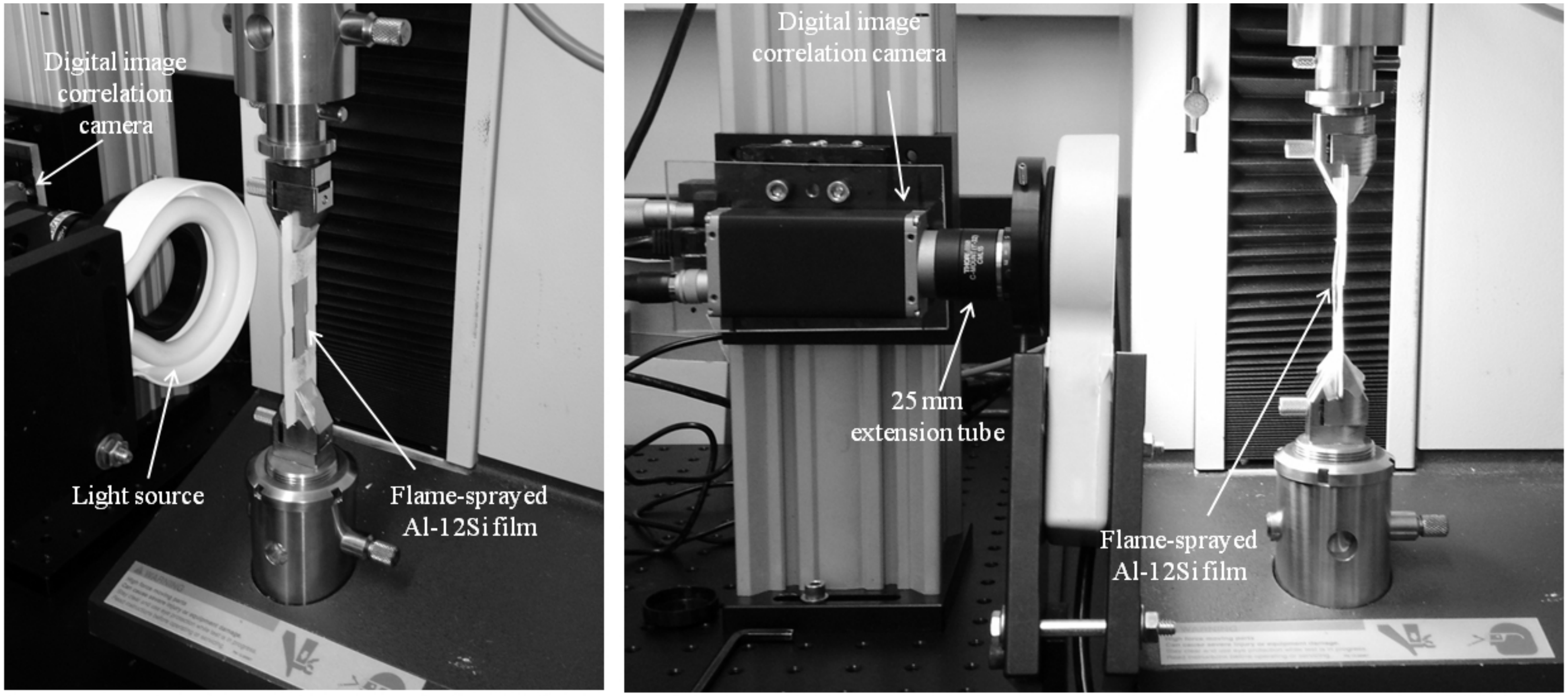

a)

b)

Figure 4.8: Experimental assembly for tensile testing of free-standing flame-sprayed Al-12Si films showing a) the tensile specimen before the application of loads and b) the digital image correlation equipment used to measure strain

4.3.3.2 Flame-sprayed FRPC specimens

A 100-kN capacity uniaxial testing machine (810, MTS Systems Corporation, Eden Prairie, MN, USA) was used to apply axial tensile load to the coated s-FRPC specimens and flame-spray exposed $[0°_8]$ FRPC specimens at room temperature. Monotonic loading of the FRPC tensile specimen was performed at a stroke rate of 0.059 mm/min. As shown in Fig. 4.9(a), a 12.7 mm gauge length extensometer (634.31, MTS Systems Corporation, Eden Prairie, MN, USA) was installed on the thin edge of the coated s-FRPC specimen to measure the axial strain ε_x^0. The DIC technique was used to measure the axial (ε_{ex}) and transversal (ε_{ey}) strains of flame spray exposed $[0°_8]$ FRPC specimens [140], as shown in Fig. 4.9(b). DIC measurements were performed using a high resolution camera (piA2400-17gm, Basler AG, Ahrensburg Germany) equipped with a 50 mm camera lens (NVM-50, Navitar Inc., Rochester, NY, USA). No surface speckle pattern was applied to the garnet-roughened surface of the flame spray exposed $[0°_8]$ FRPC specimen to perform DIC measurements. The applied load (F) and measured strains in the FRPC tensile specimen were recorded at a frequency of 2 Hz until structural failure occurred.

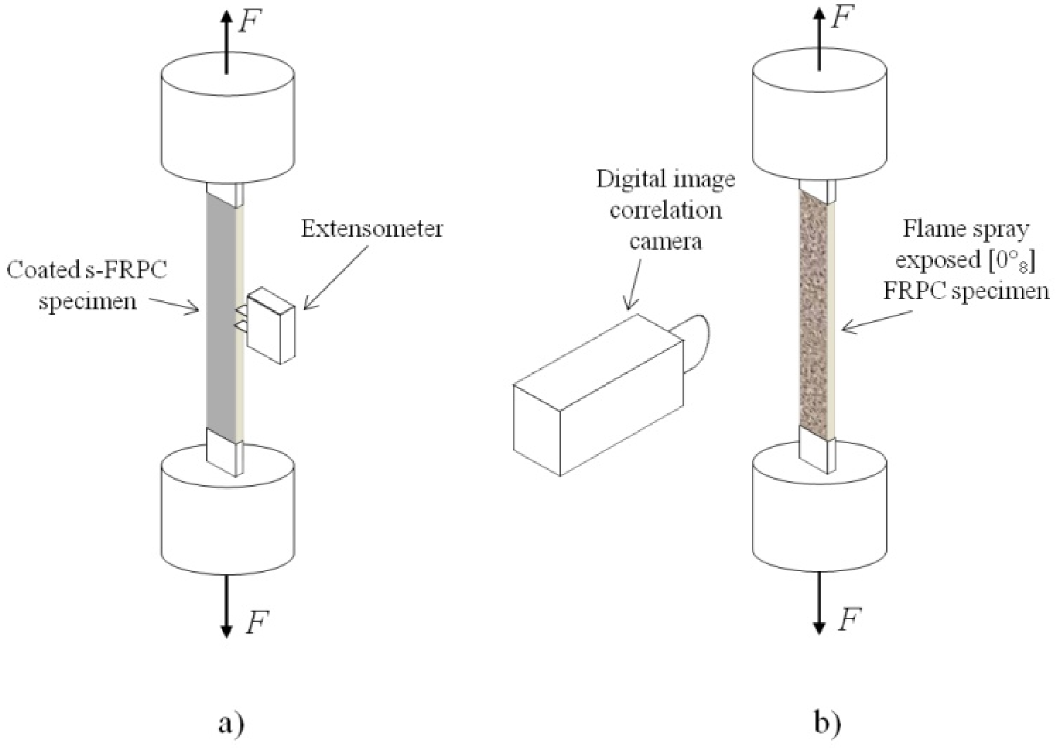

Figure 4.9: Schematic of the tensile test apparatus for a) coated s-FRPC specimens and b) flame spray exposed [0°$_8$] FRPC specimens

4.3.4 Estimation of laminate stiffness and mechanical properties

Post-processing of the load and strain data was performed using the Origin 2015 software (OriginLab Corporation, Northampton, MA, USA) to determine the maximum strain value in the linear load-strain range of tensile FRPC specimens (coated and exposed) and flame-sprayed Al-12Si films. The mechanical properties of the flame-sprayed Al-12Si coating were estimated from the tensile data of flame-sprayed Al-12Si films. For each tensile specimen, the laminate distributed load, N_x, was calculated as the applied tensile force F divided by the in-plane transversal (width) dimension to the axial axis, *b*, according to the following expression [119, 137]:

$$N_{\mathrm{x}} = \frac{F}{b} = \underline{E}_{\mathrm{x}} h_{\mathrm{L}} \varepsilon_{\mathrm{x}}^{0}, \tag{30}$$

where $\underline{E}_{\mathrm{x}}$ is the effective Young's modulus of the tensile specimen in the axial (longitudinal) direction, $\varepsilon_{\mathrm{x}}^{0}$ is the measured axial strain, and h_{L} is the total thickness of the tensile specimen (see Fig. 4.2). The uniaxial laminate stiffness, *α*, was estimated from the laminate distributed load (N_{x}) and axial strain ($\varepsilon_{\mathrm{x}}^{0}$) data in the linear load-strain range, using simple linear regression through the origin based on the least squares approach [145, 146]:

$$\underline{\alpha} = \frac{\sum_{i=1}^{m} (\varepsilon_{\mathrm{x}}^{0})_i (N_{\mathrm{x}})_i}{\sum_{i=1}^{m} (\varepsilon_{\mathrm{x}}^{0})_i^2}, \tag{31}$$

where $\underline{\alpha}$ is the estimate of the uniaxial laminate stiffness and *m* is the number of recorded data points. The statistical coefficient of determination [146], r^2, was calculated for estimated $\underline{\alpha}$ value in Eq. (31) as [145]:

$$r^2 = \frac{\sum_{i=1}^{m} (\alpha \cdot \varepsilon_{\mathrm{x}}^{0})_i^2}{\sum_{i=1}^{m} (N_x)_i^2}, \text{ for } \underline{\alpha}. \tag{32}$$

Using Eqs. (26), (30), and (31), the effective Young's modulus $\underline{E}_{\mathrm{x}}$ in the axial direction of tensile specimens was calculated as:

$$\underline{E}_{\mathrm{x}} = \frac{\underline{\alpha}}{h_{\mathrm{L}}}, \tag{33}$$

where $\underline{\alpha}$ and h_{L} are defined as per Eq. (31) and Fig. 4.2, respectively.

The major Poisson ratio of the flame spray exposed [0°$_8$] FRPC specimens and the Poisson ratio of flame-sprayed Al-12Si films was estimated using the strain rates of the strain-time data during the tensile test and performing simple linear regression through the origin. The strain rates in the axial, β_{x}, and transversal, β_{y}, directions (Fig. 4.1) of the flame-sprayed Al-12Si films and flame spray exposed [0°$_8$] FRPC specimens were calculated using the following expressions [145]:

$$\beta_{\mathrm{x}} = \frac{\sum_{i=1}^{m} (t)_i (\varepsilon_{\mathrm{x}}^0)_i}{\sum_{i=1}^{m} (t)_i^2}, \tag{34}$$

$$\beta_{\mathrm{y}} = \frac{\sum_{i=1}^{m} (t)_i (\varepsilon_{\mathrm{y}}^0)_i}{\sum_{i=1}^{m} (t)_i^2}, \tag{35}$$

where m is the number of recorded data points, t is the recorded time in the strain-time data, and $\varepsilon_{\mathrm{x}}^0$ and $\varepsilon_{\mathrm{y}}^0$ correspond to the Cauchy strains in axial and transversal directions, respectively. The following formulae were utilized to calculate the corresponding statistical coefficient of determination r^2 for the strain rate estimates [145]:

$$r^2 = \frac{\sum_{i=1}^{m} (\beta_{\mathrm{x}} \cdot t)_i^2}{\sum_{i=1}^{m} (\varepsilon_{\mathrm{x}}^0)_i^2}, \text{ for } \beta_{\mathrm{x}}, \tag{36}$$

$$r^2 = \frac{\sum_{i=1}^{m} (\beta_{\mathrm{y}} \cdot t)_i^2}{\sum_{i=1}^{m} (\varepsilon_{\mathrm{y}}^0)_i^2}, \text{ for } \beta_{\mathrm{y}}. \tag{37}$$

The axial strain rate β_{x} (Eq. (34)) and transversal strain rate β_{y} (Eq. (35)) values allowed the calculation of the major Poisson ratio of each flame spray exposed [0°$_8$] FRPC specimen, ν_{12}^e, as follows:

$$\nu_{12}^e = -\frac{\varepsilon_{\mathrm{y}}^0}{\varepsilon_{\mathrm{x}}^0} = -\frac{\beta_{\mathrm{y}}}{\beta_{\mathrm{x}}}. \tag{38}$$

Considering the potential mechanical degradation effect in the flame spray exposed [0°$_8$] FRPC specimen due to the thermal gradient induced by flame spray torch passes, the value of ν_{12}^e in Eq. (38) was used as an estimator of the major Poisson ratio of the flame-sprayed FRPC substrate in coated s-FRPC specimens, that is:

$$\nu_{12} \approx \nu_{12}^e. \tag{39}$$

Using Eq. (20), the reduced stiffness constant of the isotropic flame-sprayed Al-12Si coating, Q' was estimated as follows:

$$Q' = \frac{E_c}{1-(\nu')^2}, \tag{40}$$

where E_c is the effective Young's Modulus (Eq. (33)) and v' is the Poisson ratio (Eq. (38)) of the flame-sprayed Al-12Si film. The Poisson ratio of the flame-sprayed Al-12Si film was estimated as:

$$\nu' = -\frac{\varepsilon'^{0}_{\mathrm{y}}}{\varepsilon'^{0}_{\mathrm{x}}} = -\frac{\beta'_{\mathrm{y}}}{\beta'_{\mathrm{x}}}, \qquad (41)$$

where the apostrophe indicates the corresponding strain and strain rates over time for the flame-spray Al-12Si film, as per Eqs. (34) - (38).

The uniaxial laminate stiffness of the [0°$_8$] and [90°$_8$] coated s-FRPC formulated in Eq. (27) and Eq. (28) were estimated using Eq. (31). The average thickness of the prepared FRPC substrate and the flame-sprayed Al-12Si coating in the coated s-FRPC structure (see Fig. 4.2) was estimated through cross-sectional micrographs. Using the thickness and uniaxial laminate stiffness data, determination of the reduced stiffness constants Q_{11} and Q_{22} was accomplished by solving the system of equations given by Eqs. (27), (28), (39) - (41), using a computational knowledge engine (Wolfram Alpha, Wolfram Research Inc., Champaign, IL, USA) with a solver routine [147, 148]. The solution of the system of equations which included the lowest positive values for Q_{11} and Q_{22} was selected to perform the mechanical characterization of coated s-FRPC specimens.

The resolved Q_{11} and Q_{22} values were used to predict the uniaxial laminate stiffness of [90°$_2$/0°$_2$]$_S$ and [0°$_{10}$] coated s-FRPC specimens using the extensional stiffness components shown in Eq. (26) and Eqs. (39) - (41). The predicted uniaxial laminate stiffness value was compared to the observed uniaxial laminate stiffness of the $[90°_2/0°_2]_S$ and $[0°_{10}]$ coated s-FRPC specimens that was obtained from tensile testing (Eq. (31)) and the relative error was calculated. The relative error between the predicted and observed values for a given coated s-FRPC architecture was calculated as follows:

$$e_\mathrm{r} = \left| \frac{\alpha_\text{predicted} - \alpha_\text{observed}}{\alpha_\text{observed}} \right|, \tag{42}$$

where α_observed is the average uniaxial laminate stiffness obtained from tensile testing and $\alpha_\text{predicted}$ is the predicted uniaxial laminate stiffness value.

4.4 Results and discussion

4.4.1 Thickness measurements and scanning electron microscopy

A flame-sprayed Al-12Si film was randomly selected to perform thickness measurements using an optical microspcope (Ultraphot III, Carl Zeiss, Oberkochen, Baden-Württemberg, Germany) with controlled focal depth [149]. From differential focal depth values, the thickness of free-standing Al-12Si films was estimated to be 0.28 ± 0.02 mm ($n = 10$). The standard error of the mean is included with the sample size (n) used for applicable average values henceforth in this study [110].

A coated s-FRPC specimen of each of the $[0°_8]$, $[90°_2/0°_2]_S$, and $[0°_{10}]$ architectures was randomly selected and cut perpendicularly to the specimen axis to expose the cross section. The width of the cross section was 12 mm. Mounting and polishing of the cross section was performed to a 1 μm finish, in preparation for scanning electron microscopy (SEM) using a specialized instrument (Zeiss EVO MA15, Carl Zeiss, Toronto, ON, Canada). Figure 4.10 shows a SEM image of the cross section of the $[0°_8]$, $[90°_2/0°_2]_S$, and $[0°_{10}]$ coated s-FRPC specimens. Backscattered SEM images were utilized to estimate the average thickness of the Al-12Si coating layer and the prepared FRPC substrate. The thickness of the prepared FRPC substrate was measured as the minimum distance between garnet sand particles on opposite sides of the specimen cross section, as shown in Fig. 4.10. Even though the average thickness of the garnet sand layer can be estimated at about 0.37 mm from SEM images (see Fig. 4.10), it was not considered in the thickness measurement of the prepared FRPC substrate, given the limited stiffness provided by this discontinuous layer. The limited reinforcing effect of the consolidated garnet sand particles can be considered as part of the prepared FRPC specimen stiffness in the CLT model, which is the approach used in this study, given the lower yield strength of the particulate-reinforced epoxy thin film compared to that of the fibre-reinforced epoxy lamina [150, 151].

Table 4.1 shows the average thicknesses of the $[0°_8]$, $[90°_2/0°_2]_S$, and $[0°_{10}]$ coated s-FRPC specimens estimated from SEM images. Based on the observation that the standard error is at least one order of magnitude lower than the average thickness of the $[0°_8]$ and $[90°_2/0°_2]_S$ coated s-FRPC specimens, the average value of $h_{0°} + h_{90°} = 2.7$ mm was selected as the prepared FRPC substrate thickness of the coated s-FRPC specimens exhibiting an eight-lamina architecture ($[0°_8]$, $[90°_8]$, and $[90°_2/0°_2]_S$). Moreover, the prepared FRPC substrate thickness of $[0°_{10}]$ coated s-FRPC specimens can be considered as 3.14 mm. Considering the coated s-FRPC specimen data shown in Table 4.1, the average thickness of the flame-sprayed Al-12Si coating can be estimated to be $h_c = 0.31$ mm. Table 4.2 summarizes the selected constant thickness values used in the laminate stiffness analysis based on the results shown in Table 4.1.

Table 4.1: Average measured thickness of $[0°_8]$, $[90°_2/0°_2]_S$, and $[0°_{10}]$ coated s-FRPC specimens from cross sectional micrographs

Coated s-FRPC specimen	**Average thickness of prepared FRPC substrate (mm)**	**Average thickness of flame-sprayed Al-12Si coating layer (mm)**
$[0°_8]$	2.70 ± 0.04 ($n = 10$)	0.31 ± 0.01 ($n = 20$)
$[90°_2/0°_2]_S$	2.69 ± 0.03 ($n = 10$)	0.30 ± 0.02 ($n = 20$)
$[0°_{10}]$	3.14 ± 0.02 ($n = 10$)	0.32 ± 0.01 ($n = 20$)

Table 4.2: Average constant thickness of flame-sprayed Al-12Si coating (h_c) and the prepared FRPC substrate oriented at θ=0° and θ=90°

Coated s-FRPC specimen	$h_{0°}$ **(mm)**	$h_{90°}$ **(mm)**	h_c **(mm)**
[0°$_8$]	2.7	-	0.31
[90°$_8$]	-	2.7	
[90°$_2$/0°$_2$]$_S$	1.35	1.35	
[0°$_{10}$]	3.14	-	

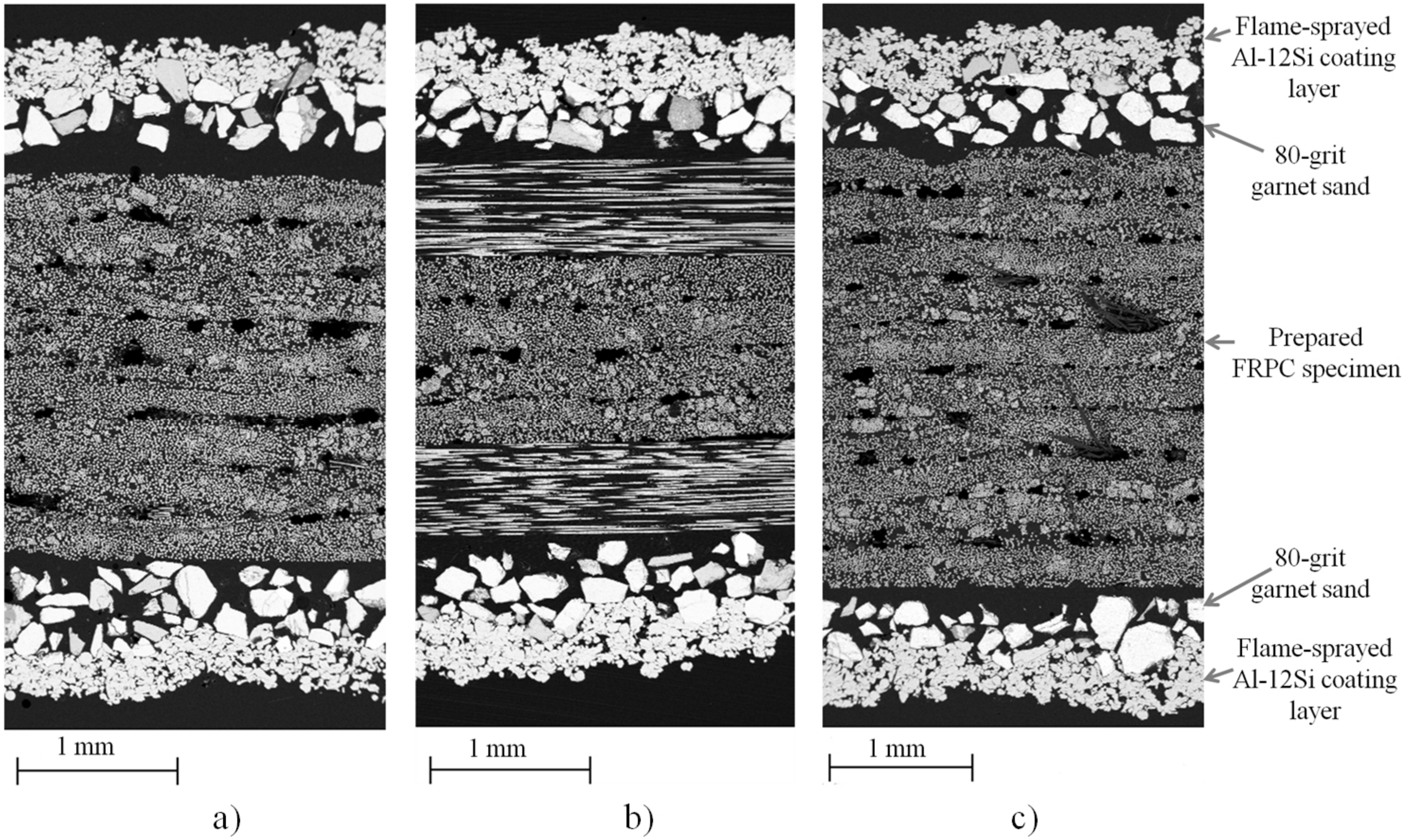

Figure 4.10: Backscattered SEM cross-sectional image of coated s-FRPC of a) [0°$_8$], b) [90°$_2$/0°$_2$]$_S$, and c) [0°$_{10}$] architectures

4.4.2 Laminate stiffness analysis

The fibre volume fraction of the FRPC laminates was calculated to be 41.1% ± 0.3% ($n = 2$) for [0°$_8$], 40.8% ± 0.9% ($n = 2$) for [90°$_8$], 41.5% ± 0.1% ($n = 2$) for [90°$_2$/0°$_2$]$_S$, and 40.1% ± 0.12% ($n = 2$) for [0°$_{10}$] specimens. Even though the number of measured samples ($n = 2$) is low, the estimated average was calculated from nearly identical results, as evidenced by the low standard error of the mean values, which allowed consistent analysis of the stiffness of flame spray exposed and coated s-FRPC specimens based on the fibre architecture. The symmetric laminate structure exhibited by the coated s-FRPC specimens is convenient for tensile testing due to the uncoupling between axial strain deformation and mid-plane curvatures, as evidenced in Eq. (10). The characteristic mechanical behaviour of the specimens in tensile testing is shown in Fig. 4.11. In Fig. 4.11(a) to (e), the characteristic relationship between the distributed laminate load, N_x, and the mid-plane strain in the tensile specimen, ε_x^0, is plotted until the occurrence of structural failure, whereas in Fig. 4.11(f), the tensile response is shown until sliding of the tensile grips occurred, which prevented any further increase in the applied load to the [0°$_{10}$] coated s-FRPC specimens. Based on the tensile response load-strain data shown in Fig. 4.11, the maximum strain values in the linear load-strain range were selected at 0.0035 for flame-sprayed Al-12Si films and 0.003 for [90°$_8$], 0.005 for [90°$_2$/0°$_2$]$_S$, and 0.015 for [0°$_8$] and [0°$_{10}$] flame-sprayed FRPC specimens. During tensile testing, the small difference in the test strain rate applied to the flame-sprayed Al-12Si films

(0.05 mm/min) and FRPC specimens (0.059 mm/min) does not adversely impact the mechanical analysis, since the effect of the increased strain rate on the mechanical behaviour of FRPC laminates in the linear load-strain range is considered to be negligible [152]. Since the axial strain of the flame-sprayed Al-12Si coating is determined by the displacement of the prepared FRPC substrate, the flame-sprayed Al-12Si film tensile data is congruent with the tensile data of coated s-FRPC specimens.

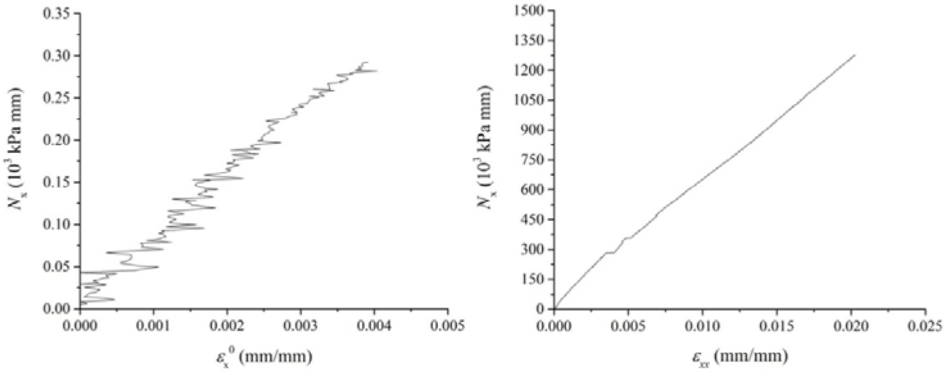

a) Flame-sprayed Al-12Si film

b) Flame spray exposed [0°$_8$] FRPC specimen

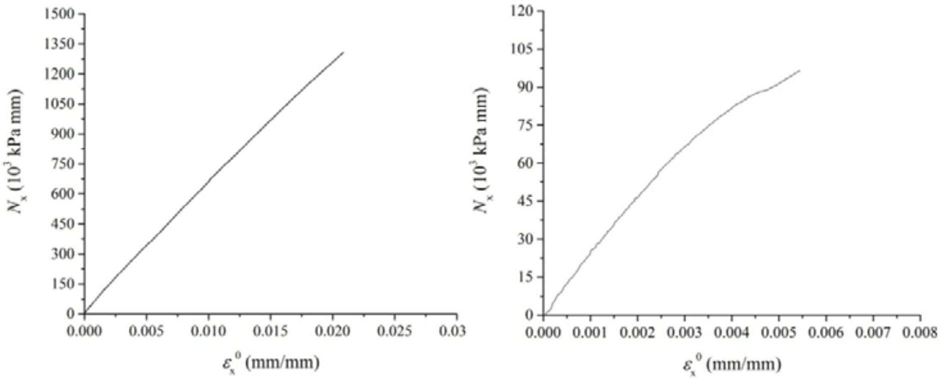

c) [0°$_8$] coated s-FRPC specimen

d) [90°$_8$] coated s-FRPC specimen

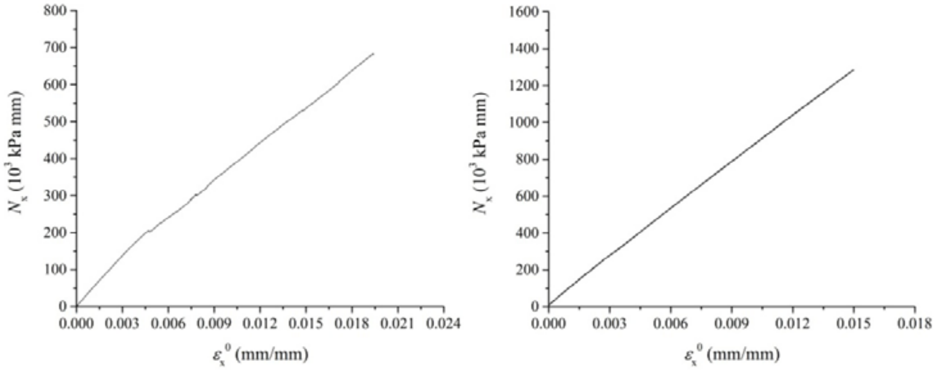

e) [90°$_2$/0°$_2$]$_S$ coated s-FRPC specimen

f) [0°$_{10}$] coated s-FRPC specimen

Figure 4.11: Characteristic mechanical behaviour of tensile specimens: a) Flame-sprayed Al-12Si film b) Flame spray exposed [0°$_8$] FRPC, c) [0°$_8$] coated s-FRPC, d) [90°$_8$] coated s-FRPC, [90°$_2$/0°$_2$]$_S$ coated s-FRPC, and [0°$_{10}$] coated s-FRPC

The application of least squares linear regression to estimate the uniaxial laminate stiffness, α, from tensile data is aimed at minimizing the effect of measurement errors, which is consistent with previous mechanical characterization studies in the elastic load-strain range [153, 154]. The estimated $\underline{\alpha}$ value can be interpreted as the slope parameter of the linear load-strain range in Fig. 4.11, which correlates to the stiffness [10, 119, 135] and the effective Young's modulus of the tensile specimen, as shown in Eq. (33). The coefficient of determination, r^2, indicates the goodness of fit in depicting the observed tensile data using the linear model, on a scale from 0 to 1 [146]. A higher coefficient of determination value corresponds to a better fit between the linear model defined by $\underline{\alpha}$ (Eq. (31)) and the observed tensile data. As shown in Table 4.3, calculated r^2 values for all tensile specimens were equal or higher than 0.96, which allows reliable examination of the linear tensile data based on the least squares linear regression of the $\underline{\alpha}$ value. Moreover, the average $\underline{\alpha}$ value shown in Table 4.3 is used for the mechanical characterization of tensile specimens in the linear load-strain range. This approach is also useful in the analysis of the tensile data of the flame sprayed Al-12Si film (Fig. 4.11 a)), which exhibits a higher variability for the estimation of mechanical properties.

Table 4.3: Estimated uniaxial laminate stiffness ($\underline{\alpha}$) of tensile specimens from tensile data and linear regression through the origin

Tensile specimen	$\underline{\alpha}$ **(GPa·mm)**	r^2	**Average $\underline{\alpha}$ and standard error of the mean (GPa·mm)**
Flame-sprayed Al-12Si film 1	0.75	0.99	0.09 ± 0.02 (*n* = 3)
Flame-sprayed Al-12Si film 2	0.82	0.96	
Flame-sprayed Al-12Si film 3	1.1	0.98	
Flame spray exposed $[0^\circ_8]$ FRPC specimen 1	63.76	0.99	65.87 ± 1.06 (*n* = 3)
Flame spray exposed $[0^\circ_8]$ FRPC specimen 2	67.18	0.99	
Flame spray exposed $[0^\circ_8]$ FRPC specimen 3	66.67	0.99	
$[0^\circ_8]$ coated s-FRPC specimen 1	65.82	0.99	68.47 ± 1.4 (*n* = 3)
$[0^\circ_8]$ coated s-FRPC specimen 2	68.82	0.99	
$[0^\circ_8]$ coated s-FRPC specimen 3	70.78	0.99	

Tensile specimen	$\underline{\alpha}$ **(GPa·mm)**	r^2	**Average** $\underline{\alpha}$ **and standard error of the mean (GPa·mm)**
[$90°_8$] coated s-FRPC specimen 1	22.78	0.99	26.32 ± 1.8 (n = 3)
[$90°_8$] coated s-FRPC specimen 2	28.22	0.99	
[$90°_8$] coated s-FRPC specimen 3	27.97	0.99	
[$90°_2/0°_2]_S$ coated s-FRPC specimen 1	42.12	0.99	44.07 ± 1.2 (n = 3)
[$90°_2/0°_2]_S$ coated s-FRPC specimen 2	44.72	0.99	
[$90°_2/0°_2]_S$ coated s-FRPC specimen 3	45.35	0.99	
[$0°_{10}$] coated s-FRPC specimen 1	84.97	0.99	85.95 ± 0.6 (n = 3)
[$0°_{10}$] coated s-FRPC specimen 2	86.97	0.99	
[$0°_{10}$] coated s-FRPC specimen 3	85.90	0.99	

From Eq. (33), the Young's modulus of the flame sprayed Al-12Si coating was estimated at 0.32 GPa using the average $\underline{\alpha}$ value (Table 4.3) and the average thickness of the flame-sprayed Al-12Si films (0.28 mm). The estimated effective Young's modulus value of the flame sprayed Al-12Si coating (0.32 GPa) is significantly lower than that of bulk Al-12Si (about 80 GPa) [155], which provides evidence of the singular mechanical properties of the porous structure (Fig. 4.10) [156, 157]. It is hypothesized that the low mechanical stiffness of the flame-sprayed Al-12Si coating is due to the low cohesive strength between the flame-sprayed splats and particles, the level of porosity, and crack size in the microstructure [125]. The low cohesive strength of flame-sprayed coatings has been noted in studies based on thermal spraying and thermal-sprayed coatings [26]. The average porosity of the flame-sprayed Al-12Si coating has been estimated to be on the order of 12 - 17% [158], and such high values of coating porosity can significantly reduce the effective Young's modulus value and provide additional initiation points for microstructural cracks. Consequently, the porosity level and morphological features (Fig. 4.10) have a dominant effect on the effective macroscopic axial stiffness of the flame-sprayed Al-12Si coating.

Considering the determination of axial and transversal in-plane strain measurements using the DIC technique, the mechanical deformation of flame-sprayed Al-12Si films and flame spray exposed $[0°_8]$ FRPC specimens over time was obtained, as shown in Fig. 4.12. The use of the DIC technique facilitated the measurement of the transversal strain in flame-sprayed Al-12Si film and flame spray exposed [0°$_8$] FRPC specimens. A DIC image of a flame-sprayed Al-12Si film is shown in Fig. 4.13. The image of the flame-sprayed Al-12Si coating shows a random contrast pattern. As a result, the speckle pattern did not need to be applied to the surface since sufficient surface contrast pattern exists for strain measurements [144]. Based on the axial and transversal strain-time data, maximum time values in the linear load-strain range were selected at $t = 2750$ s for the flame spray exposed [0°$_8$] FRPC specimens and $t = 100$ s for the flame-sprayed Al-12Si films to estimate the major Poisson ratio using Eq. (38) and Eq. (41), respectively. Table 4.4 shows the average axial (β_x) and transversal (β_y) strain rates of flame-sprayed Al-12Si films and flame spray exposed [0°$_8$] FRPC specimens.

Linear regression of the strain rate data of the flame sprayed Al-12Si film (Fig. 4.12 c) and d)) reduced the effect of strain measurement variations over time, which may be attributed to localized changes in the deformation field and the limited resolution of the DIC system (0.01% strain) [140]. As shown in Table 4.4, the Poisson ratio of the flame-sprayed Al-12Si coating (v') is estimated at 0.19 from the average strain rate values. Based on this result, the Poisson ratio of the flame-sprayed Al-12Si coating differs from the value of the isotropic bulk Al-12Si material, equivalent to 0.33 [155], which is consistent with the observation that the mechanical properties of the porous flame-sprayed coatings must be determined independently from the same material in compact form [159].

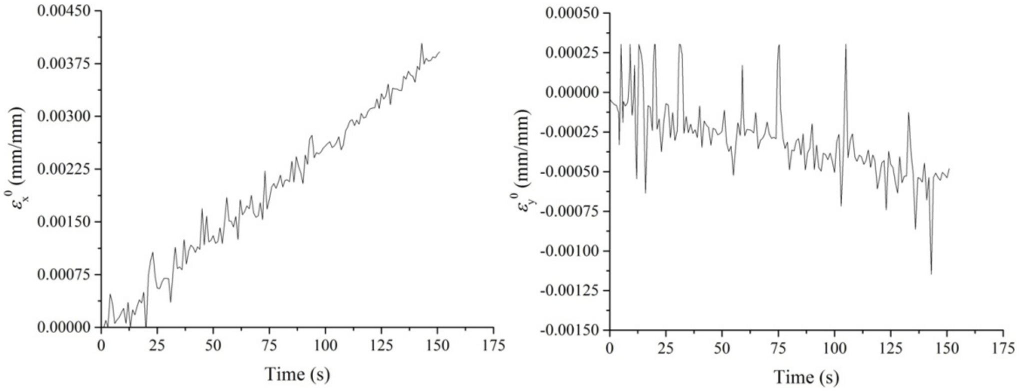

a) Axial strain in flame-sprayed Al-12Si film over time

b) Transversal strain in flame-sprayed Al-12Si film over time

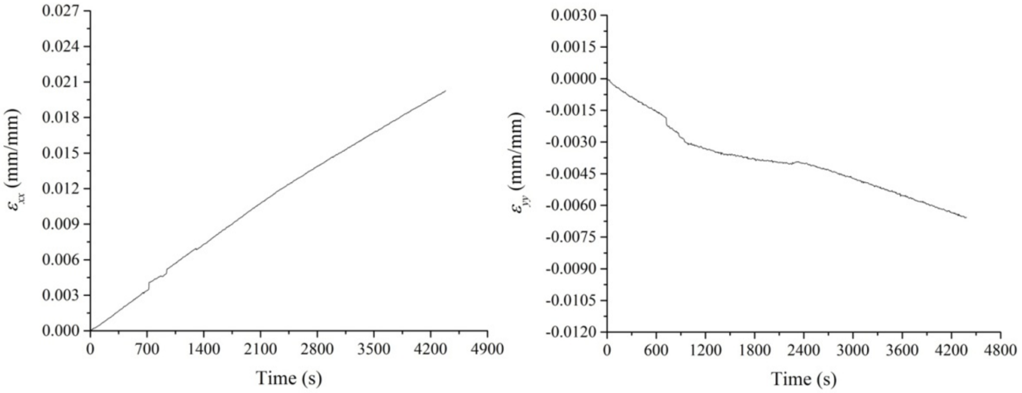

c) Axial strain in flame spray exposed [0°$_8$] FRPC specimen over time

d) Transversal strain in the flame spray exposed [0°$_8$] FRPC specimen over time

Figure 4.12: Characteristic deformation behaviour over time showing: a) axial strain in flame-sprayed Al-12Si film, b) transversal strain in flame-sprayed Al-12Si film, c) axial strain in flame spray exposed [0°$_8$] FRPC specimen, and d) transversal strain in flame spray exposed [0°$_8$] FRPC specimen

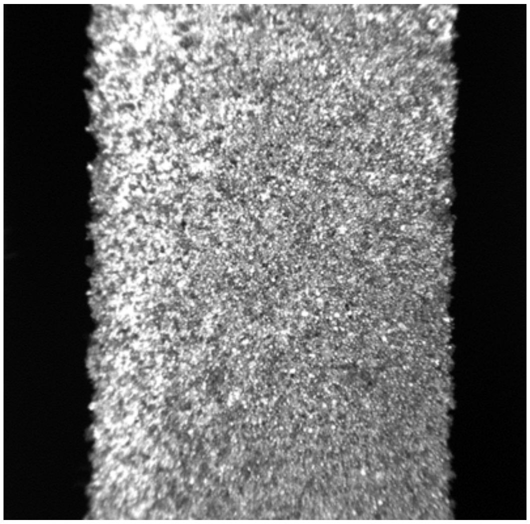

Figure 4.13: Digital image correlation image of a flame-sprayed Al-12Si film for axial and transversal strain measurements

Table 4.4: Average axial (β_x) and transversal (β_y) strain rates of flame-sprayed Al-12Si films and flame spray exposed [0°$_8$] FRPC specimens

Tensile specimen	**β_x (10^{-6}/s)**	**β_y (10^{-6}/s)**	**Estimated Poisson ratio**
Flame-sprayed Al-12Si films	26 ± 3.7 (n = 3)	-4.91 ± 1 (n = 3)	ν=0.19
Flame spray exposed [0°$_8$] FRPC specimens	4.9 ± 0.1 (n = 3)	-1.61 ± 0.1 (n = 3)	ν_{12}=0.33

From Fig. 4.12(c) and (d) and Table 4.4, the average major Poisson ratio of the flame spray exposed [0°$_8$] FRPC specimens (ν_{12}^{e}) was calculated to be 0.33 ± 0.02 ($n = 3$) using Eq. (41) and the strain rate data. Moreover, the value of $\nu_{12} = 0.33$ was selected as the estimate of the major Poisson ratio of the prepared FRPC substrate in coated s-FRPC specimens for the laminate stiffness analysis. Since the flame spray deposition of Al-12Si particles can induce mechanical degradation of the unsprayed FRPC substrate [19, 41, 43], the value of the major Poisson ratio of the flame spray exposed [0°$_8$] FRPC specimen can be considered as a reasonable approximation of the major Poisson ratio of the prepared FRPC substrate in the coated s-FRPC specimens, which is challenging to measure experimentally. However, the fabrication of the flame spray exposed [0°$_8$] FRPC specimens involves an aluminium tape interlayer to prevent material deposition onto the prepared FRPC substrate (Fig. 4.4), which limits the transfer of thermal and kinetic energy from the impinging flame-sprayed Al-12Si particles. Consequently, the major Poisson ratio of the exposed FRPC specimens represents a conservative estimate of the major Poisson ratio of the prepared FRPC substrate post-flame spray deposition (Eq. (39)).

From Table 4.3 data and Eq. (33), the average longitudinal Young's modulus of the flame spray exposed [0°$_8$] FRPC specimen was determined to be 24.44 ± 0.4 GPa ($n = 3$), which is lower than the 32 - 34 GPa value predicted by the rule of mixtures applied to similar E-glass prepreg laminates and prorated for a 40% fibre volume fraction [160, 161]. This discrepancy in values may be explained by the fact that the total thickness measurement of the flame spray exposed [0°$_8$] FRPC specimens includes the thickness of the continuous epoxy adhesive layer between the garnet sand layer and the FRPC laminae (about 0.15 mm in average), as shown in Fig. 4.10. Since the load-bearing FRPC laminae possess a higher stiffness, it follows from Eq. (31) and Eq. (33) that the incremental thickness provided by the lower strength epoxy adhesive will reduce the effective Young's modulus estimate of the prepared FRPC substrate. In addition, it is possible that the heat flux and temperature rise in the heat sensitive epoxy adhesive and subjacent polymer matrix during the flame spray process induced mechanical degradation of the prepared FRPC substrate [43], resulting in a reduction of the effective longitudinal Young's modulus.

The Young's modulus of the flame-sprayed Al-12Si film is related to the uniaxial stiffness, as per Eq. (33). As shown in Table 4.3, the $\underline{\alpha}$ value of the flame-sprayed Al-12Si coating represents less than 4% of the average uniaxial laminate stiffness of coated s-FRPC specimens, which is expected since the prepared FRPC substrate constituted the load-bearing component in the coated s-FRPC structure. However, the lowest standard error of the mean in the coated s-FRPC $\underline{\alpha}$ values (0.6 GPa-mm) is higher than the average uniaxial laminate stiffness of the Al-12Si coating (0.09 GPa-mm). Therefore, the sample-to-sample variation in the uniaxial laminate stiffness of the prepared FRPC substrate restricts the determination of the mechanical properties of flame-sprayed Al-12Si coatings using the inversion problem approach. However, it is conceived that flame sprayed Al-12Si coatings deposited onto polymeric substrates exhibiting lower Young's modulus values, such as elastomers, may allow the determination of the mechanical properties of the coating from the tensile response of the resulting coated structure.

The estimated Young's modulus (0.32 GPa) and the Poisson ratio (0.19) of the flame-sprayed Al-12Si coating can be used to determine its reduced stiffness constant, Q', which is estimated to be 0.332 GPa using Eq. (40). Considering the value of the reduced stiffness constant of the flame-sprayed Al-12Si coating (Q'), the thickness shown in Table 4.2, and the Poisson ratio values in Table 4.4, the following system of equations was solved numerically to obtain the reduced stiffness constants of the flame-sprayed substrate Q_{11} and Q_{22} from $\underline{\alpha}$ values of [0°$_8$] and [90°$_8$] coated s-FRPC specimens (Table 4.3), as per Eqs. (27) and (28):

$$\begin{cases} \alpha_1 = 2(0.332)(0.31) + Q_{11}(2.7) - \dfrac{(2(0.19)(0.332)(0.31) + \nu_{12} Q_{22}(2.7))^2}{2(0.332)(0.31) + Q_{22}(2.7)} = 68.47 \text{ GPa} \cdot \text{mm} \\ \alpha_2 = 2(0.332)(0.31) + Q_{22}(2.7) - \dfrac{(2(0.19)(0.332)(0.31) + \nu_{12} Q_{22}(2.7))^2}{2(0.332)(0.31) + Q_{11}(2.7)} = 26.32 \text{ GPa} \cdot \text{mm} \\ \nu_{12} = 0.33 \end{cases}, \tag{43}$$

which results in $Q_{11} = 26.43$ GPa and $Q_{22} = 10.12$ GPa. Using the values of ν_{12} and Q_{22}, the value of the reduced stiffness constant Q_{12} of the flame-sprayed substrate can be determined at 3.34 GPa, as per Eqs. (21) and (22). In order to compare the previous results to the observed average uniaxial laminate stiffness ($\underline{\alpha}$) of [90°$_2$/0°$_2$]$_S$ and [0°$_{10}$] coated s-FRPC specimens (Table 4.3), the following equation is derived from Eqs. (11), (14) - (22), and (26) for the predicted uniaxial laminate stiffness of the coated $[90°_2/0°_2]_S$ s-FRPC specimen, α_3, as follows:

$$N_x = \left(2Q'h_c + Q_{11}h_{0°} + Q_{22}h_{90°} - \frac{(2\nu' Q' h_c + \nu_{12}Q_{22}(h_{0°} + h_{90°}))^2}{2Q'h_c + Q_{22}h_{0°} + Q_{11}h_{90°}} \right) \varepsilon_x^0 = \alpha_3 \varepsilon_x^0 \; . \qquad (44)$$

Based on the CLT model (Eq. (26)), substitution of the resolved Q_{11} and Q_{22} values, the thickness information (Table 4.2), Q', and Poisson ratio values (Table 4.4) into Eq. (27) and Eq. (44) provides the predicted uniaxial laminate stiffness of $[0°_{10}]$ and $[90°_2/0°_2]_S$ coated s-FRPC specimens, respectively. Table 4.5 shows the predicted uniaxial laminate stiffness of the $[0°_{10}]$ and $[90°_2/0°_2]_S$ coated s-FRPC specimens, $\alpha_{\text{predicted}}$, and the relative error (e_r) of the CLT model prediction with respect to the observed average $\underline{\alpha}$ values (Table 4.3).

Table 4.5: Predicted uniaxial laminate stiffness ($\alpha_{\text{predicted}}$) values of tensile specimens based on the CLT model and relative error (e_r) with respect to observed average values

Tensile specimen	**$\alpha_{\text{predicted}}$ (GPa-mm)**	**e_r with respect to average $\underline{\alpha}$ value**
$[90°_2/0°_2]_S$ coated s-FRPC specimens	47.8	4.53%
$[0°_{10}]$ coated s-FRPC specimens	79.75	7.22%

From Table 4.3 and Table 4.5 results, the CLT model predicts the uniaxial laminate stiffness values of the $[90°_2/0°_2]_S$ coated s-FRPC specimens with higher accuracy, at a relative error of 4.53%. The predicted uniaxial laminate stiffness values of the $[0°_{10}]$ coated s-FRPC specimen exhibited a relative error of 7.22%. It is noted that the relative error in the CLT model predicted values for $[90°_2/0°_2]_S$ and $[0°_{10}]$ coated s-FRPC specimens is lower than the typical 10% error level threshold used in the experimental evaluation of stiffness in fibre-reinforced composites [162]. However, potential enhancements in the CLT model predictions may be achieved by thermo-mechanical modelling of the effect of flame sprayed Al-12Si coating deposition on the mechanical properties (i.e., major Poisson ratio) of the FRPC substrate, which is suggested by the observation that the CLT model slightly overestimated the average uniaxial laminate stiffness of the $[90°_2/0°_2]_S$ coated s-FRPC stiffness, whereas it underestimated that of the higher heat capacity $[0°_{10}]$ coated s-FRPC, as shown in Tables 4.3 and 4.5. On the other hand, the relative error values shown in Table 4.5 suggest that $v_{12}=0.33$ can be a valid estimate of the major Poisson ratio of the flame sprayed FRPC substrate in coated s-FRPC specimen. In order to investigate the effect of the v_{12} value in the laminate stiffness predictions, a sensitivity analysis of the predicted uniaxial laminate stiffness of $[90°_2/0°_2]_S$ and $[0°_{10}]$ coated s-FRPC specimens with respect to changes in the v_{12} estimate (Eq. (43)) was performed. Figure 4.14 a) and b) shows the results of performing the stiffness analysis using v_{12} values between 0.26 and 0.4, which correspond to the reported major and minor Poisson ratios of the load-bearing FRPC laminae (Cycom 1003 E-glass prepreg) [160, 161]. As shown in Fig. 4.14 a) and b), lower values of v_{12} result in a modest reduction of the relative error in the predicted uniaxial laminate stiffness of $[90°_2/0°_2]_S$ coated s-FRPC specimens and no practical change in the relative error estimate for $[0°_{10}]$ coated s-FRPC specimens. It is also noted that the predicted uniaxial laminate stiffness of $[90°_2/0°_2]_S$ coated s-FRPC specimens remains between 47.5 and 48 GPa for all estimates of v_{12}, as shown in Fig. 4.14 a). Therefore, the predicted uniaxial laminate stiffness using the CLT model exhibits low sensitivity to changes in the major Poisson ratio of the flame-sprayed FRPC substrate, which facilitate the determination of the substrate reduced stiffness constants Q_{11} and Q_{22} using v_{12} as the primary experimental estimate. Based on the presented results, it is feasible to describe the effect of the coating and substrate stiffness components in the linear load-strain range of coated s-FRPC structures using the CLT model and the presented experimental methodology, which only requires tensile testing of FRPC laminate architectures in 0° and 90° orientations. Moreover, the CLT model can facilitate the mechanical characterization of general flame spray coated FRPC structures for potential structural applications.

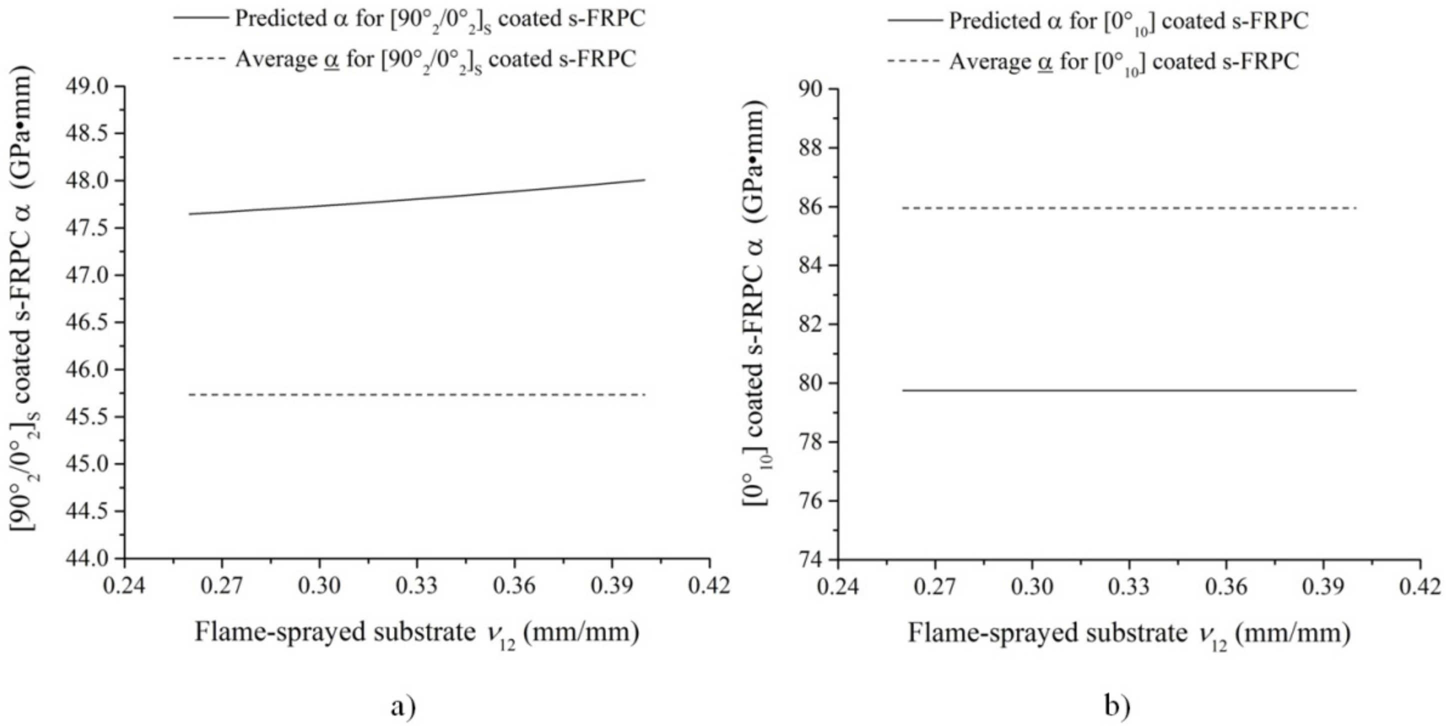

Figure 4.14: Comparison between the observed uniaxial laminate stiffness ($\underline{\alpha}$) and the predicted uniaxial laminate stiffness as function of the ν_{12} estimate for: a) $[90°_2/0°_2]_S$ coated s-FRPC specimens and b) $[0°_{10}]$ coated s-FRPC specimens

4.5 Conclusions

In this study, the elastic behaviour of flame-spray coated FRPC laminates was considered using the CLT model. The development of specific experimental procedures allowed the empirical estimation of the major Poisson ratio of flame spray exposed FRPC specimens and the mechanical properties of the flame sprayed Al-12Si coating characterized as an isotropic lamina. The mechanical properties of the flame sprayed Al-12Si coating lamina were assessed from flame-sprayed film tensile data. The Young's modulus and the Poisson ratio of the flame sprayed coating were estimated at 0.32 GPa and 0.19, respectively.

The tensile data of coated $[0°_8]$ and $[90°_8]$ FRPC specimens was used in tandem with the empirical property values to provide a complete description of the stiffness of the FRPC substrate post-flame spray deposition. Considering the mechanical characterization of the flame-sprayed Al-12Si coating and the flame-sprayed FRPC substrate, the CLT model and presented experimental procedure can be used to predict the uniaxial stiffness of general flame-spray coated and symmetric FRPC structures. Reasonable agreement was observed between average measurements and predicted uniaxial stiffness of coated $[0°_{10}]$ and $[90°_2/0°_2]_S$ FRPC specimens based on the CLT model. The relative errors of the CLT model predictions were determined at 7.22% for coated $[0°_{10}]$ FRPC specimens and 4.53% for $[90°_2/0°_2]_S$ FRPC specimens. Potential enhancements in the CLT model predictions may be achieved by incorporating thermo-mechanical effects of flame sprayed Al-12Si coating deposition on the mechanical properties of the FRPC substrate.

The application of the presented experimental approach and the CLT model may allow the determination of the elastic behaviour of general flame spray coated FRPC specimens with symmetric fibre architecture using tensile test data from flame-sprayed films and 0° and 90° laminate architectures, which can facilitate the structural design and testing for potential applications.

Chapter 5 Damage detection framework for fibre-reinforced polymer composites using flame sprayed Al-12Si coatings*[158]

5.1 Introduction

Fibre reinforced polymer composite (FRPC) materials can provide high specific stiffness and strength to engineering structures. However, damage detection in FRPC structure using electrical signals is considered complex due to the material inhomogeneity and anisotropy exhibited by the fibre-matrix ensemble. Considering that the development of electrically conductive FRPC constitutes a topic of active research [15, 163], previous studies have investigated the feasibility of depositing metal coatings onto FRPC structures [19, 41]. Moreover, the fabrication of electrically conductive thermal-sprayed metal

---

* A version of this chapter was published in the Proceedings of the Canadian International Conference on Composite Materials (CANCOM) 2015, August 17-20th, 2015, Edmonton, Alberta, Canada.

coatings onto polymers as a fabrication technique for electrical sensors [53, 68, 83, 84] is of interest.

The deposition of an electrically conductive layer may be considered as a novel approach for damage detection in the FRPC structure, provided that strain in the FRPC substrate affects the conduction of electrical charges through the conductive metal coating. Moreover, strain-induced damage in both the conductive coating and the substrate of the coated FRPC structure may be assessed by this method [100, 101]. An electrically conductive metal coating may be deposited onto the FRPC substrates using a thermal spray process [17, 19, 26, 83]. Thermal spraying comprises a group of coating processes whereby a heat source is used to melt and accelerate powdered particles prior to their deposition onto the substrate.

Conduction of electrical charges through thermal-sprayed coatings has been proposed for structural health monitoring sensors in FRPC structures, using cross-property relationships between the mechanical condition of the substrate and the electrical resistance of the coating [19, 83]. However, several studies [19, 83, 121] have indicated that the porous structure of thermal-sprayed metal coatings result in electrical properties which differ from that of the bulk metal, and therefore require special characterization as an electrical conductor. In a previous study, Huonnic *et al.* [19] deposited flame-sprayed aluminium coatings onto cured glass and basalt FRPC tubes and measured the electrical resistance and resistivity of the metal layer to characterize the quality of the deposits. A minimum of two flame spray torch passes was required to produce a uniform and electrically continuous metal layer on the polymer-based tubes and no evidence of phase changes or oxidation was observed in the flame-sprayed coatings.

In this chapter, the deposition of a thin layer of aluminium-12silicon (Al-12Si) onto FRPC samples was performed using flame spraying, a lower temperature and lower cost thermal spraying process [26], in which the combustion of gases fuels a flame that melts and accelerates droplets for layered coating deposition. The objectives of this work were to: (1) provide a theoretical framework to describe the relationship between strain in cross-ply FRPC samples and the electrical resistance change in the flame-sprayed Al-12Si coating and (2) evaluate the potential to perform damage detection in FRPC composites by monitoring the change in electrical resistance of flame-sprayed Al-12Si coatings.

5.2 Mathematical model description

Flame-sprayed Al-12Si coatings deposited onto uniaxial FRPC laminate structures may be envisaged as an isotropic and electrically conductive lamina of thickness, h_c, width, b, and length, l. A macroscopic description of the electrical conduction in the Al-12Si coating based on free electrons can be considered if the coating dimensions are at least two orders of magnitude higher than the electron mean free path [164], which has been reported as 1 μm or less for metals [165]. Moreover, a macroscopic approach of to damage detection may be used to describe the electrical properties of conductive flame-sprayed of thickness greater than 100 μm [19].

The porous structure of the flame-sprayed Al-12Si coating reduces the size of the nominal cross sectional area $A_n = b \cdot h_c$ that is available for conduction of electrical charges, and increases the volume electrical resistivity of the medium, ρ, with respect to bulk Al-12Si values. If the flame-sprayed Al-12Si coating exhibits ohmic behaviour [166] and a uniform electrical field is applied, the electrical resistance of the flame-sprayed Al-12Si coating, R, can be expressed as a function of the coating length, l, effective electrical resistivity, ρ_{eff}, and effective cross-sectional area, A_{eff}, under standard conditions [167] of temperature (20 to 30°C) and pressure (1 atm) [19]:

$$R = \rho_{\text{eff}} \frac{l}{A_{\text{eff}}} . \tag{45}$$

The effective cross sectional area is defined as $A_{\text{eff}} = A_n (1-P)$, where P denotes the porosity in the Al-12Si coating. Considering the strained configuration of the coated FRPC shown in Fig. 5.1, it can be shown from Eq. (45) and by using chain rule differentiation that the change in electrical resistance of the flame-sprayed Al-12Si coating due to the application of uniaxial strain, ε_x, is given by:

$$\frac{dR}{d\varepsilon_x} = \frac{\partial R}{\partial l}\frac{dl}{d\varepsilon_x} + \frac{\partial R}{\partial A_{\text{eff}}}\left[\frac{\partial A_{\text{eff}}}{\partial A_n}\frac{dA_n}{d\varepsilon_x} + \frac{\partial A_{\text{eff}}}{\partial P}\frac{dP}{d\varepsilon_x}\right] + \frac{\partial R}{\partial \rho_{\text{eff}}}\frac{d\rho_{\text{eff}}}{dP}\frac{dP}{d\varepsilon_x} . \tag{46}$$

Noting that $\frac{dl}{d\varepsilon_{\mathrm{x}}} = l$ and $\frac{dA_{\mathrm{n}}}{d\varepsilon_{\mathrm{x}}} = -2\nu A_{\mathrm{n}}$, where ν is the Poisson's ratio of transverse to axial strain in the structure, the following relation is obtained for the relative resistance change in the porous Al-12Si coating:

$$\frac{dR}{R} = \left(1 + 2\nu + \left(\frac{1}{1-P}\frac{dP}{d\varepsilon_{\mathrm{x}}}\right) + \frac{1}{\rho_{\mathrm{eff}}}\frac{d\rho_{\mathrm{eff}}}{dP}\frac{dP}{d\varepsilon_{\mathrm{x}}}\right)d\varepsilon_{\mathrm{x}}, \tag{47}$$

which measures the fraction of electrical resistance change with respect to the original resistance value (or size) of the conductor. Assuming that the Al-12Si coating is oxide-free and behaves like a powder compact, then due to the relatively high porosity exhibited in flame-sprayed coatings, the relationship between the effective electrical resistivity and porosity can be expressed by using a model proposed by Montes, *et al.* [168]:

$$\rho_{\mathrm{eff}} = \rho_0(1-P)^{-\beta}, \tag{48}$$

where the exponent, $\beta > 0$, is a constant that depends on the electrical properties of the Al-12Si coating. The assumption of oxide-free flame-sprayed Al-12Si coatings has been justified by other investigators using aluminium coatings [19]. On the other hand, the relationship between porosity and deformation in the flame-sprayed Al-12Si coating can be represented using the model developed by Carroll [169-171] as applied to a linear elastic porous solid under uniaxial strain:

$$P = 1-(1-P_0)e^{-c\varepsilon_{\mathrm{x}}}, \tag{49}$$

where P_0 is the porosity of the unstrained flame-sprayed Al-12Si coating and $c > 0$ is an empirical constant that describes the porosity change rate with respect to strain, with higher values of c corresponding to greater porosity per unit of strain. In circumstances where the Poisson ratio (v) of the structure is independent of ε_x, substitution of Eqs. (48) and (49) into Eq. (47) yields a first-order and separable differential equation that can be solved by direct integration. By applying the Dirichlet boundary condition $R(0) = R_0$ for the unstrained flame-sprayed Al-12Si coating, the following analytical solution is obtained:

$$R = R_0 e^{(1+2v+c+\beta c)\varepsilon_x} = R_0 e^{a\varepsilon_x}, \tag{50}$$

where $a = 1 + 2v + c + \beta c$ is a constant. Since the Poisson's ratio of an isotropic material cannot be less than -1 or greater than 0.5 [172], it follows from Eq. (50) that $a > -1$ and piezoresistive effects in the flame-sprayed Al-12Si coating correlate to higher values of a. The piezoresistive effect denotes the change in the effective electrical resistivity of the material at macro scales due to applied mechanical strain. The relative change in electrical resistance of the flame-sprayed Al-12Si coating under strain is given by:

$$\delta = \frac{\Delta R}{R_0} = \frac{R - R_0}{R_0} = e^{(1+2v+c+\beta c)\varepsilon_x} - 1 = e^{a\varepsilon_x} - 1. \tag{51}$$

Therefore, a descriptive model of the change in electrical resistance of flame-sprayed Al-12Si coating as a function of the applied axial strain is provided by Eq. (51), which may be correlated to damage mechanisms in similarly-coated FRPC structures of l, b, and h_c dimensions.

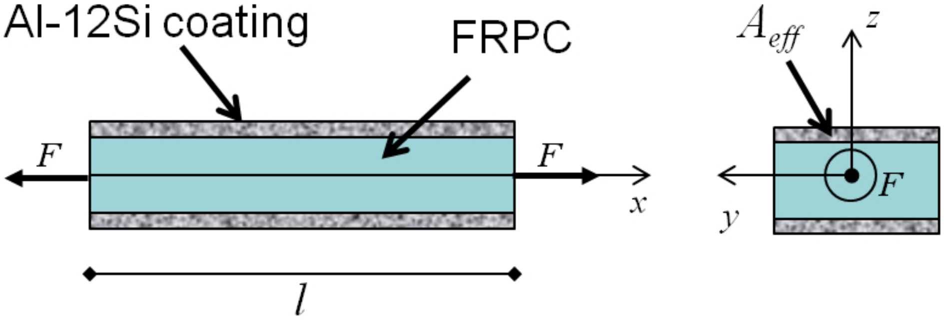

Figure 5.1: Schematic of a symmetrically flame spray coated FRPC composite under applied axial strain

5.3 Experimental method

5.3.1 Fabrication of composite material structures

Fiber-reinforced polymer composite laminates exhibiting [0°$_8$], [90°$_2$/0°$_2$]$_S$, and [0°$_2$/90°$_2$]$_S$ fibre architectures were fabricated using manual lay-up of unidirectional E-glass prepreg plies (Cycom 1003, Cytec Engineered Materials, Woodland Park, NJ, USA). Polymer matrix curing was performed in an oven at 166 °C for one hour. After curing, three rectangular specimens were cut to size from [0°$_8$] and [90°$_2$/0°$_2$]$_S$ laminates, whereas two rectangular specimens were cut from the [0°$_2$/90°$_2$]$_S$ laminate, in accordance with ASTM Standard D3039 [141]. The dimensions of the rectangular composite specimen were 254 mm in length and 25.4 mm in width. The free gauge length was set at 50.8 mm in the midsection of the composite specimen. The fibre volume fraction of the cured prepregs was obtained using the weight of one 25.4 mm x 25.4 mm laminate sample before and after burnout of the matrix phase inside an oven at 540 °C for 4 hours. The fibre volume fraction V_f of each laminate was calculated using the following formula:

$$V_\mathrm{f} = \frac{\dfrac{m_\mathrm{f}}{\rho_\mathrm{f}}}{\dfrac{m_\mathrm{f}}{\rho_\mathrm{f}} + \dfrac{m_\mathrm{m}}{\rho_\mathrm{m}}}, \qquad (52)$$

where m_f and m_m are the masses, and ρ_f and ρ_m are the densities of the fibre and matrix, respectively.

A high-strength epoxy adhesive (Scotch-Weld DP460 Off-White, 3M, St. Paul, MN, USA) was used to incorporate tensile grip connections and consolidate a layer of sprinkled 80-grit (~165 μm) garnet sand to the side of the composite specimen, as shown in Fig. 5.2. Garnet sand layer was used as an inexpensive roughening agent to promote adhesion of the spray-deposited Al-12Si particles [41, 102]. An aluminium tape section (438, 3M, St. Paul, MN, USA) was bonded onto the garnet-sand-roughened surface of the specimen at the end of the gauge length section using the high-strength epoxy adhesive. The two aluminium tape sections, herein called 'aluminium tabs', constituted electrically conductive terminal points attached to the surface of the specimen during mechanical tests. Additional garnet sand was incorporated on the edges of the aluminium tabs to create a gradual transition between the aluminium tape and the adjacent garnet-sand-roughened surface. Careful grit-blasting of the bonded aluminium tabs was executed with #24 alumina grit particles (Manus Abrasive Systems, Inc., Edmonton, AB, Canada) to promote flame spray deposition of Al-12Si particles. All preparation steps were performed on the two opposite sides of the composite specimen. An example of a prepared composite specimen is shown in Fig. 5.2. A tape mask (170-10S Red, Green Belting Industries, Mississauga, ON, Canada) was used to protect the prepared composite specimen during grit blasting and successive flame spray coating deposition.

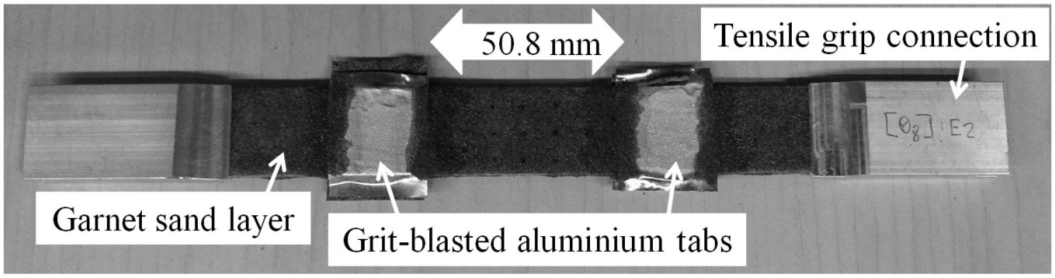

Figure 5.2: Composite specimen prior to flame spray deposition of the Al-12Si coating

5.3.2 Flame spray deposition of the Al-12Si coating

The composite specimen was fixed to a support plate at room temperature, as shown in Fig. 5.3. A gas atomized aluminium-12silicon (Al-12Si) powder, consisting of aluminium, alloyed with 12 wt.% silicon (52C-NS, Oerlikon Metco, Winterthur, Zürich, Switzerland), was deposited onto the prepared composite specimens. The morphology of the Al-12Si powder consisted of spheroidal particles ranging from 45 μm to 90 μm in diameter.

An oxy-acetylene flame spray torch (6P II, Oerlikon Metco, Winterthur, Zürich, Switzerland) was attached to a Motoman robot arm (HP20, Yaskawa Electric Corporation, Fukuoka, Japan) and employed for flame spray deposition onto the fixed composite specimens. A combustion flame was generated from the flame spray torch using a gas mixture of 8 NLPM (normal liters per minute) of acetylene and 25 NLPM of oxygen. Injection of the Al-12Si particles into the flame spray torch was performed using a volumetric powder feed unit (5MPE, Oerlikon Metco, Winterthur, Zürich, Switzerland) and argon as the carrier gas at a pressure of 515 kPa (60 psig) and 0.4 m^3/h (15 standard cubic feet per hour). The powder feed unit supplied the Al-12Si particles at a normalized powder feed rate of 90 on the flow meter reading gauge. The flame spray torch travelled linearly and parallel to the length of the specimen at a stand-off distance of 150 mm from the composite substrate, and performed horizontal deposition passes at 500 mm/s, with vertical steps of 7 mm between each pass. Three layers were deposited with a 5-minute cooling period between consecutive layer fabrications. Flame spray deposition of Al-12Si coatings was performed on the two opposite sides of the composite specimen to create a symmetrically coated laminate for tensile tests.

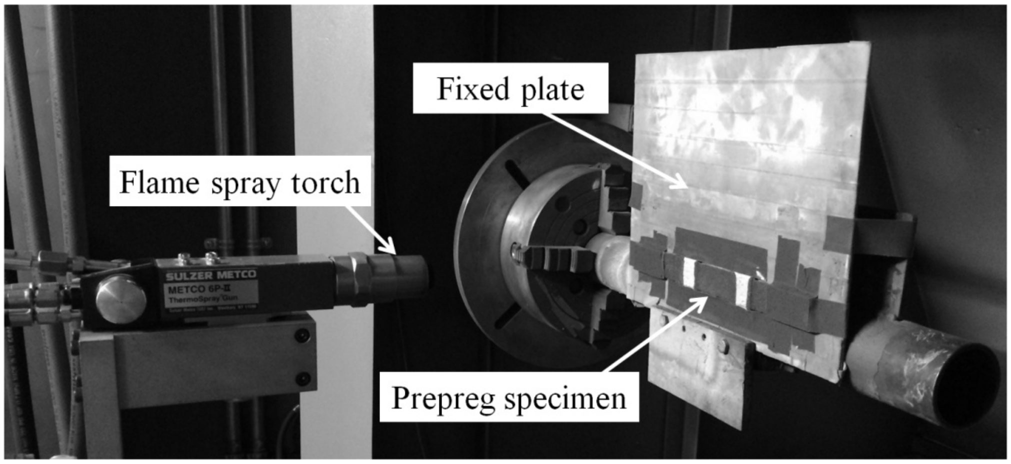

Figure 5.3: Experimental assembly for Al-12Si flame spray deposition onto composite specimens

5.3.3 Tensile testing and electrical measurements

Tensile tests were performed on two coated specimens of $[0°_8]$, $[90°_2/0°_2]_S$, and $[0°_2/90°_2]_S$ laminate fibre architectures. Flame-sprayed Al-12Si coatings deposited onto FRPC specimens were inspected using a multimeter (8846A, Fluke, Everett, WA, USA) and electrical conduction between the aluminium tabs was confirmed. No electrical connexion between the tensile grip connections was observed using direct multimeter measurements. Prior to the application of tensile loads, copper wires were soldered onto the aluminium tabs and connected to a Wheatstone bridge circuit with a set-to-length constantan wire resistance, R_C, as shown in Fig. 5.4. An attempt was made to balance the Wheatstone bridge using the adjustable resistance, until the voltage across the bridge (V_g) was measured below a threshold of 5 mV. The power supply voltage

(V_S) applied to the Wheatstone bridge did not exceed 275 mV and was constrained by a constant direct current I_S of 1 A to limit the effect of temperature on the electrical measurements (i.e. Joule heating). The Wheatstone bridge allowed the measurement of small changes in the electrical resistance (R) of the Al-12Si coating deposited onto the specimen gauge length section during the tensile tests. A 12.7mm gauge length extensometer (634.31, MTS Systems Corporation, Eden Prairie, MN, USA) was installed on the composite specimen thin edge for strain measurements in the FRPC substrate, whereas a 25.4 mm gauge length extensometer (634.12, MTS Systems Corporation, Eden Prairie, MN, USA) was used for strain measurements in the flame-sprayed Al-12Si coating.

A 100-kN capacity uniaxial testing equipment (810, MTS Systems Corporation, Eden Prairie, MN, USA) was used to apply tensile load and induce damage in the FRPC specimen while the Wheatstone bridge was connected to the aluminium tabs. Monotonic loading was performed at a stroke rate of 0.978 µm/s (0.05868 mm/min). The true strain in the FRPC substrate (ε), the true strain in the Al-12Si coating (ε_x), the applied load (F), the voltage across the bridge (V_g), and the voltage across the aluminium tabs (V_x) were recorded at a frequency of 2 Hz and at room temperature. Based on the Wheatstone bridge circuit configuration shown in Fig. 5.4, the electrical resistance change of the Al-12Si coating deposited onto the specimen gauge length section (between the aluminium tabs) can be estimated as:

$$\left(\frac{\Delta R}{R_0}\right)_i = \frac{R_i - R_0}{R_0} = \frac{\dfrac{(V_\mathrm{x})_i}{\left(I_\mathrm{s} - \dfrac{((V_\mathrm{g})_i - (V_\mathrm{x})_i)}{10\,\Omega}\right)} - R_0}{R_0}, \tag{53}$$

where the index, *i* denotes the values of the *i*-th data point recorded during the tensile test. Tensile tests were performed until structural failure of the coated composite specimen occurred. Statistical analysis of the tensile test data was executed using the Origin 2015 software (OriginLab Corporation, Northampton, MA, USA).

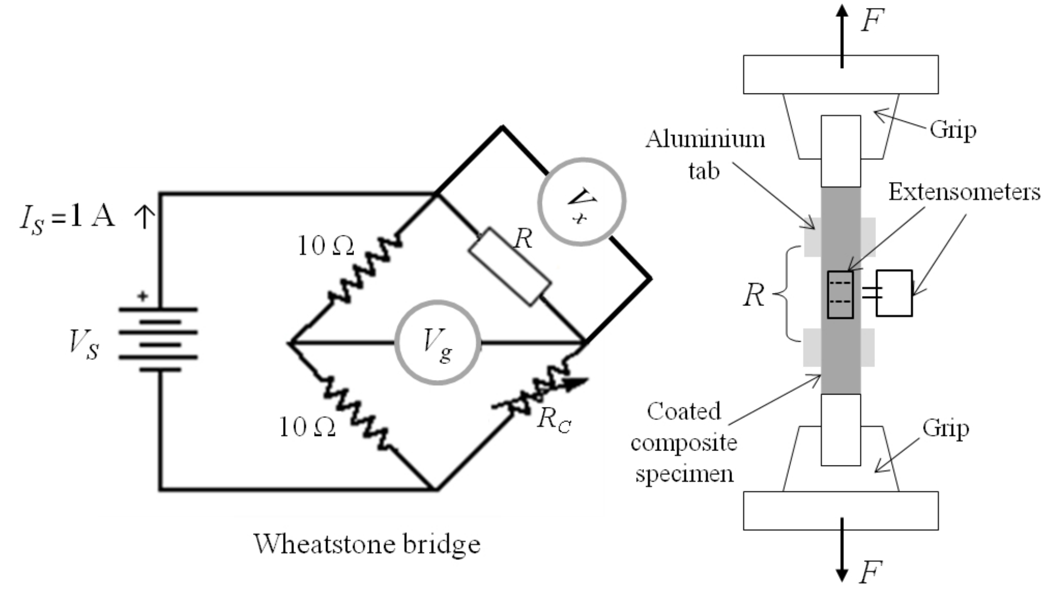

Figure 5.4: Schematic of the tensile test apparatus and Wheatstone bridge circuit, including the Al-12Si coating resistance, *R*

5.4 Results and discussion

Damage detection in FRPC specimens was examined using the strain level and structural damage considerations in unidirectional and cross-ply laminates. Tensile testing of cross-ply composites induces matrix and fibre damage in the laminate structure, which allows for a structural analysis extensible to more complex FRPC laminates [83, 173, 174]. On the other hand, unidirectional composites can be optimized for axial loading by aligning the fibres to the direction of the strain. Testing of the $[0°_8]$ fibre architecture allows the evaluation of the coating behaviour at a higher strain level and fibre-dominated damage. Also, symmetrically coated laminates constitute a convenient structure for tensile testing, due to the uncoupling between axial strain deformation and mid-plane curvatures [119, 175].

5.4.1 Characterization of coating material

Material characterization was performed to evaluate the constituents and morphological features of the deposited particles, which may affect the electrical properties and mechanical behaviour of the Al-12Si coating (e.g., coating porosity and average thickness). One $[0°_8]$ and one $[90°_2/0°_2]_S$ coated FRPC specimen were randomly selected and cut perpendicularly to the specimen axis to expose the cross section. A 12-mm wide cross section was mounted and polished to a 1-µm finish, in preparation for scanning electron microscopy (SEM) using a high definition instrument (Zeiss EVO MA15, Carl Zeiss, Toronto, ON, Canada).

Figure 5.5 shows the SEM image of the cross section of the coated specimens with porosity (*P*) values of the top and bottom Al-12Si coating layers. Moreover, Fig. 5.6 shows a SEM image and the energy-dispersive X-ray spectroscopy (EDS) mapping used to evaluate the presence of metallic compounds in the Al-12Si coatings, revealing that no chemical reaction or phase change (i.e., oxidation) occurred in the Al-12Si coating material as a result of the flame spray process.

A relatively uniform Al-12Si coating coverage of the substrate was observed with an average thickness of 0.29 ± 0.01 mm ($n = 4$). The standard error of the mean is included with the sample size (n) used for all average values henceforth in this study [110]. Porosity estimates of the flame-sprayed Al-12Si coating layer ranged from 12% to 17%, as shown in Fig. 5.5. The overall average layer porosity for flame-sprayed Al-12Si coatings was calculated at 0.15 ± 1 ($n = 4$) from SEM micrographs. However, the lamellar microstructure of fully and partially molten particles in the flame-sprayed Al-12Si coating allows for significant variation in local porosity levels and morphology, as evidenced in the relative large value of the standard error of the mean. The porosity level of the flame sprayed Al-12Si coating can affect its mechanical and electrical properties by limiting the adhesion and cohesion of coating particles [26].

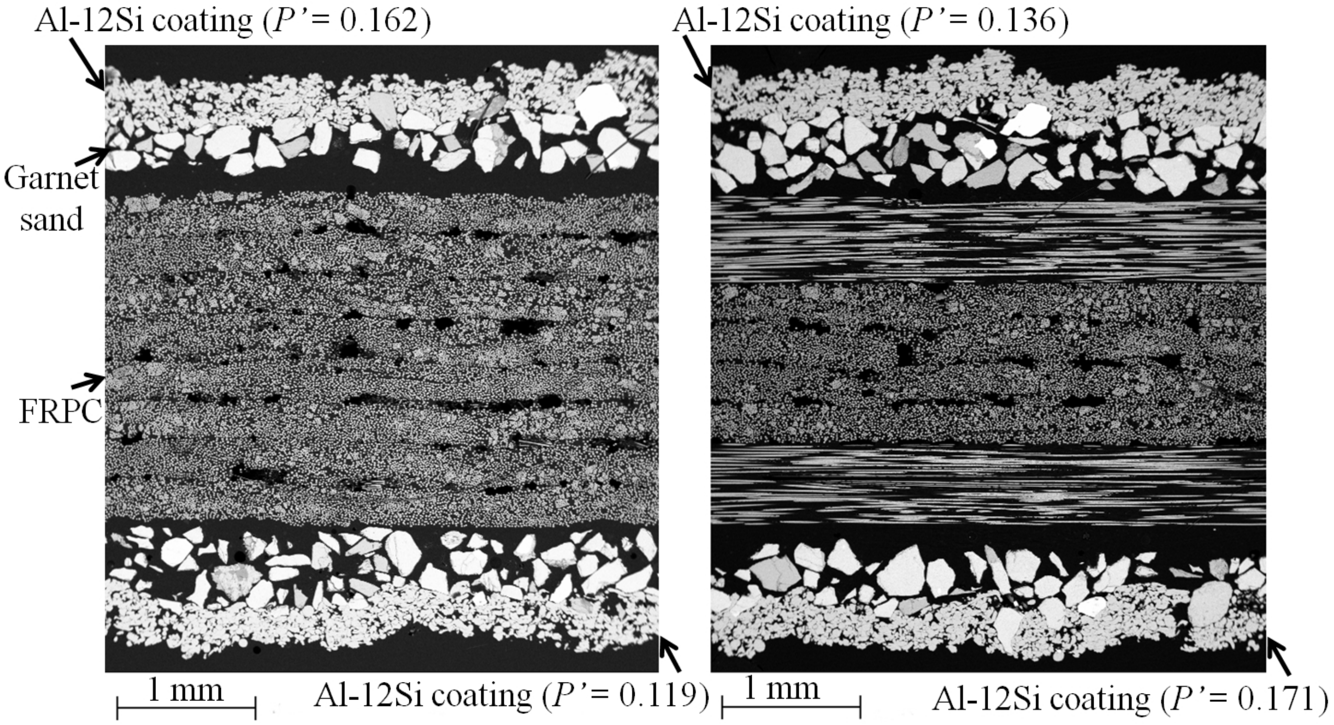

a) $[0°_8]$ b) $[90°_2/0°_2]_S$

Figure 5.5: Backscattered SEM image of the cross section of coated composite specimens with fibre architectures of a) $[0°_8]$ and b) $[90°_2/0°_2]_S$, showing the estimated porosity level (P') in the flame-sprayed Al-12Si coating

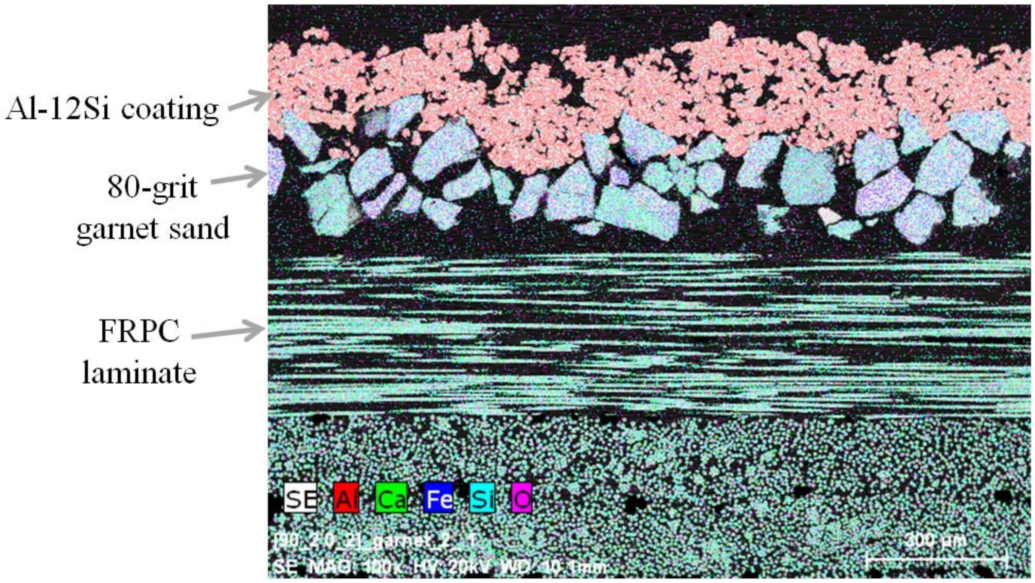

Figure 5.6: Backscattered SEM cross-sectional image with energy-dispersive X-ray spectroscopy (EDS) mapping of flame sprayed Al-12Si coating showing the content of oxygen (O) in purple

5.4.2 Damage detection in the FRPC using Al-12Si coating electrical resistance change

The electrical resistance of the Al-12Si coating was affected by the deformation of the composite specimen, which induced damage in the coated FRPC structure. The strain in the prepreg substrate produced negligible differences (< 1 mε) with respect to the strain measured in the thin flame-sprayed Al-12Si coating. The average value of the initial electrical resistance (R_0) of the

Al-12Si coatings deposited onto the specimen gauge length section was estimated at 177 ± 9 mΩ ($n = 6$). Direct proportionality between the direct electrical current and voltage in the Al-12Si coating (Ohmic behaviour) was observed for all coated specimens. Figure 5.7(a) shows the characteristic relationship between the voltage and direct electrical current of coated FRPC specimens in the unstrained configuration. An example of the current-voltage characteristic relationship in flame-sprayed Al-12Si coatings under axial deformation is shown in Fig. 5.7(b), which indicates that the coatings remained Ohmic even under axial loading.

The tensile strength of the specimen was measured using the laminate distributed load, which is defined as the applied axial load F divided by the width of the coated composite specimen b, in accordance to the Classical Laminate Theory [119]. The ultimate laminate distributed load of cross-ply specimens averaged 627 ± 9 N/mm, while that of the $[0°_8]$ specimens was 1036 ± 14 N/mm. Also, the fibre volume fraction of the FRPC specimens was calculated at 41.6% for of $[0°_8]$, 41.1% for $[90°_2/0°_2]_S$, and 41.4% for $[0°_2/90°_2]_S$, which allowed consistent analysis of tensile data.

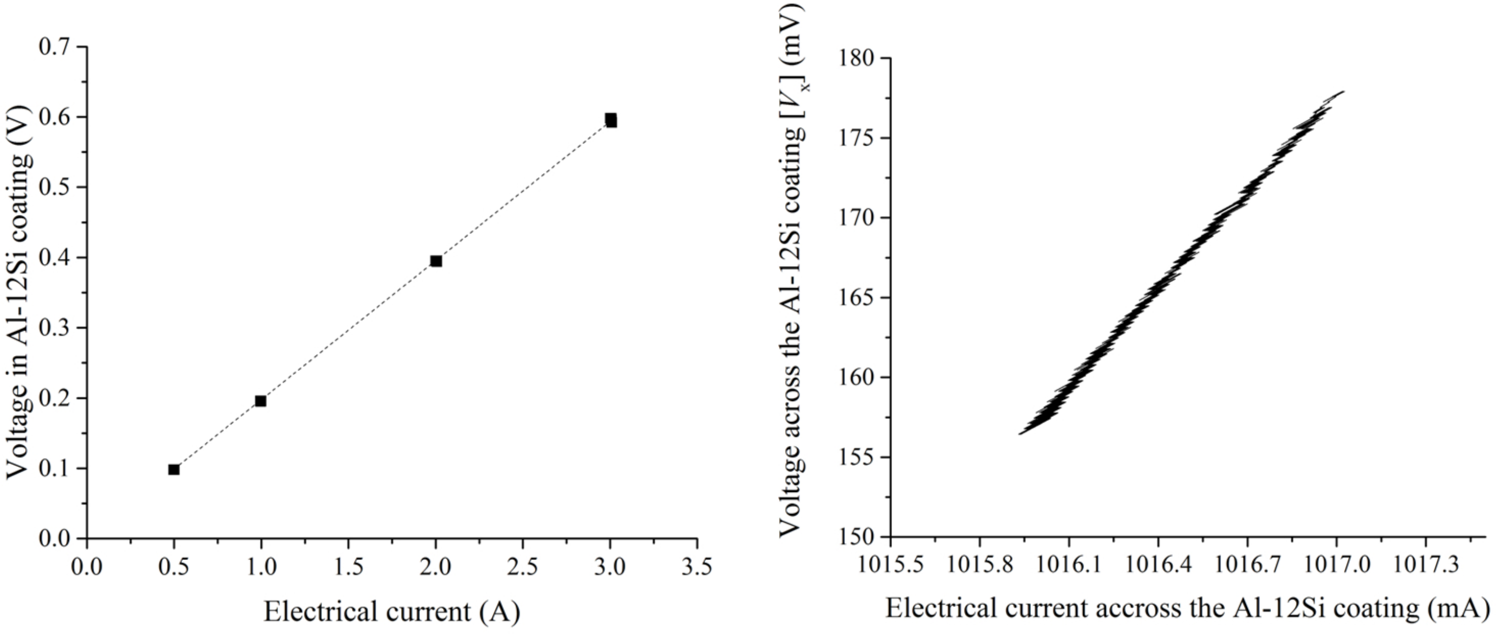

a)

b)

Figure 5.7: Characteristic voltage current relationship in flame sprayed Al-12Si coatings in: a) unstrained configuration and b) under axial deformation

Using tensile test data, least squares curve fitting was performed to optimize the parameter *a* in the *δ* function of Eq. (51), using the Levenberg-Marquardt algorithm [176, 177] and the set of *m* empirical datum pairs $\left((\varepsilon_{\mathrm{x}})_i , \left(\frac{\Delta R}{R_0} \right)_i \right)$ from Eq. (53). The objective of the optimization was set to find the value of *a* in the *δ* function that minimizes the sum of the squares of the deviations, *S*(*a*), from the experimental results. The expression for the sum of the squares of the deviations is:

$$S(a) = \sum_{i=1}^{m} \left[\left(\frac{\Delta R}{R_0} \right)_i - \delta(\, (\varepsilon_{\mathrm{x}})_i \, , a \,) \right]^2 . \tag{54}$$

The implementation of the Levenberg–Marquardt algorithm was conditioned to a convergence tolerance of $1\mathrm{x}10^{-9}$, initial iteration value of 1 for *a*, and a maximum of 5000 iterations for fit control. The adjusted statistical coefficient of determination, $\underline{R}^2$, was calculated for each parameter-optimized *δ* function and tensile data set using the following expression [146]:

$$\underline{R}^2 = 1 - \frac{(m-1)}{m} \left(1 - \left(\frac{ m \sum_{i=1}^{m} (\varepsilon_{\mathrm{x}})_i \left(\frac{\Delta R}{R_0} \right)_i - \left(\sum_{i=1}^{m} (\varepsilon_{\mathrm{x}})_i \right) \left(\sum_{i=1}^{m} \left(\frac{\Delta R}{R_0} \right)_i \right) }{ \sqrt{ m \sum_{i=1}^{m} (\varepsilon_{\mathrm{x}})^2{}_i - \left(\sum_{i=1}^{m} (\varepsilon_{\mathrm{x}})_i \right)^2 } \cdot \sqrt{ m \sum_{i=1}^{m} (\frac{\Delta R}{R_0})^2{}_i - \left(\sum_{i=1}^{m} (\frac{\Delta R}{R_0})_i \right)^2 } } \right)^2 \right) . \tag{55}$$

The statistical analysis of the experimental data allowed the selection of optimal values for the parameter *a* in the model description given by Eq. (51), and statistical evaluation of the goodness-of-fit between the tensile data and the proposed analytical description of the relative electrical resistance change in the flame-sprayed Al-12Si coating. The proposed model for the relative change in electrical change δ in Eq. (51) may be considered an extension of the bulk conductor model [178, 179] to include porosity effects and piezoresistivity. Macroscopic piezoresistive effects may be caused by microscopic damage induced in the Al-12Si coating structure due to strain, which can increase porosity and promote through-thickness crack propagation, resulting in a reduced conductive cross-sectional area in the Al-12Si coating.

Figure 5.8 a) to (f) show six graphs representing the electromechanical behaviour of each composite specimen evaluated by tensile testing. In each graph, the relationship between the laminate distributed load in the coated specimen and the axial strain in the prepreg substrate is shown by the black line, while the grey line indicates the relative change in electrical resistance $\left(\frac{\Delta R}{R_0}\right)_i$. The dashed line represents the δ model prediction from Eq. (51), using the optimized parameter a value shown in the graph. The adjusted coefficient of determination, $\underline{R}^2$, is also included as an indicator of the goodness of fit of δ to the experimental data. The experimental results of Fig. 5.8 a) to f) show that the coefficient of determination values ranged between 0.36 and 0.978, while optimum values for the a parameter ranged from 6.08 to 22.41. Figure 5.8 a) to f) also shows that higher values of the parameter a correlated to higher $\underline{R}^2$ values, which suggest that values for a between 15 and 22 may characterize the flame-sprayed Al-12Si coating electrical behaviour with respect to applied axial strain. Considering that the major Poisson ratio of the $[0°_8]$ FRPC has been estimated at 0.31 [160], the observed values of the parameter *a* point to macroscopic piezoresistive effects in the conduction of charges through the flame-sprayed Al-12Si coating under axial loads.

Equation (51) describes the electrical resistance change of the flame-sprayed Al-12Si coating deposited onto $[0°_2/90°_2]_S$, $[90°_2/0°_2]_S$, and $[0°_8]$ laminate fibre architectures, as shown in Fig. 5.8 a) to f). However, significant variation within the samples of the same fibre architecture remains unexplained. For instance, $[0°_2/90°_2]_S$ coated FRPC specimens exhibited electrical resistance changes of 4.58% (Fig. 5.8 a)) and 27.2% (Fig. 5.8 b)) at the point of structural failure (~18 mε), which represents a $\frac{27.2}{4.58} = 5.9\text{X}$ sensitivity change to strain between identically coated composite specimens. Similarly, sensitivity changes of 2X and 6.3X are obtained for $[90°_2/0°_2]_S$ and $[0°_8]$ composite specimens, respectively. The reason for the observed variability in relative electrical resistance behaviour of Al-12Si coatings is not evident, but it is deemed that porosity variation in the fabricated flame-sprayed Al-12Si coatings may contribute to it. Differences in coating porosity will greatly affect the mechanical and electrical properties of the flame-sprayed Al-12Si coatings independently of the substrate, and therefore can explain the observed differences in electrical behaviour of specimens with the identical fibre architecture, as shown in Fig. 5.8 a) to f).

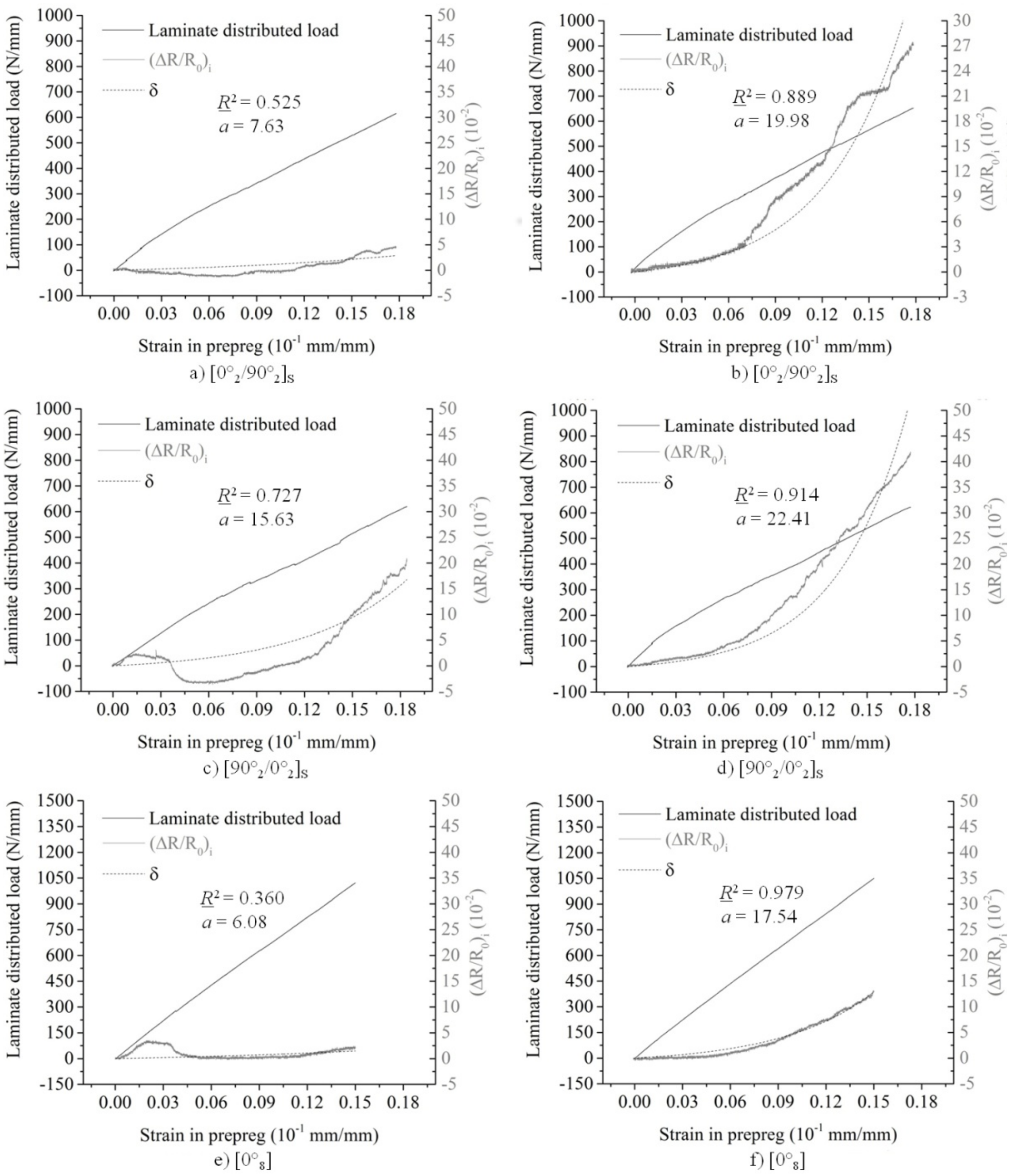

a) $[0°_2/90°_2]_S$

b) $[0°_2/90°_2]_S$

c) $[90°_2/0°_2]_S$

d) $[90°_2/0°_2]_S$

e) $[0°_8]$

f) $[0°_8]$

Figure 5.8: Relationship between the axial strain, the coated laminate load, the relative electrical resistance change of the Al-12Si coating, and the best-fit function *δ* for tested specimens: a) $[0°_2/90°_2]_S$ and *a* = 7.63, b) $[0°_2/90°_2]_S$ and *a* = 19.98, c) $[90°_2/0°_2]_S$ and *a* = 15.63, d) $[90°_2/0°_2]_S$ and *a* = 22.41, e) $[0°_8]$ and *a* = 6.08, and f) $[0°_8]$ and *a* = 17.54

Fabrication of flame-sprayed coatings with controlled porosity are required for the validation of general macroscopic models of the relative resistance change in flame-sprayed Al-12Si coatings due to strain, and may allow structural health monitoring of FRPC substrates by correlating strain levels to induced structural damage. Therefore, the framework model presented in Eq. (51) may provide a general description of the electromechanical behaviour of the flame-sprayed Al-12Si coating if consistent porosity levels exist in similarly coated composite specimens, as shown by the dependence on constant β and c parameters.

Considering the potential for electrical-based damage detection in FRPC substrates, Fig. 5.8 a) to f) shows a non-linear correlation between the axial strain in the prepreg substrate and the electrical resistance change of the flame sprayed Al-12Si coating. As shown in Fig. 5.8 a) to d), an increase in the measured electrical resistance change was observed beyond 7 mε strain in all the coated composite specimens. However, the electrical resistance of the flame sprayed Al-12Si coatings showed no consistent monotonic behaviour at low strain levels, which suggests that macroscopic piezoresistivity effects influence early damage detection in the FRPC substrate [180]. Moreover, it is hypothesized that the gibbousness observed at low strain levels in Fig. 5.8 c) and e) may be the result of reductions in the microstructural three-dimensional voids and crack cross-sectional area during the early deformation stages of the flame-sprayed Al-12Si coating. These microstructural changes may explain the observed transient decrement in the relative electrical resistance followed by the strictly monotonic behaviour of $\left(\frac{\Delta R}{R_0}\right)_i$, as the coating undergoes limited densification and compaction under axial loading, followed by geometry-dominated deformation at higher strain levels.

A gradual change in the slope of the laminate distributed load and axial strain curve of the cross-ply specimens can be observed between 3 mε and 7 mε in Fig. 5.8 a) to d). This change in stiffness indicates the occurrence of transversal matrix damage in the 90° plies of the cross-ply composite specimens. Examination of the tensile test data presented in Fig. 5.8 a) to d) suggests that the electrical resistance in the Al-12Si coating is not affected significantly by transverse matrix cracking in cross-ply FRPC laminates, since there is no notable change in electrical resistance of the flame-sprayed Al-12Si coating beyond 4mε, the value where transverse matrix cracking usually commences [173]. Also, Fig. 5.8 e) and f) show that no marked change in electrical resistance of the flame-sprayed Al-12Si coating occurred in the $[0°_8]$ specimens due to delamination until the last stages of the tensile test, which are dominated by fibre failure. Therefore, it provides further evidence that electrical resistance changes may be indicative of changes in the electrical properties of the Al-12Si coating with increasing strain, for example, due to micro-damage of the porous coating structure, rather than progressive damage in the FRPC substrate. Hence, the detection of early damage in the FRPC, i.e., transverse matrix cracking, seems unattainable by use of the flame-sprayed Al-12Si coatings. Examination of the microscopic electrical conduction properties of the flame-sprayed Al-12Si coatings may allow further consideration of a damage detection strategy based on localized electromechanical effects due to strain, in tandem with porosity-controlled coatings.

5.5 Conclusions

A framework for damage detection in symmetric cross-ply and unidirectional FRPC structures was considered using the electrical resistance change in flame-sprayed Al-12Si coatings. A macroscopic descriptive model of the relationship between the relative change in electrical resistance of the Al-12Si coating and the applied axial strain in the FRPC substrate was presented. The model has been shown to be capable of describing the evolution of the relative change in electrical resistance of the Al-12Si coating during tensile tests with satisfactory adjusted coefficient of determination values. However, significant variability was observed in the values of the electrical resistance change, possibly due to microstructural differences in the flame-sprayed Al-12Si coatings.

The suitability of the flame-spray Al-12Si coating for detecting strain induced damage in the FRPC was found to be limited to the late stages of failure dominated by fibre failure and delamination, where structural integrity is already compromised. Reliable detection of early matrix damage at low strain levels in the FRPC substrates was unattainable. Further microstructural characterization of flame-sprayed Al-12Si coatings with controlled porosity may allow the development of a damage detection strategy at low strain levels using the changes in the electrical properties.

Chapter 6 Economic Analysis

6.1 Introduction

In recent years, structural health monitoring (SHM) of fibre-reinforced polymer composite (FRPC) materials has been proposed in applications for the aerospace [181, 182] and oil/gas pipe [183] industries. The cost-effective implementation of SHM sensors in FRPC structures depends on technical and economic factors. However, there is limited literature available on the economic aspects of the SHM sensor implementation in FRPC structures. Moreover, the increasing importance of SHM sensor economics is evidenced by market research activity on SHM technology impact and value chain [184]. In this context, the economic analysis of the proposed flame-sprayed SHM sensor (FS SHM sensor) can contribute to the assessment of the significance and potential impact of this novel approach to SHM in FRPC structures.

The study of the cost structure of the thermal spray technology is required to develop commercially unexplored applications [40, 65], such as the advancement of functional flame-spray coatings for SHM purposes. In this Chapter, the economic analysis of the proposed FS SHM sensor is performed to investigate the cost efficiency of the damage detection unit at the current development stage, using oil and gas FRPC pipes as the potential target application. In addition, the financial performance of the FS SHM sensor is evaluated with respect to a commercially available SHM sensor for FRPC pipes based on Fibre Bragg Grating (FBG) technology, which is the predominant optical SHM technology for civil infrastructure [185]. The Fibre Bragg Grating SHM sensor (FBG SHM sensor) reflects a wavelength of light that shifts in response to variations in strain due to periodic alterations in the refractive index of the fibre core [186, 187]. Moreover, several studies have explored the use of FBG sensors for structural health monitoring of FRPC structures [188-191] due to the following FBG properties [187, 190, 192, 193]: (i) high corrosion resistance and durability; (ii) high elongation range (up to 5% strain) and application to different surfaces (i.e., cylindrical pipes, flat elements); and (iii) low invasiveness and minimum electromagnetic interference and capacity to provide remote damage detection.

The concurrent evaluation of the cost performance of the proposed FS SHM sensor and the FBG SHM sensor can facilitate the identification of economic and operational factors for further technology development and competitive implementation of SHM in FRPC structures, which is in good agreement with several studies on technologically driven proposals for the energy sector in Canada [194, 195]. The objectives of this economic analysis were to: (1) compare the capital costs of the FS and FBG SHM sensors, (2) ascertain the distribution of capital and operational direct costs of the FS and FBG SHM sensors, and (3) calculate the Net Present Value of the FS and FBG SHM sensor applications.

6.2 Methods of analysis

6.2.1 Physical unit

A FRPC specimen exhibiting a $[0°_2/90°_2]_S$ fibre architecture was selected to develop an economic analysis of the flame-sprayed SHM sensor (FS SHM sensor) described in Chapter 5. A Fibre Bragg Grating (FBG) was attached to the gage length of the FS SHM sensor to provide an alternative SHM sensing unit for the FRPC substrate. A commercially-available polyimide FBG (OFS BF06158-02, Technica Optical Components LLC, Reno, NV, USA) was bonded at two consecutive points on the side edge of the FRPC, as shown in Fig. 6.1. During the bonding of each contact point, a tension of 1 N was applied to the FBG free end using a metrology weight, which ensured axial alignment of the FBG to the side edge of the FRPC. Upon bonding the FBG, the metrology weight was removed, and the FBG was connected to a FBG interrogator (SmartScan, Smart Fibres Ltd., Bracknell, Berkshire, United Kingdom) to form a FBG SHM sensor. Figure 6.1 illustrates the configuration of the FS and FBG SHM sensors installed on the physical unit. The fabrication of the physical unit shown in Fig 6.1 allowed an evaluation of capital and operational costs components of the FS and FBG SHM sensors at their current development stage. All FS and FBG sensor cost values presented in this study are costs per physical unit, which corresponds to a FRPC structure with a characteristic length of 140 mm with one SHM sensor of each type, as shown in Fig 6.1.

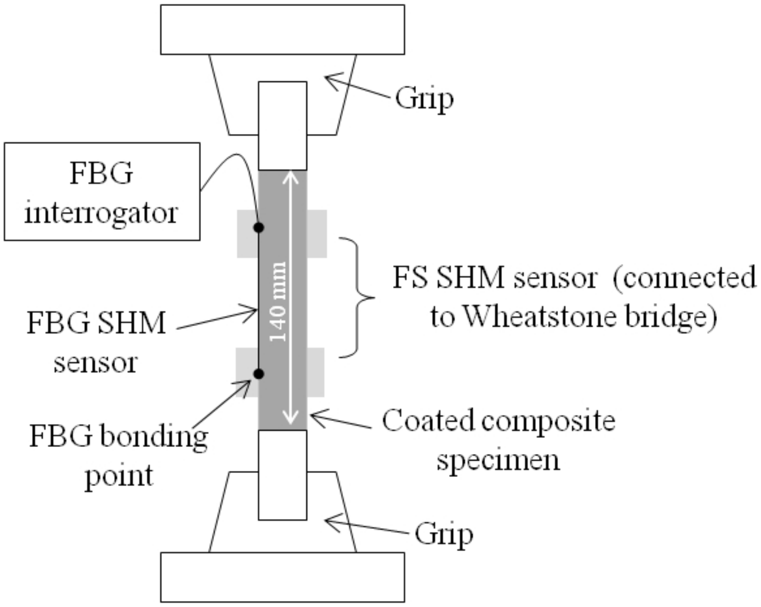

Figure 6.1: Schematic of the physical unit for cost analysis, showing the FS and FBG SHM sensors upon installation on the coated composite specimen

6.2.2 Capital and operating costs

End user initial capital cost (ICC) and operating cost were estimated for the FS and FBG SHM sensors. Canadian Dollars ($) were used as the currency to express the FS and SHM sensor costs in the present economic analysis. An exchange rate of $1.21025 per American Dollar (US$) was applied to authoritative estimates where applicable, as per the average official exchange rate between these two currencies as current to May 1st, 2015 [196].

The end user ICC of the FBG SHM sensor, ICC_{FBG}, was estimated by:

$$ICC_{\text{FBG}} = C_{\text{FBG-retail}} + C_{\text{FBGi-retail}}, \tag{56}$$

where $C_{\text{FBG-retail}}$, is the retail costs of the FBG unit, and $C_{\text{FBGi-retail}}$ is the retail cost of one FBG interrogator. A value of \$121.02 (US\$100) was used for $C_{\text{FBGi-retail}}$ in Eq. (56) based on the FBG retail cost in April 14th, 2015. The cost of the FBG interrogator was estimated at \$12,102.50 (US\$10,000) per unit, based on supplier information [197]. Since the FBG interrogator can be connected to up to 16 FBGs, a cost contribution of \$756.41 (12102.50/16) was used as the FBG interrogator retail cost for the FBG SHM sensor in Eq. (56). Other FBG SHM sensor installation costs, such as bonding adhesive and labour costs, were not considered in this study due to the possibility to integrate the FBG into the fibre-reinforced polymer structure during the composite fabrication.

The FS SHM sensor is not currently available, and hence the end user ICC of the FS SHM sensor included manufacturing direct costs and applicable cost markups for the end user. Direct costs are defined as expenses incurred before the FS SHM sensors are operational, such as material, labour, and installation costs [198]. Three markup categories were considered for end user ICC of the FS SHM sensor: (1) cost contingency, (2) allowance for fixed cost, and (3) allowance for retail and distribution cost. The end user ICC of the FS SHM sensor, ICC_{FS}, was estimated as follows:

$$ICC_{\mathrm{FS}} = C_{\mathrm{FSdirect}} \cdot (1 + m_{\mathrm{c}}) \cdot (1 + m_{\mathrm{f}}) \cdot (1 + m_{\mathrm{r}}) , \tag{57}$$

where C_{FSdirect} is the manufacturing direct cost of the FS SHM sensor, m_{c} is the cost contingency markup rate, m_{f} is fixed cost markup rate, and m_{r} is the retail and distribution markup rate. A conservative cost contingency markup value of 0.3 was used, to account for any unexpected variation in current cost estimates due to manufacturing factors. A fixed cost markup value of 0.35 was estimated based on the ratio between the operating and administrative cost (SG&A) and the revenue of a North-American structural sensor firm in the 2014 third quarter (Q3) income statement [199, 200]. A retail and distribution markup value of 0.43 was selected, which is equal to the sum of the average markups for retail trade, transportation, and warehousing in Canada during the period between 1961 and 2004 [201].

The manufacturing direct cost of the FS SHM sensor presented in Eq. (57) was divided into two cost categories: (1) flame spray direct costs and (2) complementary direct costs. Flame spray direct cost comprised all direct costs incurred during flame spray deposition of the aluminium-12silicon (Al-12Si) coating, as part of the FS SHM sensor fabrication. Complimentary direct costs included the manufacturing direct costs not incurred during the Al-12Si flame spray deposition, such as surface preparation, complementary labour, and Wheatstone bridge costs. The manufacturing direct cost of the FS SHM sensor, C_{FSdirect}, was determined using the following expression:

$$C_{\mathrm{FSdirect}} = C_{\mathrm{FS}} + C_{\mathrm{comp}} \tag{58}$$

where C_{FS} is the flame spray direct cost and C_{comp} is the complementary direct costs of the FS SHM sensor. A diagram showing the structure of ICC_{FS} (Eq. (57)) is shown in Fig. 6.2.

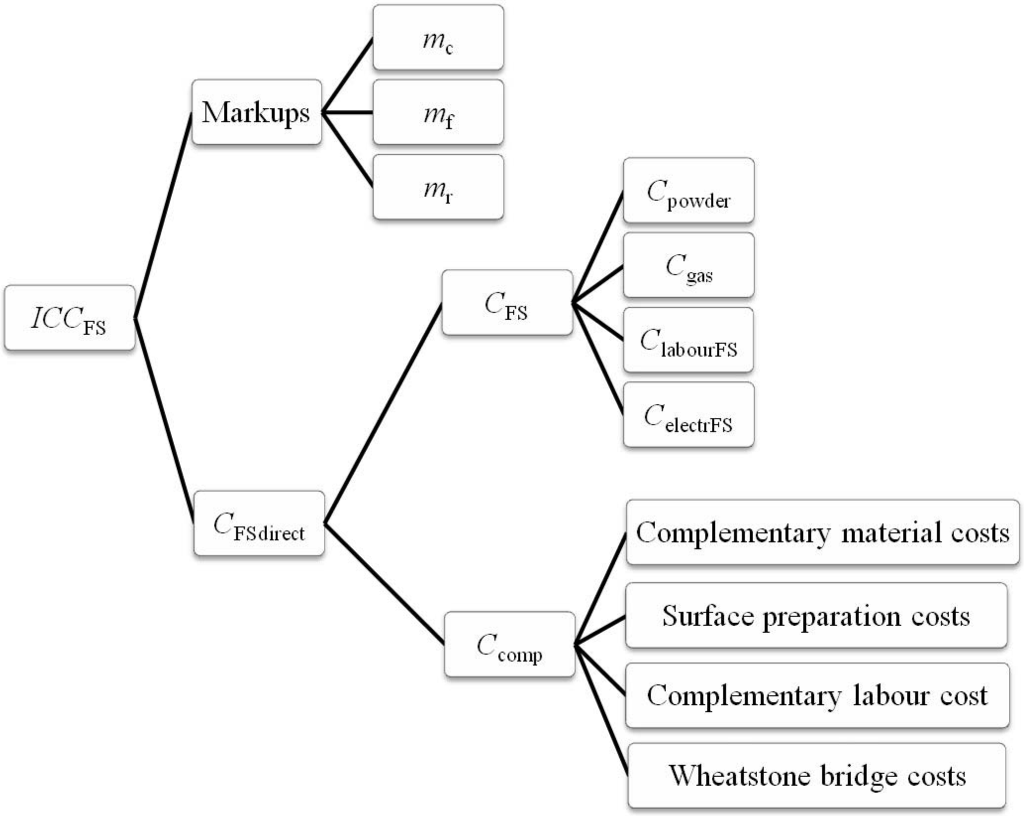

Figure 6.2: Structure of the initial capital costs of the FS SHM sensor (ICC_{FS}) showing manufacturing direct cost ($C_{FSdirect}$), markups, flame spray direct costs (C_{FS}), and complementary direct costs (C_{comp})

The estimation of the complementary direct costs of the FS SHM sensor is presented in the Appendix A of this thesis document. Flame spray direct costs were estimated using a cost model for powder, gas, labour, and electrical costs during the fabrication of the FS SHM sensor, which is described in the next subsection. The initial capital cost values of the FBG SHM sensor (Eq. (56)) and FS SHM sensor (Eq. (57)) were utilized to estimate the present investment required to bring the sensor device to an installed and commercially operable status.

In addition to ICC_{FS} and ICC_{FBG}, operating costs were estimated for the FS and FBG SHM sensors. Operating costs are defined as time dependent costs incurred once the SHM sensor is in service. The operating cost of the FS SHM sensor, O_{FS}, and the FBG SHM sensor, O_{FBG}, were determined using direct current (DC) electricity costs as follows:

$$O_{\mathrm{FS}} = C_{\mathrm{fsDC}} + ICC_{\mathrm{FS}} \cdot m_{\mathrm{op}} \tag{59}$$

$$O_{\mathrm{FBG}} = C_{\mathrm{fbgDC}} \tag{60}$$

where m_{op} is the annual maintenance allowance for the FS SHM sensor, C_{fsDC} is the annual DC electricity cost of the FS SHM sensor, and C_{fbgDC} is the annual DC electricity cost of the FBG SHM sensor. In Eq. (59), an annual maintenance allowance equal to 3% of ICC_{FS} was used to account for the higher uncertainty perceived in the long-term implementation of the novel FS SHM sensor technology with respect to that of the FBG SHM sensor, which is accepted and in use in industry [187]. In Eq. (59) and Eq. (60), C_{fsDC} and C_{fbgDC} were estimated using the average DC power $\underline{P}$ dissipated by the given SHM sensor while in service. The annual DC electricity cost of the FS SHM sensor, C_{fsDC}, and the FBG SHM sensor, C_{fbgDC}, were estimated as follows [202]:

$$C_{\text{fsDC}} = \frac{1}{\eta} \cdot \underline{P}_{FS} \cdot \underline{t}_{\text{on}} \cdot U_{\text{electr}}, \tag{61}$$

$$C_{\text{fbgDC}} = \frac{1}{\eta} \cdot \underline{P}_{FBG} \cdot \underline{t}_{\text{on}} \cdot U_{\text{electr}}, \tag{62}$$

where the subscripts denote the $\underline{P}$ value of the given sensor, U_{electr} is the cost of electricity (i.e. cost of the kWh), $\eta = 0.811$ is the maximum efficiency of a full-wave alternate-to-direct current rectifier [203], and $\underline{t}_{\text{on}}$ is the annual operation time designated for both the FS and FBG SHM sensors. Since SHM sensors are usually commissioned to provide long-term continuous damage detection, a value of 8765.81 hours per annum is used for $\underline{t}_{\text{on}}$ in this study, which represents the time of a standard calendar year adjusted for leap years. Table 6.1 shows the average DC power $\underline{P}$ dissipated by the FS SHM sensor ($\underline{P}_{\text{FS}}$) and FBG SHM sensors ($\underline{P}_{\text{FS}}$), respectively. The average DC power of the FS SHM sensor was calculated using the electrical measurements of current and voltage over a period of 300 s [202], as shown in Table 6.1. All time measurements of this study were performed using a stopwatch and rounded to the nearest tenth of a second. The cost of electricity, U_{electr}, used for all electrical cost calculations in this study was \$0.15 per kWh, which corresponds to the sum of the average electricity cost of the regulated electricity service in Alberta in 2014 (\$0.08 per kWh) [204] and an assumed electrical transmission and distribution costs of \$0.07 per kWh on-site for the end user.

Table 6.1: Average DC power ($\underline{P}$) dissipated by FS and FBG SHM sensors

DC Electrical equipment	**$\underline{P}$ (W)**	**Estimation method**
FS SHM sensor and Wheatstone bridge	0.41	Product of the average electrical current and voltage in a period of 300 s
FBG SHM sensor and interrogator	7.5	Manufacturer specifications [197]

6.2.2.1 Flame spray direct cost model

The flame spray direct cost (C_{FS}) constitutes a subset of the manufacturing direct costs of the FS SHM sensor (C_{FSdirect}), as shown in Fig. 6.2. An economic model was construed to estimate the flame spray direct costs of the FS SHM sensor, using the methodology developed in a previous economic study on the cold spray process [65]. The flame spray direct cost of the FS SHM sensor, C_{FS}, was estimated as follows:

$$C_{\mathrm{FS}} = C_{\mathrm{powder}} + C_{\mathrm{gas}} + C_{\mathrm{labourFS}} + C_{\mathrm{electrFS}}, \tag{63}$$

where C_{powder} is the cost of the feedstock powder, C_{gas} is the cost of the consumable gases, C_{labourFS} is the flame spray labour cost, and C_{electrFS} is the electricity cost of the flame spray process equipment during deposition (i.e. robot and powder feeding control). Flame spray labour costs in Eq. (63) were estimated using an estimated thermal spray operator wage of \$42.01 per hour (wage and benefits) and a measured flame spray labour time of 0.88 hours per FS SHM sensor. The assessment of powder, gas, and electrical flame spray costs is described in the remainder of this subsection.

Powder costs were estimated using the expense of Al-12Si feedstock powder during the flame spray deposition process. The powder cost of the FS SHM sensor was calculated as [65]:

$$C_{\text{powder}} = \frac{(1+G)}{Y} m_{\text{c}} \cdot U_{\text{powder}}, \qquad (64)$$

where U_{powder} denotes the cost of Al-12Si powder per unit of mass, G is the geometric loss factor of the Al-12Si flame spray deposition, m_c is the mass of the Al-12Si flame spray deposit (i.e. dual-sided Al-12Si coatings in the FS SHM sensor), and Y is the Al-12Si deposition efficiency [64, 65]. A value of \$80.86 per kg was used for U_{powder} in this study, based on the price of Al-12Si powder (Metco 52C-NS) provided by Oerlikon Metco (Westbury, NY, USA) in May 2015.

The G parameter shown in Eq. (64) is a consequence of the fact that flame spraying is usually performed on a larger spray area than the presented workpiece area to maintain a uniform deposition, which is affected by the turning points in the nozzle tracks [65]. During flame spraying of the FS SHM sensor, uniform Al-12Si coating deposition on the prepared FRPC was achieved by extending the nozzle tracks beyond the FRPC workpiece edges, resulting in a total deposition area that was greater than that of the FRPC workpiece, by a factor of 1+G. The geometric loss factor G in Eq. (64) was determined using the formula [65]:

$$G = \frac{A_{\text{total}} - A_{\text{w}}}{A_{\text{w}}}, \tag{65}$$

where A_{w} is the area of the prepared FRPC workpiece, and A_{total} is the total area covered by the nozzle deposition tracks during Al-12Si deposition. Figure 6.3 shows the relationship between the A_{total} and A_{w} for a centered rectangular workpiece profile, such as the FRPC substrate of the FS SHM sensor. The coated profile of the FS SHM sensor exhibited an horizontal length l of 140 mm and a vertical height b of 25.4 mm, resulting in a coated area $A_{\text{w}} = bl$ of 3556 mm². The total deposition area of the FRPC workpiece, A_{total} in Eq. (65) was calculated as:

$$A_{\text{total}} = (l + 2\delta_1)(b + 2\delta_2), \tag{66}$$

where δ_1 and δ_2 are the designated overspray lengths in the horizontal and vertical directions, respectively, as illustrated in Fig. 6.3. A value of 22280 mm² was calculated for A_{total} using the standard overspray length values of $\delta_1 = 76.2$ mm and $\delta_2 = 25.4$ mm [205]. A geometric loss factor of 5.26 was determined for the FS SHM sensor from Eq. (65) and Eq. (66).

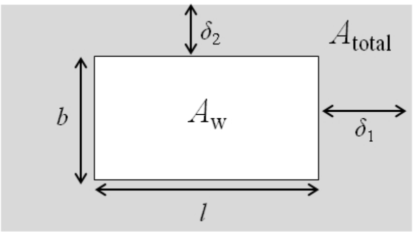

Figure 6.3: Representation of the total spray area (A_{total}) for the centered rectangular workpiece of area A_{w}

In Eq. (64), the mass of the Al-12Si flame spray deposit m_c was calculated to be 3.55 g using differential weight measurements between coated and uncoated FRPC specimens. The deposition efficiency Y in Eq. (64) was determined using the following formula [64, 65]:

$$Y = \frac{m_{\text{c}}}{m_{\text{powder}}}, \tag{67}$$

where m_{powder} is the weight of impacting Al-12Si deposition particles. A fine spandex fabric barrier was attached to the outlet of the unignited flame spray nozzle to collect the Al-12Si particles accelerated by the powder carrier gas flow, which consisted of argon at a flowrate identical to that used for FS SHM fabrication (7.08 L/min). The average powder spray rate was estimated by measuring the weight of the Al-12Si particles collected inside the spandex barrier in 60 s of active powder gas flow. The average powder spray rate was multiplied by the measured deposition time required for FS SHM fabrication to determine the m_{powder}, which was estimated to be 37.1 g. Using Eq (67) and values for m_c and

m_{powder}, a deposition efficiency Y of 0.096 was determined for Al-12Si deposition, as part of the FS SHM sensor fabrication process. The powder cost of the FS SHM sensor in Eq. (64) was estimated using the U_{powder}, G, m_c, and Y values.

In addition to powder expenses, an evaluation of flame spray gas cost presented in Eq. (63) was performed. Flame spray gas cost comprised the expenditure for argon carrier gas for the powder and acetylene and oxygen combustion gases for Al-12Si coating deposition using relatively low gas pressures. The flame spraying cost of a given gas, X_{gas}, was estimated by:

$$X_{\text{gas}} = \frac{t_{\text{run}}}{t_{\text{bottle}}} \cdot U_{\text{bottle}}, \tag{68}$$

where t_{run} is the time the gas flow is flowing during the FS SHM sensor fabrication process, t_{bottle} is the time required to consume the cylinder bottle of the given gas, and U_{bottle} is the cost of one full gas cylinder bottle. The estimated value of t_{run} for each gas is presented in Table 6.2. The ideal gas law was used to calculate t_{bottle} in Eq. (68), by estimating the equivalent volume of each gas entering the flame spray nozzle, V_{run}, assuming an isothermal process [206]:

$$V_{\text{run}} = \frac{P_{\text{SPT}} \cdot V_{\text{bottle-STP}}}{P_{\text{run}}}, \tag{69}$$

where $V_{\text{bottle-STP}}$ is the designated total volume of the given gas in the cylinder gas bottle under standard conditions of temperature (20 to 30°C) and pressure (1 atm) [167], P_{run} is the set outlet pressure of the gas entering the flame spray nozzle, and P_{STP} is the standard pressure of 1 atm (101.325 kPa). The value of t_{bottle} for each gas was calculated using the following formula:

$$t_{\mathrm{bottle}} = \frac{V_{\mathrm{run}}}{\upsilon_{\mathrm{run}}}, \tag{70}$$

where υ_{run} is the set outlet flowrate of the given gas at P_{run} and standard conditions of temperature. Table 6.2 summarizes the parameters used to estimate the flame spray gas costs of the FS SHM sensor, including the gas cylinder information and costs, as provided by Praxair Canada Inc. in April 2015. The information presented on Table 6.2 was used in tandem with Eqs. (68), (69), and (70) to estimate the argon, oxygen, and acetylene gas costs of the FS SHM sensor. The flame spraying cost of the FS SHM sensor (C_{gas}) in Eq. (63) was estimated using the following expression:

$$C_{\mathrm{gas}} = X_{\mathrm{argon}} + X_{\mathrm{acetylene}} + X_{\mathrm{oxygen}}, \tag{71}$$

where the subscripts denote the given gas cost, defined as per Eq. (68).

Table 6.2: Economic flame spray gas parameters of the FS SHM sensor fabrication including: the designated volume of the gas bottle ($V_{\text{bottle-STP}}$), the outlet pressure of gas (P_{run}), the set outlet flowrate (υ_{run}), the flow time of the gas (t_{run}), and the cost per gas bottle (U_{bottle})

Gas	**Cylinder pressure (kPa)**	$\boldsymbol{V_{\text{bottle-STP}}}$ **(L)**	$\boldsymbol{P_{\text{run}}}$ **(kPa)**	$\boldsymbol{\upsilon_{\text{run}}}$ **(L/min)**	$\boldsymbol{t_{\text{run}}}$ **(s)**	$\boldsymbol{U_{\text{bottle}}}$ **($)**
Argon	18303	9486	515	7.08	296.8	56.32
Oxygen	18303	9543	342.6	25	465.8	20.83
Acetylene	1825	9345	204.75	8	584.1	167.16

Estimation of the electrical cost (C_{electrFS}) in Eq. (63) was performed as part of the FS SHM sensor cost structure shown in Fig. 6.2. Three alternating current (AC) pieces of equipment were considered in the estimation of the flame spray electrical cost: the spray-tracking HP-20 robot arm, the 5MPE volumetric powder feed unit, and the 9MC gas flow controller. The flame spray electrical cost of the FS SHM sensor, C_{electrFS}, was determined using the average real AC power $\underline{\underline{P}}$ and run time t_{on} during the flame spray process, which was calculated as follows [202]:

$$C_{\text{electrFS}}=(\underline{\underline{P}}_{\text{9MC}}\cdot t_{\text{on\_9MC}}+\underline{\underline{P}}_{\text{5MPE}}\cdot t_{\text{on\_5MPE}}+\underline{\underline{P}}_{\text{robot}}\cdot t_{\text{on\_robot}})\cdot U_{\text{electr}}, \tag{72}$$

where the subscripts indicate the given AC electrical equipment, and U_{electr} is the cost per unit of electricity ($0.08 per kWh). Estimation of $\underline{\underline{P}}$ values of the 9MC, the 5MPE, and the HP-20 robot arm in Eq. (72) was performed using the following expression [202]:

$$\underline{\underline{P}} = \underline{\underline{Z}} \cdot p_{\mathrm{f}}, \tag{73}$$

where $\underline{\underline{Z}}$ is the apparent AC power expressed in Volt-Amperes (VA) and p_{f} is the power factor corresponding to the phase difference between the supplied current and voltage. As shown in Table 6.3, manufacturer specifications for $\underline{\underline{P}}$ and $\underline{\underline{Z}}$ values were used for the 9MC, the 5MPE, and the HP-20 robot arm, when available. A power factor of 0.2 was used to calculate $\underline{\underline{P}}_{\mathrm{robot}}$, considering a low load for the servomotor during spray nozzle motion [207]. A power factor equal to 1 was assumed for $\underline{\underline{P}}_{\mathrm{9MC}}$ calculations to provide the maximum dissipated power estimate in Eq. (73). The run time (t_{on}) in Eq. (72) was estimated using recorded time measurements during the Al-12Si deposition process, as part of the FS SHM sensor fabrication. Table 6.3 summarizes the dissipated power and run time values of the AC electrical equipment used to fabricate the FS SHM sensor. Based on Eq. (72), the values shown in Table 6.3 allowed the estimation of the electrical cost C_{electrFS} presented in Eq. (65).

Table 6.3: Electricity cost parameters for FS SHM sensor fabrication showing the equipment AC power ($\underline{\underline{P}}$) and run time ($t_{\mathrm{run}}$)

AC Electrical equipment	**$\underline{\underline{P}}$ (kW)**	**t_{on} (s)**	**Manufacturer specifications**
9MC	1.104	296.8	$\underline{\underline{Z}}$=1.104 kVA [208]
5ME	0.075	213.6	$\underline{\underline{P}}$=75 W [209]
HP-20 robot	0.56	120.6	$\underline{\underline{Z}}$=2.8 kVA [210]

The flame spray direct cost (C_{FS}) of the FS SHM sensor was estimated using the presented methodology in this subsection. As shown in Fig. 6.2, the flame spray direct cost contributed to the estimation of the $\mathrm{ICC}_{\mathrm{FS}}$ value, which was used in the discounted cash flow analysis of the FS SHM sensor.

6.2.3 Discounted cash flow analysis

The ICC and operating costs of the FS SHM sensor were compared to those of the FBG SHM sensor to determine the incremental ICC and incremental operating costs for each SHM sensor. Incremental costs are defined as expenses that are unidentical in attribute or value between the FS SHM sensor and the FBG SHM sensor [198]. The sensor deployment costs, such as electrical power supply and data acquisition units costs, were assumed to be identical (non-incremental) for both sensors, and were not considered in the economic analysis.

A 20-year operation time for the FS and FBG SHM sensors was used in the study and was based on the reported design life of FRPC pipes in the Canadian oil and gas industry [211], which is considered the primary area of potential application. The annual operating costs of the FS and FBG sensors presented in Eq. (59) and (60) were assumed to be paid at the end of the year, as per conventional DCF practices [198, 212].

The incremental ICC and operating costs of the FS SHM sensor and the FBG sensor can be represented as a series of cash flow expenses over the sensor operation time [198, 212]. The expenses in the cash flow series start with ICC at time $t = 0$, which corresponds to the present time in 2015, and continue with the operating costs for the 20-year operation time of the SHM sensor, as illustrated in Fig 6.4. End user cash flows are represented as vector arrows in Fig. 6.4. The length of the arrow is proportional to the cash flow value, while the direction of the arrow indicates the cash flow sign, i.e. a down arrow represents a negative cash flow or cost. The cost cash flows of a given SHM sensor during the 20-year operation time is herein called ‘characteristic cash flows’. The characteristic cash flows of the FS and FBG SHM sensors constituted pre-tax expenses over the 20-year operation time.

Fundamental tax deductions were applied to the characteristic cash flows of the FS and FBG SHM sensors in order to obtain the after-tax cash flows, using

Capital Cost Allowance (CCA) and corporate tax rates [200, 212]. The CCA was calculated for the FS and FBG SHM sensor operating costs utilizing the Undepreciated Capital Cost (UCC) and the half-year rule, as per standard financial practices in Canada [200, 212]. The calculation of the UCC and CCA values in the n-th year ($t = n$) was performed as follows [200, 212]:

$$\tau_n = \begin{cases} 0.5\,|ICC|, & \text{if } t = 0 \\ 0, & \text{if } t > 0 \end{cases} \tag{74}$$

$$UCC_n = UCC_{n-1} + \tau_n - CCA_n \ , \ n \neq 1 \tag{75}$$

$$UCC_{-1} = 0 \quad ; \quad UCC_1 = |ICC| + \tau_n - CCA_n \quad ; \quad CCA_0 = 0 \tag{76}$$

$$CCA_n = r \cdot (UCC_{n-1} + \tau_n) \ , \ n > 0, \tag{77}$$

where ICC is the initial capital cost of the SHM sensor (year $t = 0$), τ_n is the transaction value to account for the half-year rule for UCC [200, 212], r is the CCA rate, CCA_n is the capital costs allowance in the year $t = n$, and UCC_n and UCC_{n-1} are the undepreciated capital costs in the year $t = n$ and $t = n$-1, respectively.

FS and FBG SHM sensors were considered as data network infrastructure equipment under CCA class 46, which has a rate of $r = 30\%$, as per Canada Revenue Agency regulations [213]. In tandem with CCA, an effective corporate tax rate of 27% [214-216] was applied to the difference between the characteristic cash flows and the CCA values of the FS and FBG SHM sensors to calculate the tax amount. The selected tax rate is based on the expected tax rate in Alberta at the end of 2015. The difference between the characteristic cash flows and the tax amount determined the after-tax cash flows of the of the FS and FBG SHM sensors.

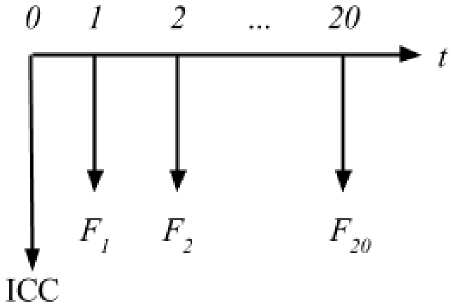

Figure 6.4: Representation of the SHM sensor after-tax cash flows over time *t*, including the incremental ICC and the incremental operating costs (F_1, F_2,..., F_{20}) in a 20-year period

Using the base year of 2015 for cost values, a discounted cash flow (DCF) analysis [198, 212] was performed using the after-tax cash flows of the FS and FBG SHM sensors. The DCF analysis methodology is based on the concept of time value of money [217], which is defined as the variation in the earning potential, risk, and the relative purchasing power (inflation or deflation) of money over time [212]. A future after-tax cash flow of a given SHM sensor was assumed to be mathematically equivalent to a discounted (reduced) after-tax cash flow in the present, in accordance with the time value of money. The after-tax cash flow F_n at the end of the *n*-th year ($t = n$) was discounted to the after-tax present value P_n at $t = 0$ using the following formula [198]:

$$P_n = \frac{F_n}{(1+i)^n}, \tag{78}$$

where i is the annual effective real discount rate, (e.g., 1% per annum) . Figure 6.5 illustrates the discounting of a given future after-tax cash flow F_n in n years to obtain the equivalent present after-tax cash flow P_n, based on the concept of time value of money.

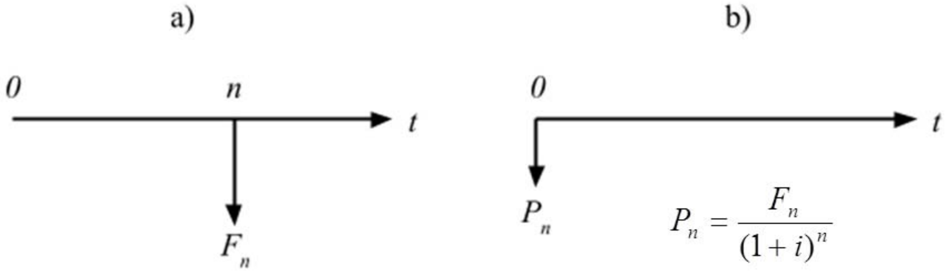

Figure 6.5: Illustration of the concept of time value of money using an annual effective real discount rate i : a) a future after-tax cash flow F_n in n years and b) the equivalent present after-tax cash flow P_n for F_n

The discount rate i in Eq. (78) is a parameter that defines the average (i.e. constant) rate of the time value of money [198], as per conventional financial practices in DCF analysis [198, 212]. The annual effective real discount rate i in Eq. (78) was estimated as follows [198]:

$$i = \frac{i_{\mathrm{n}} - f}{1+f}, \tag{79}$$

where f is the annual inflation rate and i_n is the inflation-free discount rate per year. An annual inflation rate value of $f = 3\%$ was assumed for the 20-year project period based on a conservative appraisal of the Bank of Canada's target of 2% from 2012 to date [218]. Values for i_n equal 8.15% and 15.36% were selected based on typical discount rates for public and corporate investments, respectively [212]. Annual effective real discount rates were determined at $i_{\text{public}} = 5\%$ and $i_{\text{corp}} = 12\%$ for public and corporate investment analysis, respectively [212]. These annual effective real discount rates were applied independently to the after-tax cash flows of the FS and FBG SHM sensors leading to four different investment options, as shown in Table 6.4. The four investment options resulted from the combinations of i values and after-tax cash flows of FS and FBG SHM sensors considered in the DCF analysis. As shown in Table 6.4, the FS and FBG SHM sensors were evaluated as two mutually exclusive investment options [192, 194, 212, 219] using the i_{public} and i_{corp} discount rates.

Table 6.4: Investment options considered in the DCF analysis of FS and FBG SHM sensors, respectively

		Annual effective real discount rate *i*	
		$i_{\text{public}} = 5\%$	**$i_{\text{corp}} = 12\%$**
After-tax cash flows	FBG SHM sensor	Public investment option 1	Corporate investment option 1
	FS SHM sensor	Public investment option 2	Corporate investment option 2

For a given investment option shown in Table 6.4, the equivalent discounted P_n values of each after-tax cash flow at a time $t = 1,2,...,n$ was calculated using Eq. (78). The Net Present Value (NPV) of the given investment option was calculated as the sum of all discounted P_n values, using the following expression [198, 212]:

$$\mathrm{NPV} = \sum_{n=0}^{20} P_n = \sum_{n=0}^{20} \frac{F_n}{(1+i)^n} = \mathrm{ICC} + \sum_{n=1}^{20} \frac{F_n}{(1+i)^n}, \tag{80}$$

which represents a measure of the after-tax cash flow of a SHM sensor at a given i, as illustrated in Fig. 6.6. The NPV was utilized as the estimate of the long-term financial performance [198, 212, 217, 219] of the after-tax cash flows of the FS and FBG SHM sensors, based on Eqs. (56), (57), and (80).

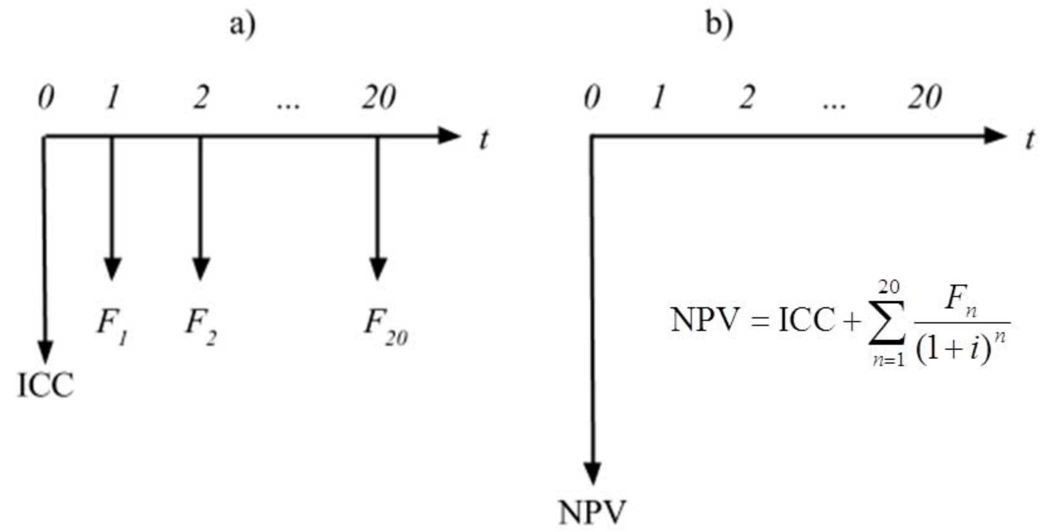

$$\mathrm{NPV} = \mathrm{ICC} + \sum_{n=1}^{20} \frac{F_n}{(1+i)^n}$$

Figure 6.6: Representation of: a) the SHM sensor after-tax cash flows and b) the equivalent NPV of the SHM sensor after-tax cash flows , at a given annual effective real discount rate i

6.3 Results and discussion

The estimated end user ICC of the FBG SHM sensor ICC_{FBG} is estimated at \$877.43, based on Eq. (56). The general distribution of the ICC of the FS and FBG SHM sensors is illustrated in Fig.6.7. The FBG interrogator cost represents \$754.41 (86.21%) of the ICC of the FBG SHM sensor, while the polyimide FBG contributes the remainder \$121.02 (13.79%). Alternatively, the end user ICC of the FS SHM sensor, ICC_{FS}, is estimated at a value of \$273.46, which includes \$108.95 (39.84%) in manufacturing direct costs (C_{FSdirect}) and \$164.51 (60.16%) in combined markups (ICC_{FS} minus C_{FSdirect}), as per Eq. (57). The combined contingency, fixed costs, and retail and distribution markup costs represent approximately 1.5 times the manufacturing direct cost of the FS SHM sensor, which is commensurate with typical price-cost margins for a novel technology [200]. Even though the cost of the FBG interrogator is expected to decrease as the FBG technology becomes more prevalent for SHM purposes [184, 187], the current initial capital cost of the FBG SHM sensor is considerably higher than that of the FS SHM sensor, as shown in Fig. 6.7.

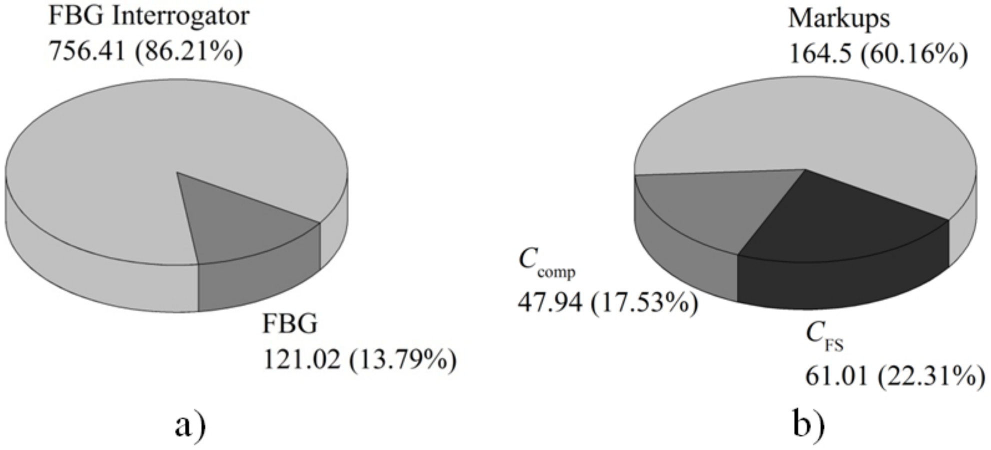

Figure 6.7: Distribution of the initial capital cost in: a) FBG SHM sensor and b) FS SHM sensor, which shows the flame spray direct cost (C_{FS}) and the complementary direct cost (C_{comp})

In Fig.6.7, the two cost components of $C_{FSdirect}$ are shown, which comprise the flame spray direct cost (C_{FS}) and the complementary direct cost (C_{comp}), as per Eq. (58). The flame spray direct cost account for \$61.01 (22.31%) of the ICC_{FS}, which is greater than that of the complementary direct costs (\$47.94 (17.53%)).

Therefore, the flame spray process contributes a significant fraction to the FS SHM sensor manufacturing cost. The distribution of the flame spray direct cost of the FS SHM sensor is shown in Fig. 6.8. Considering the flame spray direct cost (C_{FS}) model presented in Eq. (63), the following four cost categories are discussed: labour cost (C_{labourFS}), gas cost (C_{gas}), powder cost (C_{powder}), and electricity cost (C_{eletrFS}).

The flame spray labour cost constitutes the most significant component of the flame spray direct cost of the FS SHM sensor at \$36.98 (60.61%), as shown in Fig. 6.8. Therefore, there is a potential for reduced manufacturing costs in the FS SHM sensor by introducing a higher degree of automation in the flame spray process, which is consistent with the industrial automation trend in thermal spraying [65, 220, 221].

As illustrated in Fig. 6.8, flame spray gas costs account for \$5.3 (8.69%) of the flame spray direct cost, distributed among argon (\$1.06), oxygen (\$1.43), and acetylene (\$2.81) expenses. Flame spray costs are proportional to the outlet flowrate (υ_{run}) and the cost of the bottle of the gas (U_{bottle}), as per Eqs. (68) and (70). Therefore, the higher U_{bottle} value of acetylene produces the most significant gas cost in the fabrication of the FS SHM sensor, in spite of exhibiting the lowest outlet flowrate (υ_{run}) value, as shown in Table 6.2. Considering that acetylene, argon, and oxygen gas specifications for the FS SHM sensor fabrication are constrained, technical and economic factors should be considered to lower the current gas costs, which are dependent on the flame spray nozzle geometry and outlet pressure (P_{run}) of the powder carrier gas and combustion gases.

Flame spray powder costs represent \$18.72 (30.68%) of the flame spray direct cost, as illustrated in Fig. 6.8. According to Eq. (64), the deposition efficiency Y is the characteristic parameter of the flame spray process that influences the powder costs for the FS SHM sensor. The deposition efficiency has a direct correlation with the physical parameters of powder spray deposition [65]. However, predictive models of the deposition efficiency based on flame spray process parameters have not been successful to date [65], which provide grounds to support experimental estimation methods for Y, such as the one presented in this study (Eq. (67)). According to Eq. (70), there is a negative correlation between the deposition efficiency and the gas flow rate, which is proportional to the gas cost, as per Eq. (68). Therefore, a compromise between the powder and gas cost components must be reached to minimize the joint cost contribution to the flame spray direct cost of the FS SHM sensor. However, considering the relatively low deposition efficiency (Y) value of 0.096 observed during the FS SHM sensor fabrication, improved flame spray economics may be realized if the Al-12Si deposition onto the FRPC can be enhanced without a significant increment in the gas costs, e.g., by optimization of the FRPC substrate roughness for Al-12Si particle adhesion.

The evaluation of the flame spray electricity costs provides a quantitative estimate of the maximum economic impact of the electrical equipment power consumption on the flame spray direct costs of the FS SHM sensor. As shown in Fig. 6.8, the flame spray electricity cost represents \$0.01 (0.02%) of the flame spray direct cost, which is considered negligible with respect to powder, gas, and labour costs of the FS SHM sensor. Therefore, the electricity costs of the HP-20 robot arm, 9MC, and 5MPE units can be neglected and a simplification of the flame spray cost model presented in Eq. (63) sans electrical costs may be used without a significant loss in overall accuracy.

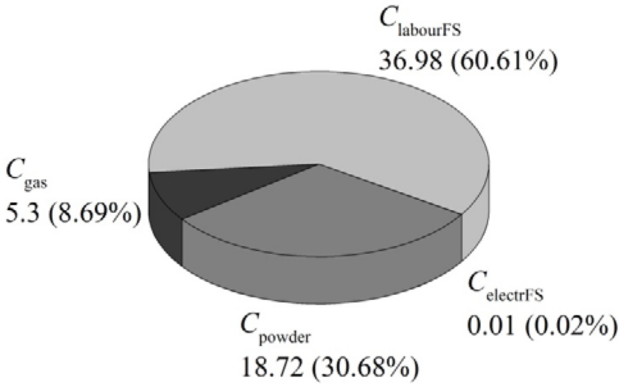

Figure 6.8: Distribution of the flame spray direct cost of the FS SHM sensor showing the flame spray labour (C_{labourFS}), powder (C_{powder}), gas (C_{gas}), and electrical (C_{electrFS}) cost components

Even though the flame spray direct costs of labour, powder, gas, and electricity constitute an important component of the ICC_{FS}, the complementary direct cost (C_{comp}) represents \$47.94 (17.53%) of the manufacturing direct costs of the FS SHM sensor, as shown in Fig.6.7. Based on the estimation of complementary direct cost presented in the Appendix A of this thesis document, it is noted that the material cost of 80-grit garnet sand ($0.0001) and the electrical cost of grit-blasting the aluminium tape contact ($0.008) [222] are not consequential, since the mass production regime that would make these costs significant is not contemplated as part of the scope of this work. Therefore, the material cost of 80-grit garnet sand and the electrical cost of grit-blasting the aluminium tape can be neglected. Excluding garnet sand and grit-blasting electricity costs, the distribution of the complementary direct cost of the FS SHM sensor is presented in Fig. 6.9. As shown in Figure 6.9, the combined cost of off-the-shelf materials and components (Wheatstone bridge, 170-10S red plasma masking tape, 3M 438 aluminium tape, DP-460 adhesive, flux, solder, and constantan wire) represents roughly 43% of the complementary direct costs of the FS SHM sensor, whereas labour costs constitute the remainder 57%. Although a careful selection of suppliers should be considered to reduce the purchase cost of off-the shelf materials and components of the FS SHM sensor, the complementary direct cost (C_{comp}) are dominated by external economic factors such as changes in supply prices and salary regulations, which are not the focus of this study.

In addition to initial capital costs, the annual operating costs of the FS and FBG SHM sensors are considered over the 20-year period of deployment. According to Eq. (59) and Eq. (60), the operating costs of the FS SHM sensor results in an annual electricity cost of $0.65 and an annual maintenance allowance of $8.20. The operating cost of the FBG SHM sensor is an annual electricity expense of $12.16. Considering the ICC and operating cost values, the characteristic cash flows (pre-tax) of the FS and FBG SHM sensors are presented in Fig. 6.10 and Fig. 6.11, respectively. The choice of an annual period for operating costs of the FS and FBG SHM sensors implies that operating cash flows are considered to occur at the end of each year, when in fact the operating expenses are incurred over the course of each year, i.e. monthly. However, the practical impact of the annual payment premise is typically small compared to the accuracy of the assumptions that generate the SHM sensor operating cash flow projections for the DCF analysis [212].

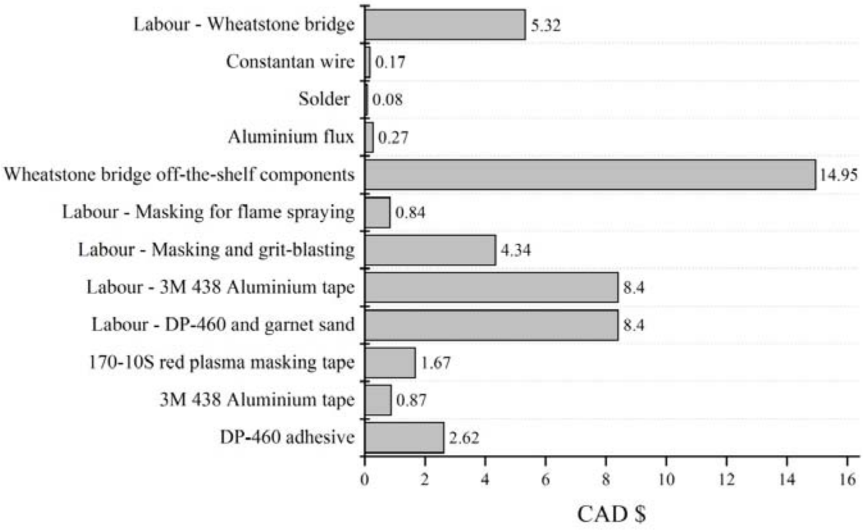

Figure 6.9: Distribution of the complementary direct cost of the FS SHM sensor

As evidenced in Fig. 6.10 and Fig. 6.11, the influence of CCA and tax rates on the characteristic cash flows (pre-tax) of the FS and FBG sensors results in a declining-balance in after-tax cash flows of the FS and FBG sensors after the first year of operation ($n > 1$). Since the FBG SHM sensor exhibits higher undepreciated capital cost (UCC) values compared to those of the FS SHM sensor, the F_n values of the FBG SHM sensor are positive from the end of year one ($n = 1$) until the end of ninth year ($n = 9$), whereas those of the FS SHM sensor are positive from the end of the first year ($n = 1$) until the end of the fourth year ($n = 4$).

Inflation is not considered in the calculation of the F_n cash flow values in Fig. 6.10 and Fig. 6.11. Instead, the annual effective real discount rate i includes the estimated inflationary effects, as per Eq. (79) [198]. Moreover, the inflation-free discount rate (i_{n}) values used in Eq. (79) can be considered as a measure of the Minimum Hurdle Rate of Return (MARR) for public and corporate capital investments [212]. Therefore, the annual effective real discount rate i includes both the minimum return expectation and the inflation effect in the estimation of the time value of money for the DCF analysis.

The discounted cash flow (DCF) results are presented in Fig. 6.12. The discounting of the after-tax cash flows F_n of the FS and FBG sensors is accomplished using Eq. (78) for the four investment options (combinations of SHM sensor after-tax cash flow and i) presented in Table 6.4. Each investment option yields a net present value (NPV), as per Eq. (80).

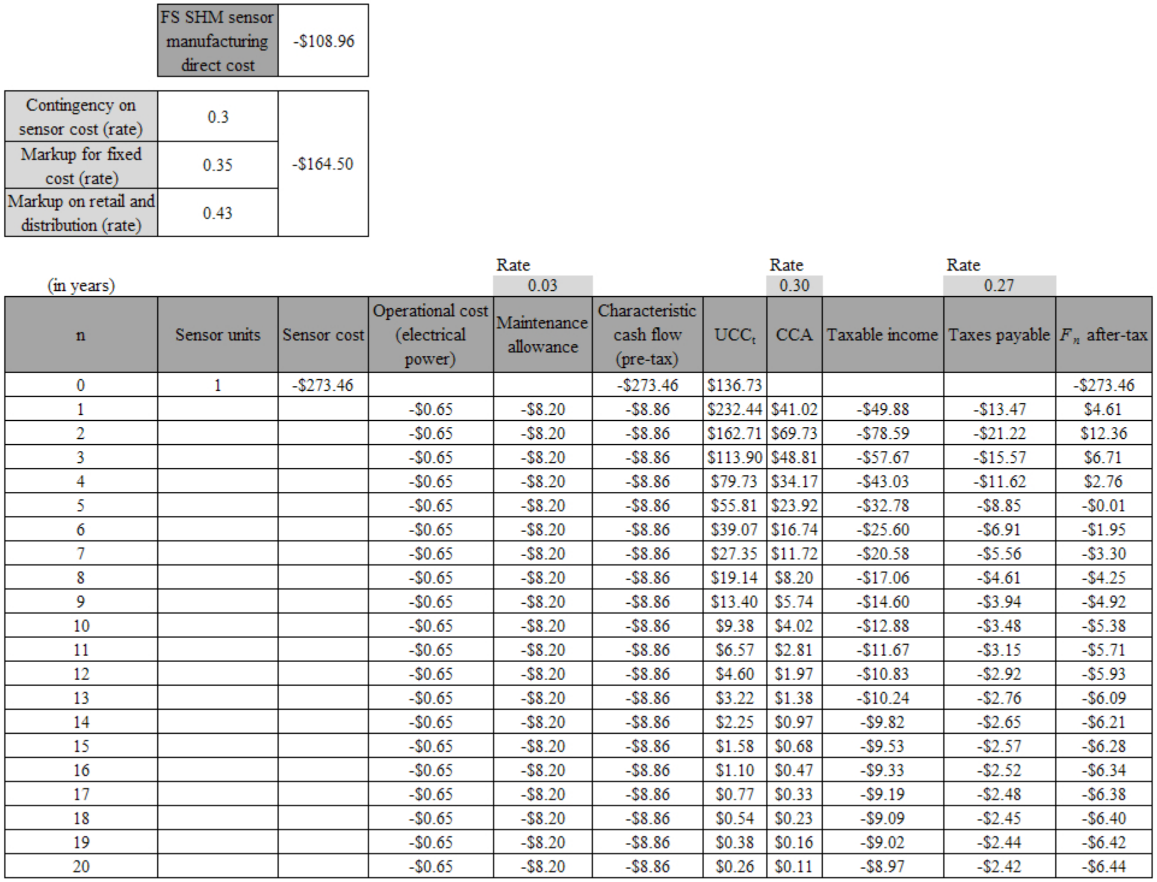

FS SHM sensor manufacturing direct cost	-$108.96

Contingency on sensor cost (rate)	0.3	-$164.50
Markup for fixed cost (rate)	0.35	
Markup on retail and distribution (rate)	0.43	

(in years)				Rate 0.03			Rate 0.30		Rate 0.27	
n	Sensor units	Sensor cost	Operational cost (electrical power)	Maintenance allowance	Characteristic cash flow (pre-tax)	UCC_t	CCA	Taxable income	Taxes payable	F_n after-tax
0	1	-$273.46			-$273.46	$136.73				-$273.46
1			-$0.65	-$8.20	-$8.86	$232.44	$41.02	-$49.88	-$13.47	$4.61
2			-$0.65	-$8.20	-$8.86	$162.71	$69.73	-$78.59	-$21.22	$12.36
3			-$0.65	-$8.20	-$8.86	$113.90	$48.81	-$57.67	-$15.57	$6.71
4			-$0.65	-$8.20	-$8.86	$79.73	$34.17	-$43.03	-$11.62	$2.76
5			-$0.65	-$8.20	-$8.86	$55.81	$23.92	-$32.78	-$8.85	-$0.01
6			-$0.65	-$8.20	-$8.86	$39.07	$16.74	-$25.60	-$6.91	-$1.95
7			-$0.65	-$8.20	-$8.86	$27.35	$11.72	-$20.58	-$5.56	-$3.30
8			-$0.65	-$8.20	-$8.86	$19.14	$8.20	-$17.06	-$4.61	-$4.25
9			-$0.65	-$8.20	-$8.86	$13.40	$5.74	-$14.60	-$3.94	-$4.92
10			-$0.65	-$8.20	-$8.86	$9.38	$4.02	-$12.88	-$3.48	-$5.38
11			-$0.65	-$8.20	-$8.86	$6.57	$2.81	-$11.67	-$3.15	-$5.71
12			-$0.65	-$8.20	-$8.86	$4.60	$1.97	-$10.83	-$2.92	-$5.93
13			-$0.65	-$8.20	-$8.86	$3.22	$1.38	-$10.24	-$2.76	-$6.09
14			-$0.65	-$8.20	-$8.86	$2.25	$0.97	-$9.82	-$2.65	-$6.21
15			-$0.65	-$8.20	-$8.86	$1.58	$0.68	-$9.53	-$2.57	-$6.28
16			-$0.65	-$8.20	-$8.86	$1.10	$0.47	-$9.33	-$2.52	-$6.34
17			-$0.65	-$8.20	-$8.86	$0.77	$0.33	-$9.19	-$2.48	-$6.38
18			-$0.65	-$8.20	-$8.86	$0.54	$0.23	-$9.09	-$2.45	-$6.40
19			-$0.65	-$8.20	-$8.86	$0.38	$0.16	-$9.02	-$2.44	-$6.42
20			-$0.65	-$8.20	-$8.86	$0.26	$0.11	-$8.97	-$2.42	-$6.44

Figure 6.10: Characteristic and after-tax cash flows of the FS SHM sensor

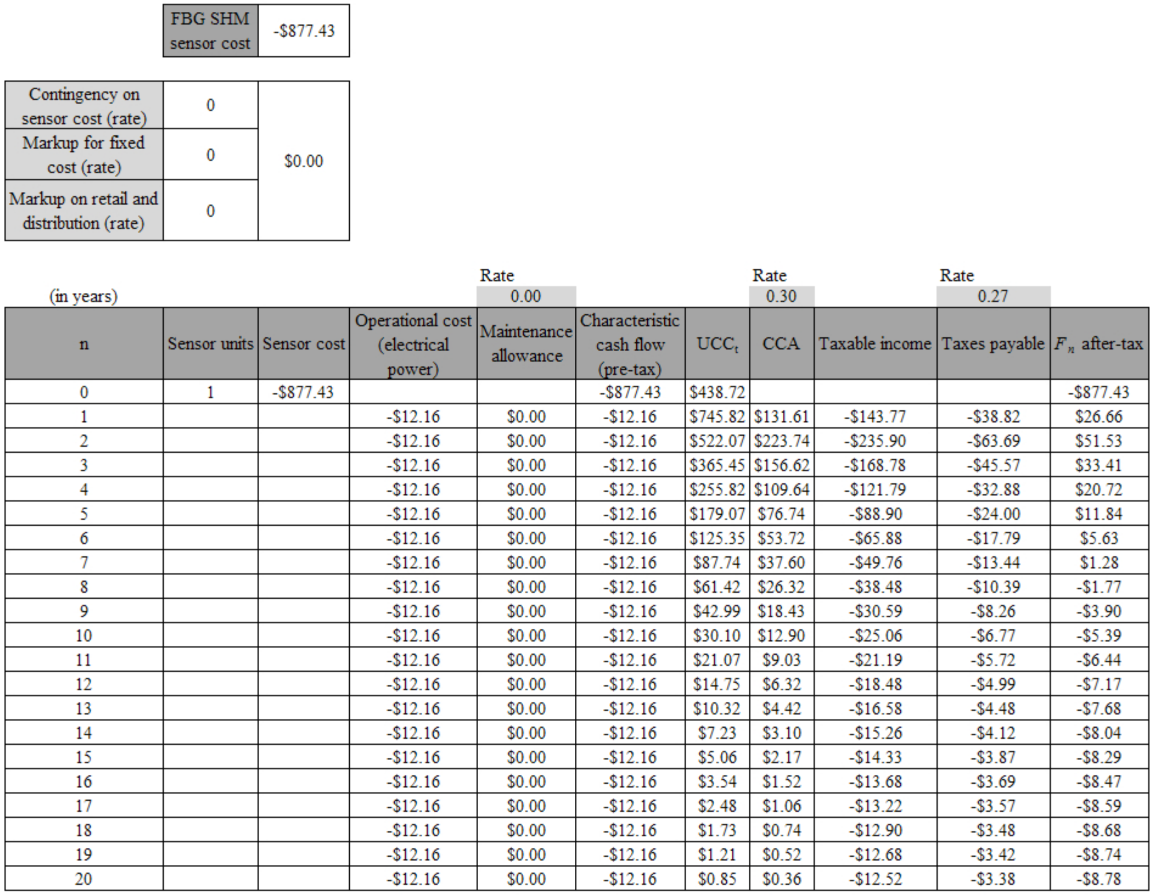

FBG SHM sensor cost	-$877.43

Contingency on sensor cost (rate)	0	$0.00
Markup for fixed cost (rate)	0	
Markup on retail and distribution (rate)	0	

				Rate			Rate		Rate	
(in years)				0.00			0.30		0.27	
n	Sensor units	Sensor cost	Operational cost (electrical power)	Maintenance allowance	Characteristic cash flow (pre-tax)	UCC_t	CCA	Taxable income	Taxes payable	F_n after-tax
0	1	-$877.43			-$877.43	$438.72				-$877.43
1			-$12.16	$0.00	-$12.16	$745.82	$131.61	-$143.77	-$38.82	$26.66
2			-$12.16	$0.00	-$12.16	$522.07	$223.74	-$235.90	-$63.69	$51.53
3			-$12.16	$0.00	-$12.16	$365.45	$156.62	-$168.78	-$45.57	$33.41
4			-$12.16	$0.00	-$12.16	$255.82	$109.64	-$121.79	-$32.88	$20.72
5			-$12.16	$0.00	-$12.16	$179.07	$76.74	-$88.90	-$24.00	$11.84
6			-$12.16	$0.00	-$12.16	$125.35	$53.72	-$65.88	-$17.79	$5.63
7			-$12.16	$0.00	-$12.16	$87.74	$37.60	-$49.76	-$13.44	$1.28
8			-$12.16	$0.00	-$12.16	$61.42	$26.32	-$38.48	-$10.39	-$1.77
9			-$12.16	$0.00	-$12.16	$42.99	$18.43	-$30.59	-$8.26	-$3.90
10			-$12.16	$0.00	-$12.16	$30.10	$12.90	-$25.06	-$6.77	-$5.39
11			-$12.16	$0.00	-$12.16	$21.07	$9.03	-$21.19	-$5.72	-$6.44
12			-$12.16	$0.00	-$12.16	$14.75	$6.32	-$18.48	-$4.99	-$7.17
13			-$12.16	$0.00	-$12.16	$10.32	$4.42	-$16.58	-$4.48	-$7.68
14			-$12.16	$0.00	-$12.16	$7.23	$3.10	-$15.26	-$4.12	-$8.04
15			-$12.16	$0.00	-$12.16	$5.06	$2.17	-$14.33	-$3.87	-$8.29
16			-$12.16	$0.00	-$12.16	$3.54	$1.52	-$13.68	-$3.69	-$8.47
17			-$12.16	$0.00	-$12.16	$2.48	$1.06	-$13.22	-$3.57	-$8.59
18			-$12.16	$0.00	-$12.16	$1.73	$0.74	-$12.90	-$3.48	-$8.68
19			-$12.16	$0.00	-$12.16	$1.21	$0.52	-$12.68	-$3.42	-$8.74
20			-$12.16	$0.00	-$12.16	$0.85	$0.36	-$12.52	-$3.38	-$8.78

Figure 6.11: Characteristic and after-tax cash flows (F_n) of the FBG SHM sensor

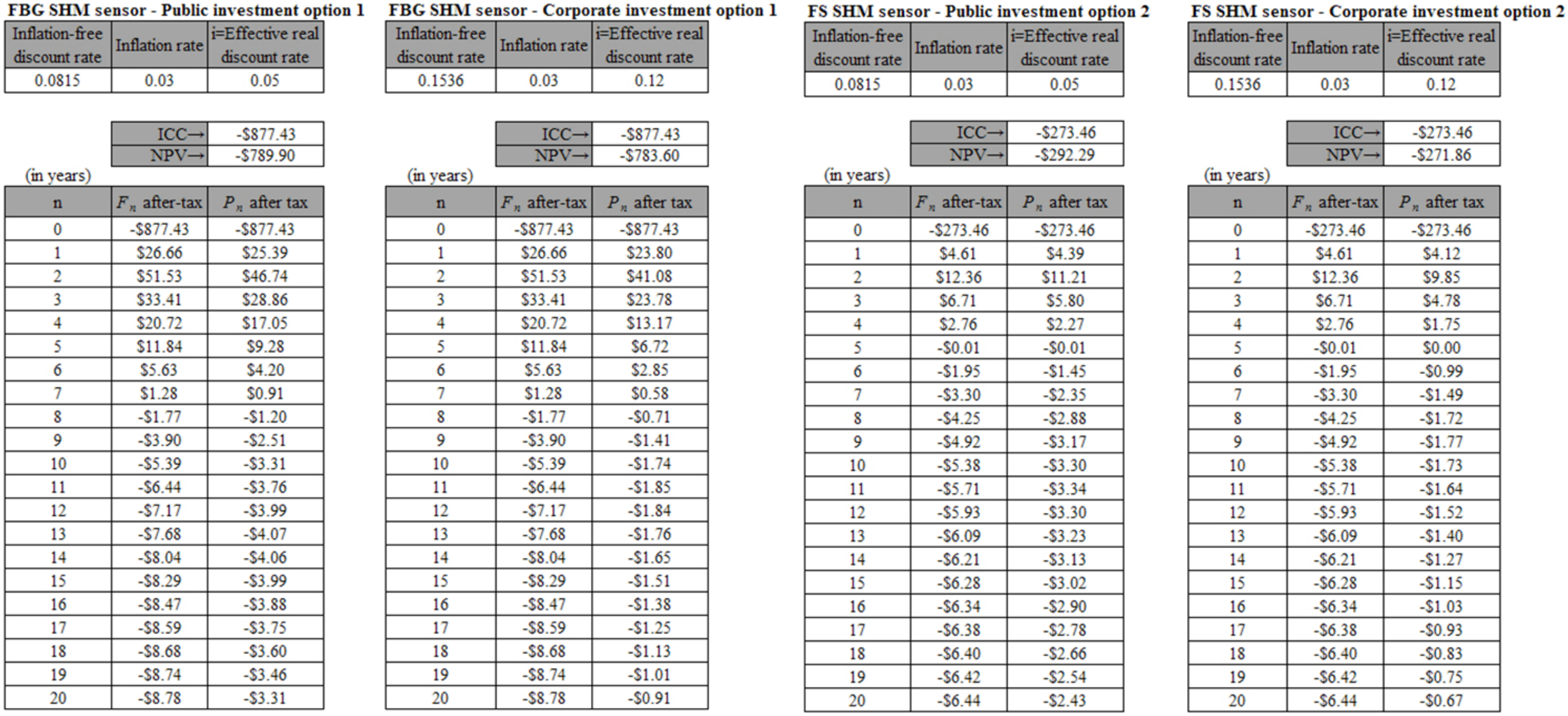

FBG SHM sensor - Public investment option 1

Inflation-free discount rate	Inflation rate	i=Effective real discount rate
0.0815	0.03	0.05

ICC→	-$877.43
NPV→	-$789.90

(in years)

n	F_n after-tax	P_n after tax
0	-$877.43	-$877.43
1	$26.66	$25.39
2	$51.53	$46.74
3	$33.41	$28.86
4	$20.72	$17.05
5	$11.84	$9.28
6	$5.63	$4.20
7	$1.28	$0.91
8	-$1.77	-$1.20
9	-$3.90	-$2.51
10	-$5.39	-$3.31
11	-$6.44	-$3.76
12	-$7.17	-$3.99
13	-$7.68	-$4.07
14	-$8.04	-$4.06
15	-$8.29	-$3.99
16	-$8.47	-$3.88
17	-$8.59	-$3.75
18	-$8.68	-$3.60
19	-$8.74	-$3.46
20	-$8.78	-$3.31

FBG SHM sensor - Corporate investment option 1

Inflation-free discount rate	Inflation rate	i=Effective real discount rate
0.1536	0.03	0.12

ICC→	-$877.43
NPV→	-$783.60

(in years)

n	F_n after-tax	P_n after tax
0	-$877.43	-$877.43
1	$26.66	$23.80
2	$51.53	$41.08
3	$33.41	$23.78
4	$20.72	$13.17
5	$11.84	$6.72
6	$5.63	$2.85
7	$1.28	$0.58
8	-$1.77	-$0.71
9	-$3.90	-$1.41
10	-$5.39	-$1.74
11	-$6.44	-$1.85
12	-$7.17	-$1.84
13	-$7.68	-$1.76
14	-$8.04	-$1.65
15	-$8.29	-$1.51
16	-$8.47	-$1.38
17	-$8.59	-$1.25
18	-$8.68	-$1.13
19	-$8.74	-$1.01
20	-$8.78	-$0.91

FS SHM sensor - Public investment option 2

Inflation-free discount rate	Inflation rate	i=Effective real discount rate
0.0815	0.03	0.05

ICC→	-$273.46
NPV→	-$292.29

(in years)

n	F_n after-tax	P_n after tax
0	-$273.46	-$273.46
1	$4.61	$4.39
2	$12.36	$11.21
3	$6.71	$5.80
4	$2.76	$2.27
5	-$0.01	-$0.01
6	-$1.95	-$1.45
7	-$3.30	-$2.35
8	-$4.25	-$2.88
9	-$4.92	-$3.17
10	-$5.38	-$3.30
11	-$5.71	-$3.34
12	-$5.93	-$3.30
13	-$6.09	-$3.23
14	-$6.21	-$3.13
15	-$6.28	-$3.02
16	-$6.34	-$2.90
17	-$6.38	-$2.78
18	-$6.40	-$2.66
19	-$6.42	-$2.54
20	-$6.44	-$2.43

FS SHM sensor - Corporate investment option 2

Inflation-free discount rate	Inflation rate	i=Effective real discount rate
0.1536	0.03	0.12

ICC→	-$273.46
NPV→	-$271.86

(in years)

n	F_n after-tax	P_n after tax
0	-$273.46	-$273.46
1	$4.61	$4.12
2	$12.36	$9.85
3	$6.71	$4.78
4	$2.76	$1.75
5	-$0.01	$0.00
6	-$1.95	-$0.99
7	-$3.30	-$1.49
8	-$4.25	-$1.72
9	-$4.92	-$1.77
10	-$5.38	-$1.73
11	-$5.71	-$1.64
12	-$5.93	-$1.52
13	-$6.09	-$1.40
14	-$6.21	-$1.27
15	-$6.28	-$1.15
16	-$6.34	-$1.03
17	-$6.38	-$0.93
18	-$6.40	-$0.83
19	-$6.42	-$0.75
20	-$6.44	-$0.67

Figure 6.12: Initial capital cost (ICC), after-tax cash flows (F_n), discounted cash flows (P_n), and net present value (NPV) of each investment option for the FS and FBG SHM sensors

The NPV represents a valuation of the financial performance of the SHM sensor after-tax cash flows based on the annual effective real discount rate *i*. Based on financial theory, the optimal choice of mutually exclusive investment alternatives is the one yielding the highest NPV [198, 212]. In addition, the NPV is often the preferred financial indicator for investments that do not have revenue (positive) stream in the cash flows [212], which is consistent with the present economic analysis of the FS and FBG SHM sensors.

As shown in Fig 6.12, NPV values are -\$789.90 ($i = 5\%$) and -\$783.60 ($I = 12\%$) for the FBG SHM sensor, whereas the FS SHM sensor exhibit NPV values of -\$292.29 ($i = 5\%$) and -\$271.86 ($i = 12\%$). Considering the investment options shown in Table 6.4, a negative NPV indicates that the given investment option does not achieve the rate of return given by *i*. The fact that all NPVs are negative in Fig 6.12 is expected since the characteristic cash flows of the FS and FBG SHM sensors represent capital and operational costs (negative cash flow values) and do not contemplate the full economic impact of the SHM sensor, which requires an assessment of the risk, quality, potential operational benefits, and cost saving factors. Therefore, the NPV values in this study do not represent the economic value of the FS and FBG SHM sensors in absolute dollar terms for the end user, but only the value in terms of SHM sensor direct costs.

In this context, however, the NPV values provide an indicator of the cost efficiency of the FS and FBG SHM sensors that is independent from the functional SHM effectiveness. However, the net present values presented in Fig. 6.12 can be used as a benchmark to compare the cost performance of the FS and FBG SHM sensors. The comparative analysis of the cost-efficiency versus the required investment of the FS and FBG SHM sensors is accomplished by pairing the NPV and *ICC* results for each investment option shown in Table 6.4, which is shown in Fig. 6.12 and Fig. 6.13.

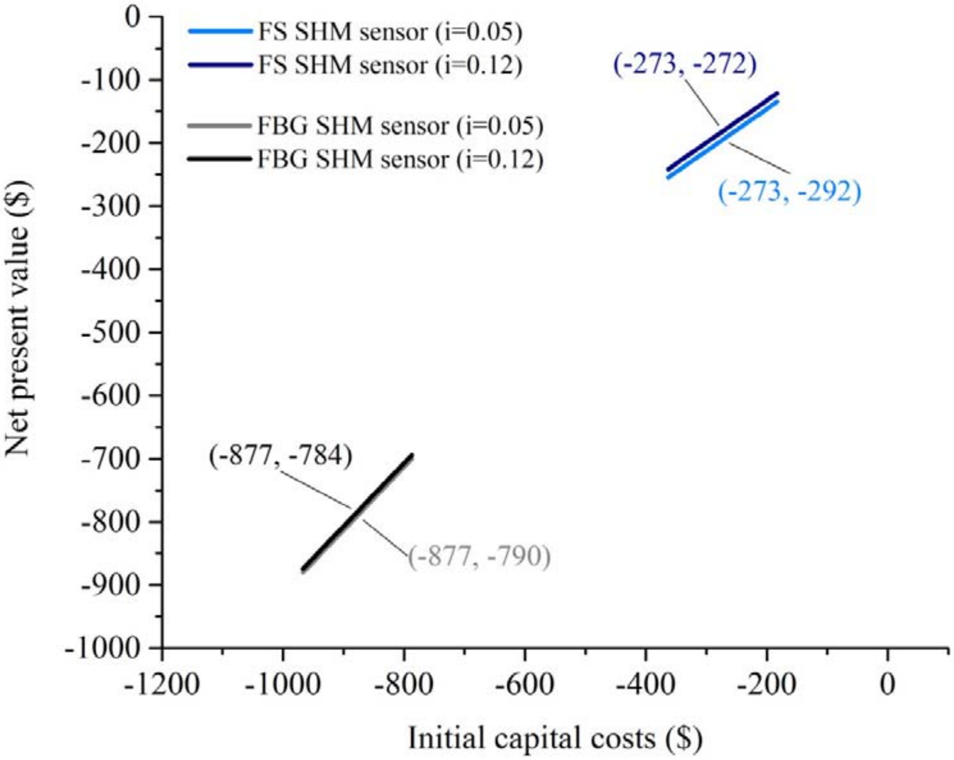

Figure 6.13: Relationship between the initial capital costs and net present values of the FS and FBG SHM sensors using the values of the annual effective real discount rate (*i*)

In Fig. 6.13, the label points represent the ICC-NPV pairs for the four investment options. The sensitivity of the NPV to changes in the ICC values is represented by the line segments, which are centered at the label point value of each investment option. As shown in Fig. 6.13, changes in the annual effective real discount rate (i) produce modest changes in the NPV of the FS and FBG SHM sensors. Therefore, the net present values of the FS and FBG SHM sensors are considered insensitive to the discount rate. This is explained by the distribution of the characteristic cash flows of the FS and FBG SHM sensors over time, which is overwhelmingly laden at $t = 0$ (front-loaded), as shown in Fig. 6.10 and Fig. 6.11. Therefore, the relative high value of ICC dominates the calculation of the NPV in Eq. (80). Furthermore, if the characteristic cash flow values of the FBG SHM sensor for $n > 0$ remain fixed, ICC_{FBG} values of -\$234.66 and -\$251.45 are required in order to produce the same net present values of the FS SHM sensor at $i = 0.05$ and $i = 0.12$.

Based on the ICC and NPV of the FS and FBG SHM sensors presented in Fig. 6.13, the FS SHM sensor possess the lowest ICC and the highest NPV for both $i = 0.05$ (public investment option) and $i = 0.12$ (corporate investment option). Therefore, the FS SHM sensor exhibits better cost economics with respect to the FBG SHM sensor, which can provide additional grounds for research and technical development of the FS SHM sensor in order to realize the potential financial benefits of such implementation in FRPC structures.

6.4 Conclusions

This study evaluated the financial performance of the FS and FBG SHM sensors for FRPC structures based on end user capital and operational costs. A model of the flame spray direct costs was developed to determine the contribution of powder, gas, labour, and electricity costs in the ICC of the FS SHM sensor. The structure of the incremental ICC of the FS and FBG SHM sensors was analyzed and a lower initial cost was estimated for the FS SHM sensor.

A DCF analysis of the after-tax cash flows of the FS and FBG SHM sensors was performed using public and corporate annual effective real discount rates over a 20-year project horizon. The results of the DCF analysis show that the characteristic cash flows of the FS and FBG SHM sensors are predominantly front-loaded. Therefore, the ICC is the most important significant factor on the determination of the NPV of the FS and FBG SHM sensors. The FS SHM sensor exhibits better cost efficiency in terms of lower ICC and higher NPV compared to the FBG SHM sensor for public and corporate effective real discount rates, respectively. The advantageous cost economics of the FS SHM sensor can contribute to the assessment of the potential financial benefits of the implementation in FRPC structures.

Chapter 7 Conclusions and recommendations

7.1 Findings and contributions

The development and characterization of a damage detection SHM sensor based on flame-sprayed Al-12Si coatings onto FRPC structures was performed as part of this research project. The literature review in Chapter 2 on the thermal spray metal deposition onto FRPC substrates showed that research conducted on functional thermal spray coatings is limited with regards to the deposition of electrically conductive coatings onto FRPC substrates. Moreover, the current investigation on damage detection SHM sensing in FRPC materials contributes to the research of the electromechanical behaviour of flame sprayed coatings, and expands the body of knowledge on potential applications for thermal spray metalized FRPC structures.

The mechanical effect of flame spray deposition of Al-12Si coatings on FRPC structures was evaluated in terms of the fluid containment performance in FRPC tubes and stiffness response for FRPC laminates. Coated FRPC tubes exhibited slightly higher mean leakage and burst pressures than those of the uncoated specimens and *t*-test results provided statistical evidence that the flame spray process can be performed without inducing damage in FRPC structures covered with garnet sand. Moreover, the applicability of the classical laminate theory model to describe the elastic behaviour of coated FRPC laminates under tension was validated considering the flame sprayed Al-12Si coating as an isotropic lamina, which included in the experimental determination of the effective Young's modulus and Poisson ratio of the porous flame sprayed Al-12Si coating.

A damage detection framework for coated FRPC laminates was developed to provide a description of the electrical resistance change in the porous Al-12Si coating under applied axial strain and evaluate the potential to perform damage detection in FRPC structures. The presented mathematical framework was capable of describing the evolution of the relative change in electrical resistance of the Al-12Si coating under applied axial strain, albeit significant experimental variability. The suitability of flame-spray Al-12Si coating for detecting strain induced damage was found to be limited to the late stages of failure, where fibre breakage and delamination affect the integrity of the FRPC structure.

In addition, a comparative economic analysis of the developed flame-sprayed SHM sensor was conducted to ascertain the distribution of capital and operational direct costs with respect to an industry-grade Fibre Bragg Grating SHM sensor, using the Net Present Value methodology over a 20-year project period. The cost structure of the flame-sprayed SHM sensor was dominated by initial capital costs, and exhibited advantageous economics with respect to Fibre Bragg Grating SHM sensor, which can provide grounds for research and technical development to realize potential financial benefits in FRPC structures.

7.2 Proposed future work

The work conducted in this research project has made valuable contributions in the field of FRPC thermal spray metallization. At the same time, the work identifies opportunities for future studies to improve and expand upon current findings. Proposed areas of future work are as follows:

- Knowledge of the temperature distribution within the FRPC substrate during the flame spray deposition process can facilitate the sensitivity analysis to process parameter and prevent mechanical degradation of the coated FRPC structure. As shown in Chapter 2, limited studies have focused on the temperature distribution within the substrate during the flame spray process. Potential enhancements in mechanical model predictions may be achieved by incorporating the thermal load effects of flame spray deposition on the mechanical properties of as-sprayed FRPC substrates.

- Further characterization of the effect of the microstructural porosity and morphology on the electrical properties of flame sprayed coatings needs to be undertaken to define suitable damage detection criteria at low strain levels that can be implemented in damage detection SHM sensors for FRPC structures. Moreover, the examination of the mechanisms of strain-induced porosity at the microscopic level is considered as an interesting extension to the present work, which can contribute to the development of flame-sprayed coatings with tailored electrical properties for FRPC substrates.

Bibliography

1. Why Multiscale? Thermal interactions. Firehole Technologies. Available at: http://i.ytimg.com/vi/fagaC94idjY/maxresdefault.jpg. 2009. Last accessed: Aug 21, 2015.

2. H. GangaRao, Applied Plastics Engineering Handbook, William Andrew Publishing, Oxford, England, United Kingdom, 2011, pp. 565-584.

3. L. Böger, M.H.G. Wichmann, L.O. Meyer, K. Schulte, Load and health monitoring in glass fibre-reinforced composites with an electrically conductive nanocomposite epoxy matrix, Composites Science and Technology 68 (7–8) (2008) 1886-1894.

4. L. Ainsworth, Fibre-reinforced plastic pipes and applications, Composites 12 (3) (1981) 185-190.

5. P. Mertiny, K. Juss, T. Bell, Corrosion and erosion resistant polymer composite pipe for oil sands hydrotransport, in: NACE - International Corrosion Conference Series, New Orleans, LO, United States, 2008, pp. 086671-086678.

6. L.L. Parent, D.Y. Li, Wear of hydrotransport lines in Athabasca oil sands, Wear 301 (1–2) (2013) 477-482.

7. Y. Yang, Y.F. Cheng, Parametric effects on the erosion–corrosion rate and mechanism of carbon steel pipes in oil sands slurry, Wear 276–277 (0) (2012) 141-148.

8. D. Fox, Market for FRP grows in the power industry, Reinforced Plastics 52 (9) (2008) 40-43.

9. J.D. Achenbach, Structural health monitoring – What is the prescription?, Mechanics Research Communications 36 (2) (2009) 137-142.

10. F.L. Matthews, R.D. Rawlings, Composite materials: Engineering and science, Chapman & Hall, London, NY, United States, 1994, pp. 223-245.

11. D. Richard, T. Hong, M. Hastak, A. Mirmiran, O. Salem, Life-cycle performance model for composites in construction, Composites Part B: Engineering 38 (2) (2007) 236-246.

12. R.A. Smith, Materials Science and Engineering (Vol. III), EOLSS Publishers Company Limited, Oxford, England, United Kingdom, 2009, pp. 103-143.

13. A.E. Kouche, H.S. Hassanein, Ultrasonic Non-Destructive Testing (NDT) Using Wireless Sensor Networks, Procedia Computer Science 10 (0) (2012) 136-143.

14. A.G. Smith, Non-destructive testing in industry aviation, Non-Destructive Testing 5 (3) (1972) 170-174.

15. A. Todoroki, K. Omagari, Y. Shimamura, H. Kobayashi, Matrix crack detection of CFRP using electrical resistance change with integrated surface probes, Composites Science and Technology 66 (11–12) (2006) 1539-1545.

16. M.H.G. Wichmann, J. Sumfleth, F.H. Gojny, M. Quaresimin, B. Fiedler, K. Schulte, Glass-fibre-reinforced composites with enhanced mechanical and electrical properties – Benefits and limitations of a nanoparticle modified matrix, Engineering Fracture Mechanics 73 (16) (2006) 2346-2359.

17. F. Robitaille, M. Yandouzi, S. Hind, B. Jodoin, Metallic coating of aerospace carbon/epoxy composites by the pulsed gas dynamic spraying process, Surface and Coatings Technology 203 (19) (2009) 2954-2960.

18. B. Rooks, Robot spraying of helicopter rotor blade ice protection system, Industrial Robot 28 (4) (2001) 313-315.

19. N. Huonnic, M. Abdelghani, P. Mertiny, A. McDonald, Deposition and characterization of flame-sprayed aluminum on cured glass and basalt fiber-reinforced epoxy tubes, Surface and Coatings Technology 205 (3) (2010) 867-873.

20. J. Voyer, P. Schulz, M. Schreiber, Electrically conductive flame sprayed aluminum coatings on textile substrates, in: International Thermal Spray Conference 2008, Maastricht, Limburg, Netherlands, 2008, pp. 818-823.

21. A. Ganesan, J. Affi, M. Yamada, M. Fukumoto, Bonding behavior studies of cold sprayed copper coating on the PVC polymer substrate, Surface and Coatings Technology 207(2012) 262-269.

22. A.G. McDonald, Visualization and Analysis of the Impact of Plasma-sprayed Particles, University of Toronto, 2007. Dissertation.

23. T.C. Totemeier, R.N. Wright, W.D. Swank, Residual stresses in high-velocity oxy-fuel metallic coatings, Metallurgical and Materials Transactions A: Physical Metallurgy and Materials Science 35 A (6) (2004) 1807-1814.

24. R. Li, L. Ye, Y. Mai, Application of plasma technologies in fibre-reinforced polymer composites: a review of recent developments, Composites Part A: Applied Science and Manufacturing 28 (1) (1997) 73-86.

25. S. Guanhong, H. Xiaodong, J. Jiuxing, S. Yue, Parametric study of Al and Al2O3 ceramic coatings deposited by air plasma spray onto polymer substrate, Applied Surface Science 257 (17) (2011) 7864-7870.

26. J.R. Davis, Handbook of Thermal Spray Technology, ASM International, Materials Park, OH, United States, 2004, pp. 1-36.

27. J. Sloan, 787 integrates new composite wing deicing system, High Performance Composites 17 (1) (2009) 27.

28. R. Gonzalez, P. Mertiny, A.G. McDonald, Effect of flame-sprayed Al-12Si coatings on the leakage of pressurized fiber-reinforced pipes, in: Proceedings

of the 24th Canadian Congress of Applied Mechanics, Saskatoon, SK, Canada, 2013, pp. DM-29-DM-32.

29. C. Katsoulis, B.K. Kandola, P. Myler, E. Kandare, Post-fire flexural performance of epoxy-nanocomposite matrix glass fibre composites containing conventional flame retardants, Composites Part A: Applied Science and Manufacturing 43 (8) (2012) 1389-1399.

30. P. Fauchais, A. Vardelle, Heat, mass and momentum transfer in coating formation by plasma spraying, International Journal of Thermal Sciences 39 (9–11) (2000) 852-870.

31. P. Fauchais, G. Montavon, Thermal and cold spray: Recent developments, Key Engineering Materials 384(2008) 1-59.

32. R.W. Smith, R. Knight, Thermal spraying I: powder consolidation - from coating to forming, The Journal of The Minerals, Metals & Materials Society 47 (8) (1995) 32-39.

33. A. McDonald, M. Lamontagne, C. Moreau, S. Chandra, Impact of plasma-sprayed metal particles on hot and cold glass surfaces, Thin Solid Films 514 (1-2) (2006) 212-222.

34. M.P. Dewar, A.G. McDonald, A.P. Gerlich, Interfacial heating during low-pressure cold-gas dynamic spraying of aluminum coatings, Journal of Materials Science 47 (1) (2012) 184-198.

35. T. Schmidt, F. Gartner, H. Assadi, H. Kreye, Development of a generalized parameter window for cold spray deposition, Acta Materialia 54 (3) (2006) 729-742.

36. P. Fauchais, M. Fukumoto, A. Vardelle, M. Vardelle, Knowledge concerning splat formation: An invited review, Journal of Thermal Spray Technology 13 (3) (2004) 337-360.

37. A. Moridi, S. Hassani-Gangaraj, M. Guagliano, M. Dao, Cold spray coating: Review of material systems and future perspectives, Surface Engineering 30 (6) (2014) 369-395.

38. T. Goyal, R.S. Walia, T.S. Sidhu, S. Samir, A review of coating technology processes and recent advancements, in: National Conference on Advances in Manufacturing Technology 2012, Chandigarh, India, 2012, pp. II -1-II -5.

39. D.S. Therrien, A.G. McDonald, P. Mertiny, Temperature measurements of polymer composite flat plates coated with aluminum-12silicon, in: International Thermal Spray Conference 2012, Houston, TX, USA, 2012, pp. 1-6.

40. F.N. Longo, Industrial guide - markets, materials, and applications for thermal-sprayed coatings, Journal of Thermal Spray Technology 1 (2) (1992) 143-145.

41. R. Gonzalez, A. McDonald, P. Mertiny, Effect of flame-sprayed Al-12Si coatings on the failure behaviour of pressurized fibre-reinforced composite tubes, Polymer Testing 32 (8) (2013) 1522-1528.

42. D.S. Therrien, Heat Transfer Analysis of Flame-sprayed Metal-polymer Composite Structures, University of Alberta, 2013. Dissertation.

43. H. Ashrafizadeh, P. Mertiny, A. McDonald, Determination of temperature distribution within polyurethane substrates during deposition of flame-sprayed aluminum-12silicon coatings using Green's function modeling and experiments, Surface and Coatings Technology 259(2014) 625-636.

44. X.L. Zhou, A.F. Chen, J.C. Liu, X.K. Wu, J.S. Zhang, Preparation of metallic coatings on polymer matrix composites by cold spray, Surface and Coatings Technology 206 (1) (2011) 132-136.

45. W. Huang, X. Fan, Y. Zhao, X. Zhou, X. Meng, Y. Wang, B. Zou, X. Cao, Z. Wang, Fabrication of thermal barrier coatings onto polyimide matrix composites via air plasma spray process, Surface and Coatings Technology 207(2012) 421-429.

46. M.J. Vucko, P.C. King, A.J. Poole, C. Carl, M.Z. Jahedi, R. de Nys, Cold spray metal embedment: an innovative antifouling technology, Biofouling 28 (3) (2012) 239-248.

47. D. Giraud, F. Borit, V. Guipont, M. Jeandin, J.M. Malhaire, Metallization of a polymer using cold spray: Application to aluminum coating of polyamide 66,

in: International Thermal Spray Conference 2012, Houston, TX, USA, 2012, pp. 265-270.

48. M. Gardon, A. Latorre, M. Torrell, S. Dosta, J. Fernandez, J.M. Guilemany, Cold gas spray titanium coatings onto a biocompatible polymer, Materials Letters 106(2013) 97-99.

49. H. Ye, J. Wang, Preparation of aluminum coating on Lexan by cold spray, Materials Letters 137(2014) 21-24.

50. H. Ashrafizadeh, P. Mertiny, A. McDonald, Evaluation of the Influence of Flame Spraying Parameters on Microstructure and Electrical Conductivity of Al-12Si Coatings Deposited on Polyurethane Substrates, in: International Thermal Spray Conference 2015, Long Beach, CA, USA, 2015, pp. 370-376.

51. J.H. Koo, B. Muskopf, G. McCord, P. Van Dine, B. Spencer, U. Sorathia, S. Venumbaka, Characterization of fire safe polymer matrix composites for naval applications, in: International SAMPE Symposium and Exhibition, San Marcos, TX, USA, 2001, pp. 2170-2182.

52. R.N. Walters, Fire-safe polymer composites, in: International SAMPE Symposium and Exhibition, Long Beach, CA, USA, 2002, pp. 716-727.

53. S. Sampath, Opportunities for thermal spray in functional materials, electronics, and sensors, Advanced Materials and Processes 171 (11) (2013) 69-70.

54. J. Voyer, P. Schulz, M. Schreiber, Conducting flame-sprayed Al coatings on textile fabrics, Journal of Thermal Spray Technology 17 (4) (2008) 583-588.

55. An Introduction to Thermal Spray. Oerlikon Metco. Available at: http://www.oerlikon.com/ecomaXL/files/metco/oerlikon_Thermal_Spray_Brochure_EN5.pdf. 2014. Last accessed: Jun 1, 2015.

56. P.C. King, A.J. Poole, S. Horne, R. de Nys, S. Gulizia, M.Z. Jahedi, Embedment of copper particles into polymers by cold spray, Surface and Coatings Technology 216(2013) 60-67.

57. M.J. Vucko, P.C. King, A.J. Poole, M.Z. Jahedi, R. de Nys, Polyurethane seismic streamer skins: an application of cold spray metal embedment, Biofouling 29 (1) (2013) 1-9.

58. A.S.M. Ang, C.C. Berndt, A review of testing methods for thermal spray coatings, International Materials Reviews 59 (4) (2014) 179-223.

59. R. Lupoi, W. O'Neill, Deposition of metallic coatings on polymer surfaces using cold spray, Surface and Coatings Technology 205 (7) (2010) 2167-2173.

60. J. Affi, H. Okazaki, M. Yamada, M. Fukumoto, Fabrication of aluminum coating onto CFRP substrate by cold spray, Materials Transactions 52 (9) (2011) 1759-1763.

61. A. Sturgeon, B. Dunn, S. Celotto, B. O'Neill, Cold sprayed coatings for polymer composite substrates, in: 10th International Symposium on Materials in a Space Environment and The 8th International Conference on Protection of Materials and Structures in a Space Environment, Collioure, Languedoc-Roussillon, France, 2006, pp. 616-1-616-6.

62. R. Ely, L.R. Centolanza, Demonstration of rotor blades with increased environmental durability, in: 67th American Helicopter Society International Annual Forum 2011, Virginia Beach, VA, USA, 2011, pp. 1880-1893.

63. M. Fukumoto, H. Terada, M. Mashiko, K. Sato, M. Yamada, E. Yamaguchi, Deposition of copper fine particle by cold spray process, Materials Transactions 50 (6) (2009) 1482-1488.

64. M. Vijay, V. Selvarajan, S. Yugeswaran, P.V. Ananthapadmanabhan, K.P. Sreekumar, Effect of spraying parameters on deposition efficiency and wear behavior of plasma sprayed alumina-titania composite coatings, Plasma Science and Technology 11 (6) (2009) 666-673.

65. O. Stier, Fundamental cost analysis of cold spray, in: 2013 International Thermal Spray Conference, Busan, Yeongnam, South Korea, 2014, pp. 131-139.

66. B. Jodoin, P. Richer, G. Berube, L. Ajdelsztajn, A. Erdi-Betchi, M. Yandouzi, Pulsed-Gas Dynamic Spraying: Process analysis, development and selected

coating examples, Surface and Coatings Technology 201 (16-17) (2007) 7544-7551.

67. G.M. Nelson, J.A. Nychka, A.G. McDonald, Structure, phases, and mechanical response of Ti-alloy bioactive glass composite coatings, Materials Science and Engineering C 36 (1) (2014) 261-276.

68. H. Boyer, A. McDonald, P. Mertiny, Flame spray deposition of electrically conductive traces on polymer substrates for system integrated composite structures, in: Composites 2012, Las Vegas, NV, USA, 2012, pp. 1-6.

69. M.H.A. Malek, N.H. Saad, S.K. Abas, N.M. Shah, Thermal arc spray overview, in: 2013 International Conference on Manufacturing, Optimization, Industrial and Material Engineering, Bandung, West Java, Indonesia, 2013, pp. 012028-1-012028-11.

70. X. Wang, J. Heberlein, E. Pfender, W. Gerberich, Effect of nozzle configuration, gas pressure, and gas type on coating properties in wire arc spray, Journal of Thermal Spray Technology 8 (4) (1999) 565-575.

71. A. Liu, M. Guo, M. Zhao, H. Ma, S. Hu, Arc sprayed erosion-resistant coating for carbon fiber reinforced polymer matrix composite substrates, Surface and Coatings Technology 200 (9) (2006) 3073-3077.

72. A. Liu, M. Guo, J. Gao, M. Zhao, Influence of bond coat on shear adhesion strength of erosion and thermal resistant coating for carbon fiber reinforced

thermosetting polyimide, Surface and Coatings Technology 201 (6) (2006) 2696-2700.

73. E. Lugscheider, T. Weber, Plasma spraying--An innovative coating technique: Process variants and applications, IEEE Transactions on Plasma Science 18 (6) (1990) 968-973.

74. A. Ganesan, M. Yamada, M. Fukumoto, The effect of CFRP surface treatment on the splat morphology and coating adhesion strength, in: International Thermal Spray Conference 2013, Busan, Yeongnam, South Korea, 2014, pp. 236-244.

75. R. Beydon, G. Bernhart, Y. Segui, Measurement of metallic coatings adhesion to fibre-reinforced plastic materials, Surface and Coatings Technology 126 (1) (2000) 39-47.

76. M. Mellali, P. Fauchais, A. Grimaud, Influence of substrate roughness and temperature on the adhesion/cohesion of alumina coatings, Surface and Coatings Technology 81 (2-3) (1996) 275-286.

77. A. Lopera-Valle, A. McDonald, Use of Flame-sprayed Coatings as Heating Elements for Polymer-Based Composite Structures, in: International Thermal Spray Conference 2015, Long Beach, CA, USA, 2015, pp. 1183-1190.

78. A. Lopera-Valle, A. McDonald, Application of Flame-sprayed Coatings as Heating Elements for Polymer-Based Composite Structures, Journal of

Thermal Spray Technology (under review (Manuscript ID: JTST-15-03-2284)) .

79. H. Ashrafizadeh, A. McDonald, P. Mertiny, Deposition of Electrically Conductive Coatings on Castable Polyurethane Elastomers by the Flame Spraying Process, Journal of Thermal Spray Technology (under review (Manuscript ID: JTST-15-04-2296)) .

80. L. PawŁowski, Temperature distribution in plasma-sprayed coatings, Thin Solid Films 81 (1) (1981) 79-88.

81. M. Floristan, R. Fontarnau, A. Killinger, R. Gadow, Development of electrically conductive plasma sprayed coatings on glass ceramic substrates, Surface and Coatings Technology 205 (4) (2010) 1021-1028.

82. A. Ganesan, M. Yamada, M. Fukumoto, Cold spray coating deposition mechanism on the thermoplastic and thermosetting polymer substrates, Journal of Thermal Spray Technology 22 (8) (2013) 1275-1282.

83. R. Gonzalez, A.G. McDonald, P. Mertiny, Damage detection method for fiber-reinforced polymer composites using Al-12Si flame-sprayed coatings, in: SAMPE Seattle 2014 Conference, Seattle, WA, USA, 2014, pp. 4056 -1-4056 -11.

84. M. Fasching, F.B. Prinz, L.E. Weiss, 'Smart' coatings: a technical note, Journal of Thermal Spray Technology 4 (2) (1995) 133-136.

85. M. Prudenziati, M.L. Gualtieri, Electrical properties of thermally sprayed Ni- and Ni20Cr-based resistors, Journal of Thermal Spray Technology 17 (3) (2008) 385-394.

86. S. Sampath, H. Herman, A. Patel, R. Gambino, R. Greenlaw, E. Tormey, Thermal spray techniques for fabrication of meso-electronics and sensors, in: Materials Development for Direct Write Technologies, April 24, 2000 - April 26, 2000, pp. 181-188.

87. A. Sharma, R.J. Gambino, S. Sampath, Electrical conduction in thermally sprayed thin metallic coatings, in: 2005 Materials Research Society Fall Meeting, 2006, pp. 287-292.

88. N. Margadant, S. Siegmann, J. Patscheider, T. Keller, W. Wagner, J. Ilavsky, J. Pisacka, G. Barbezat, P.S. Fiala, Microstructure - property relationships and cross-property-correlations of thermal sprayed ni-alloy coatings, in: International Thermal Spray Conference 2001, Singapore, Singapore, 2001, pp. 643-652.

89. A. Sharma, R.J. Gambino, S. Sampath, Anisotropic electrical properties in thermal spray metallic coatings, Acta Materialia 54 (1) (2006) 59-65.

90. N. Bheekhun, A.R. Abu Talib, M.R. Hassan, Thermal Spray Coatings for Polymer Matrix Composites in Gas Turbine Engines: A Literary Preview, International Review of Aerospace Engineering 7 (3) (2014) 84-87.

91. M. Grujicic, V. Sellappan, G. Arakere, N. Seyr, M. Erdmann, Computational feasibility analysis of direct-adhesion polymer-to-metal hybrid technology for load-bearing body-in-white structural components, Journal of Materials Processing Technology 195 (1–3) (2008) 282-298.

92. K. Patel, C.S. Doyle, D. Yonekura, B.J. James, Effect of surface roughness parameters on thermally sprayed PEEK coatings, Surface and Coatings Technology 204 (21–22) (2010) 3567-3572.

93. P. Mertiny, F. Ellyin, Influence of the filament winding tension on physical and mechanical properties of reinforced composites, Composites Part A: Applied Science and Manufacturing 33 (12) (2002) 1615-1622.

94. P. Mertiny, K. Juss, M.M. El Ghareeb, Evaluation of glass and basalt fiber reinforcements for polymer composite pressure piping, Journal of Pressure Vessel Technology, Transactions of the ASME 131 (6) (2009) 0614071-0614076.

95. K.D. Cowley, P.W.R. Beaumont, Damage accumulation at notches and the fracture stress of carbon-fibre/polymer composites: Combined effects of stress and temperature, Composites Science and Technology 57 (9–10) (1997) 1211-1219.

96. R.R. Chang, Experimental and theoretical analyses of first-ply failure of laminated composite pressure vessels, Composite Structures 49 (2) (2000) 237-243.

97. P. Mertiny, A. Gold, Quantification of leakage damage in high-pressure fibre-reinforced polymer composite tubular vessels, Polymer Testing 26 (2) (2007) 172-179.

98. P. Mertiny, Leakage failure in fibre-reinforced polymer composite tubular vessels at elevated temperature, Polymer Testing 31 (1) (2012) 25-30.

99. J.D. Wolodko, Biaxial fatigue and leakage characteristics of fiber reinforced composite tubes, University of Alberta, 1999. Dissertation.

100. R. Scheuer, P. Mertiny, D. Bormann, Analysis of surface strains and leakage behavior in composite pipes and vessels using digital image correlation technique, in: Proceedings of the ASME 2009 Pressure Vessels and Piping Division Conference, Prague, Czech Republic, 2010, pp. 449-455.

101. J. Bai, P. Seeleuthner, P. Bompard, Mechanical behaviour of ± 55 ° filament-wound glass-fibre/epoxy-resin tubes: I. Microstructural analyses, mechanical behaviour and damage mechanisms of composite tubes under pure tensile loading, pure internal pressure, and combined loading, Composites Science and Technology 57 (2) (1997) 141-153.

102. J.D. Diniz Melo, F. Levy Neto, G. De Araujo Barros, F.N. De Almeida Mesquita, Mechanical behavior of GRP pressure pipes with addition of quartz sand filler, Journal of Composite Materials 45 (6) (2011) 717-726.

103. J. Singer, A simple procedure to compute the sample size needed to compare two independent groups when the population variances are unequal, Statistics in medicine 20 (7) (2001) 1089-1095.

104. D.C. Montgomery, G.C. Runger, Applied Statistics and Probability for Engineers, John Wiley & Sons Ltd, 2010, pp. 351-394.

105. How are FRP/GRP pipe filament winding machine working. Hebei Maple Fiberglass Industry Co.,Ltd. Available at: http://www.frpmachining.com/faqs/frpgrp-pipe-filament-winding-machine. 2013. Last accessed: Jun 1, 2015.

106. V.R. Alferes, Methods of Randomization in Experimental Design, 1st ed, SAGE Publications, 2012, pp. 1-17.

107. F. Ellyin, J.D. Wolodko, Testing facilities for multiaxial loading of tubular specimens, in: Proceedings of the 1995 Symposium on Multiaxial Fatigue and Deformation Testing Techniques, Denver, CO, USA, 1997, pp. 7-24.

108. P. Mertiny, Manufacturing and joining technology of fibre-reinforced composite materials for tubular components under biaxial loading conditions, University of Alberta, 2005. Dissertation.

109. G. Meijer, F. Ellyin, A failure envelope for 60 filament wound glass fibre-reinforced epoxy tubulars, Composites Part A: Applied Science and Manufacturing 39 (3) (2008) 555-564.

110. J.R. Taylor. An Introduction to Error Analysis: The Study of Uncertainties in Physical Measurements. University Science Books. 1997.

111. M. Osako, E. Ito, Simultaneous thermal diffusivity and thermal conductivity measurements of mantle materials up to 10GPa, Institute for Study of the Earth's Interior, 1997.

112. D.C. Montgomery, G.C. Runger, Applied Statistics and Probability for Engineers, John Wiley & Sons Ltd, 2010, pp. 283-344.

113. G.C. Canavos, J.A. Koutrouvelis. Introduction to the Design and Analysis of Experiments. 1st ed. Pearson Education, New York, NY, USA. 2008.

114. S. Kumar, V. Subramanya Sarma, B.S. Murty, A statistical analysis on erosion wear behaviour of A356 alloy reinforced with in situ formed TiB2 particles, Materials Science and Engineering A 476 (1-2) (2008) 333-340.

115. J.M. Chambers, W.S. Cleveland, B. Kleiner, P. Tukey, Graphical methods for data analysis, Wadsworth International Group, 1983, pp. 191-237.

116. J.J. Filliben, The Probability Plot Correlation Coefficient Test for Normality, Technometrics 17 (1) (1975) 111-117.

117. S. Timoshenko, S. Woinowsky-Krieger. Theory of Plates and Shells. 2nd ed. McGraw-Hill, New York, NY, USA. 1959.

118. F. Ellyin, Z. Xia, Y. Chen, Viscoelastic micromechanical modeling of free edge and time effects in glass fiber/epoxy cross-ply laminates, Composites Part A: Applied Science and Manufacturing 33 (3) (2002) 399-409.

119. A. Kaw, Mechanics of Composite Materials: Chapters III-V, 2nd ed, CRC Press, Boca Raton, FL, USA, 2005, pp. 203-293.

120. C. Dong, I.J. Davies, Flexural and tensile moduli of unidirectional hybrid epoxy composites reinforced by S-2 glass and T700S carbon fibres, Materials and Design 54(2014) 893-899.

121. R.S. Lima, S.E. Kruger, B.R. Marple, Towards engineering isotropic behaviour of mechanical properties in thermally sprayed ceramic coatings, Surface and Coatings Technology 202 (15) (2008) 3643-3652.

122. P. Bansal, P.H. Shipway, S.B. Leen, L.C. Driver, Experimental validation of FE predicted fracture behaviour in thermally sprayed coatings, Materials Science and Engineering A 430 (1-2) (2006) 104-112.

123. W.D. Callister. Materials Science and Engineering : An Introduction. 6th ed. Wiley, New York, NY, USA. 2003.

124. F. Azarmi, T. Coyle, J. Mostaghimi, Young's modulus measurement and study of the relationship between mechanical properties and microstructure of air plasma sprayed alloy 625, Surface and Coatings Technology 203 (8) (2009) 1045-1054.

125. K. Ma, J. Zhu, H. Xie, H. Wang, Effect of porous microstructure on the elastic modulus of plasma-sprayed thermal barrier coatings: Experiment and numerical analysis, Surface and Coatings Technology 235(2013) 589-595.

126. S.V. Raj, R. Pawlik, W. Loewenthal, Young's moduli of cold and vacuum plasma sprayed metallic coatings, Materials Science and Engineering A 513-514(2009) 59-63.

127. O. Kovarik, J. Nohava, J. Siegl, Mechanical properties of plasma sprayed alumina coatings, Acta Technica CSAV (Ceskoslovensk Akademie Ved) 48 (2) (2003) 129-145.

128. C. Leither, J. Risan, M. Bashirzadeh, F. Azarmi, Determination of the elastic modulus of wire arc sprayed alloy 625 using experimental, analytical, and numerical simulations, Surface and Coatings Technology 235(2013) 611-619.

129. S. Jordan Liu, Q. Jane Wang, Determination of young's modulus and poisson's ratio of coatings with non-destructive indentation, in: 2005 World Tribology Congress III, September 12, 2005 - September 16, 2005, pp. 741-742.

130. R.S. Lima, S.E. Kruger, G. Lamouche, B.R. Marple, Elastic modulus measurements via laser-ultrasonic and knoop indentation techniques in thermally sprayed coatings, Journal of Thermal Spray Technology 14 (1) (2005) 52-60.

131. M. Eskner, R. Sandstrom, Measurement of the elastic modulus of a plasma-sprayed thermal barrier coating using spherical indentation, Surface and Coatings Technology 177-178(2004) 165-171.

132. W. Tillmann, J. Nebel, Analysis of the mechanical properties of an arc sprayed WC-FeCSiMn coating: Compression, bending, and tension behavior, in: , 2011, pp. 317-327.

133. K. Ma, H. Xie, J. Zhu, H. Wang, Physical and mechanical properties of plasma-sprayed thermal barrier coatings at room and high temperatures, Surface and Coatings Technology 253(2014) 58-67.

134. W. Tillmann, U. Selvadurai, W. Luo, Measurement of the Young's modulus of thermal spray coatings by means of several methods, in: , 2013, pp. 290-298.

135. M.H. Datoo, Mechanics of Fibrous Composites: Chapters I -VI, 1st ed, Springer, Berlin, Germany, 1991, pp. 1-364.

136. J.E. Ashton, J.D. Halphin, P.H. Petit. Primer on Composite Materials: Analysis. 1st ed. Technomic Publishing Company, West Port, CT, USA. 1969.

137. F. Avilés, A.I. Oliva, A. May-Pat, Determination of Elastic Modulus in a Bimaterial Through a One-dimensional Laminated Model, Journal of Materials Engineering and Performance 17 (4) (2008) 482-488.

138. Y. Yang, N. Yao, W.O. Soboyejo, C. Tarquinio, Deformation and fracture in micro-tensile tests of freestanding electrodeposited nickel thin films, Scripta Materialia 58 (12) (2008) 1062-1065.

139. C. Chien, J. Wu, C. Chen, T. Chen, Mechanical characterization of thin film using DIC and inverse approach, in: SEM Annual Conference and Exposition on Experimental and Applied Mechanics 2009, Albuquerque, NM, USA, 2009, pp. 2447-2455.

140. M.A. Sutton, J.J. Orteu, H.W. Schreier. Image Correlation for Shape, Motion and Deformation Measurements: Basic concepts, theory, and applications. Springer, New York, NY, USA. 2009.

141. ASTM D3039M - 08, Test Method for Tensile Properties of Polymer Matrix Composite Materials, West Conshohocken, PA, USA, ASTM International, 2008.

142. Y.-. Wang, C.-. Li, A. Ohmori, Influence of substrate roughness on the bonding mechanisms of high velocity oxy-fuel sprayed coatings, Thin Solid Films 485 (1-2) (2005) 141-147.

143. ASTM E8/E8M - 13a, Standard Test Methods for Tension Testing of Metallic Materials, West Conshohocken, PA, USA, ASTM International, 2013.

144. B. Pan, K. Qian, H. Xie, A. Asundi, Two-dimensional digital image correlation for in-plane displacement and strain measurement: A review, Measurement Science and Technology 20 (6) (2009) .

145. J.G. Eisenhauer, Regression through the Origin, Teaching Statistics 25 (3) (2003) 76-80.

146. D.C. Montgomery, E.A. Peck, G.G. Vining. Introduction to Linear Regression Analysis. 5th ed ed. Wiley, Hoboken, NJ, USA. 2012.

147. System of Equations Solver. Wolfram Research Inc. Available at: http://www.wolframalpha.com/widgets/view.jsp?id=ae438682ce61743f90d4693c497621b7. 2011. Last accessed: July 30, 2015.

148. Solve. Wolfram Research Inc. Available at: https://reference.wolfram.com/language/ref/Solve.html. 2014. Last accessed: July 30, 2015.

149. F. Ahmad, J.O. Dennis, M.H.M. Khir, N.H. Hamid, A. Yar, A new technique to measure the thickness of micromachined structures using an optical microscope, in: 3rd International Conference on Fundamental and Applied Sciences (ICFAS 2014): Innovative Research in Applied Sciences for a Sustainable Future, 2014, pp. 650-6.

150. F.C. Campbell, Structural Composite Materials: Chapter I, 1st ed, ASM International, Russell Township, OH , USA, 2010, pp. 1-30.

151. V.K. Vadlamani, V. Chalivendra, A. Shukla, S. Yang, In situ sensing of non-linear deformation and damage in epoxy particulate composites, Smart Materials and Structures 21 (7) (2012) .

152. J. Ye, Y. Qiu, Z. Zhai, X. Chen, Strain rate influence on nonlinear response of polymer matrix composites, Polymer Composites 36 (5) (2015) 800-810.

153. M. Beghini, G. Benamati, L. Bertini, F. Frendo, Measurement of coating's elastic properties by mechanical methods: Part 2. Application to thermal barrier coatings, Experimental Mechanics 41 (4) (2001) 305-311.

154. S. Yoon, P.J.M. Monteiro, D.E. Macphee, F.P. Glasser, M.S. Imbabi, Statistical evaluation of the mechanical properties of high-volume class F fly ash concretes, Construction and Building Materials 54(2014) 432-442.

155. S. Roy, A. Wanner, Metal/ceramic composites from freeze-cast ceramic preforms: Domain structure and elastic properties, Composites Science and Technology 68 (5) (2008) 1136-1143.

156. M. Alfano, L. Pagnotta, G. Stigliano, G. Di Girolamo, C. Blasi, Measurement of the elastic modulus of ceria yttria co-stabilized zirconia coatings, in: 3rd WSEAS International Conference on Applied and Theoretical Mechanics, Tenerife, Canary Islands, Spain, 2007, pp. 222-227.

157. J. Wang, Young's modulus of porous materials, Journal of Materials Science 19 (3) (1984) 801-808.

158. R. Gonzalez, P. Mertiny, A. McDonald, Damage detection framework for fiber-reinforced polymer composites using Al-12Si flame-sprayed coatings, in: Canadian International Conference on Composite Materials, Edmonton, AB, Canada, 2015, pp. 1-8.

159. N.A. Dolgov, Method for determining the modulus of elasticity for gas thermal spray coatings, Powder Metallurgy and Metal Ceramics 43 (7-8) (2004) 423-428.

160. J.W. Hoover, Transverse cracking of (+,-theta/90(3))(s) composite laminates, University of Alberta, 1999. Dissertation.

161. S. Parhizgar, L.W. Zachary, C.T. Sun, Application of the principles of linear fracture mechanics to the composite materials, International Journal of Fracture 20 (1) (1982) 3-15.

162. M.G. Jenkins, J.P. Piccola, E. Lara-Curzio, Fracture Mechanics of Ceramics: Fatigue, Composites, and High-Temperature Behavior
- Section: Onset of cumulative damage (first matrix cracking) and the effects of test parameters on the tensile behaviour of a continuous fibre-reinforced ceramic composite (CFCC), 1st ed, Springer, Berlin, Germany, 2012, pp. 267-282.

163. J. Wen, Z. Xia, F. Choy, Damage detection of carbon fiber reinforced polymer composites via electrical resistance measurement, Composites Part B: Engineering 42 (1) (2011) 77-86.

164. C. Reale, Size effect on the electrical conductivity and longitudinal gauge factor of thin metal films, Czechoslovak Journal of Physics, Section B 21 (6) (1971) 662-72.

165. Z.H. Meiksin, R.A. Hudzinski, A theoretical study of the effect of elastic strain on the electrical resistance of thin metal films, Journal of Applied Physics 38 (11) (1967) 4490-4494.

166. J.A. Stratton, Electromagnetic Theory : Chapter I, 1st ed, McGraw-Hill, New York, NY, USA, 1941, pp. 14-15.

167. ASTM E41 - 92(2010), Standard Terminology Relating To Conditioning, West Conshohocken, PA, USA, ASTM International, 2010.

168. J.M. Montes, F.G. Cuevas, J. Cintas, Electrical resistivity of metal powder aggregates, Metallurgical and Materials Transactions B: Process Metallurgy and Materials Processing Science 38 (6) (2007) 957-964.

169. M.M. Carroll, Mechanical response of fluid-saturated porous materials, in: XVth International Congress of Theoretical and Applied Mechanics, 1980, pp. 251-62.

170. K.T. Kim, J. Suh, Elastic-plastic strain hardening response of porous metals, International Journal of Engineering Science 27 (7) (1989) 767-778.

171. K. Wunnemann, G.S. Collins, H.J. Melosh, A strain-based porosity model for use in hydrocode simulations of impacts and implications for transient crater growth in porous targets, Icarus 180 (2) (2006) 514-27.

172. H. Gercek, Poisson's ratio values for rocks, International Journal of Rock Mechanics and Mining Sciences 44 (1) (2007) 1-13.

173. J. Berthelot, Transverse cracking and delamination in cross-ply glass-fiber and carbon-fiber reinforced plastic laminates: Static and fatigue loading, Applied Mechanics Reviews 56 (1) (2003) 111-147.

174. C. Li, F. Ellyin, A. Wharmby, A damage meso-mechanical approach to fatigue failure prediction of cross-ply laminate composites, International Journal of Fatigue 24 (2–4) (2002) 429-435.

175. C.L. Chow, F. Yang, A. Asundi, A three-dimensional analysis of symmetric composite laminates with damage, International Journal of Damage Mechanics 2 (3) (1993) 229-45.

176. P.F. Mondragon, A Comparison of Nonlinear Regression Codes, New Mexico Institute of Mining and Technology, 2003. Dissertation.

177. A. Risinger, Implementation of a levenberg-marquardt algorithm to perform regression to I-V curves, in: 39th IEEE Photovoltaic Specialists Conference, PVSC 2013, June 16, 2013 - June 21, 2013, pp. 712-714.

178. G.C. Kuczynski, Effect of elastic strain on the electrical resistance of metals, Physical Review 94(1954) 61-64.

179. J.K.A. Amuzu, E.K. Agyei, A. Hodzoada, Effect of tensile stress on the electrical resistivity of some metallic glasses, Solid State Communications 76 (6) (1990) 769-771.

180. E. Sevkat, J. Li, B. Liaw, F. Delale, A statistical model of electrical resistance of carbon fiber reinforced composites under tensile loading, Composites Science and Technology 68 (10-11) (2008) 2214-2219.

181. K. Diamanti, C. Soutis, Structural health monitoring techniques for aircraft composite structures, Progress in Aerospace Sciences 46 (8) (2010) 342-352.

182. X. Chen, H. Ren, C. Bil, H. Jiang, Synchronizing structural health monitoring with scheduled maintenance of aircraft composite structures, in: International Conference on Concurrent Engineering, CE 2014, September 8, 2014 - September 11, 2014, pp. 813-822.

183. P. Mertiny, C. Hansen, J. Kotlarski, Structural health monitoring using embedded metal filaments in polymer composite piping, in: 2009 ASME Pressure Vessels and Piping Conference, PVP 2009, July 26, 2009 - July 30, 2010, pp. 729-736.

184. Structural health monitoring impact of technology innovations and emerging opportunities, Frost & Sullivan, 2015.

185. U. Tiwari, Civil structural health monitoring using FBG sensors: Trends and challenges, Journal of the Indian Institute of Science 94 (3) (2014) 341-348.

186. X. Li, S. Li, S. Zhong, S. Ge, Comparison analysis of fiber Bragg grating and resistance strain gauge used in quayside container crane structural health monitoring, in: 2nd International Conference on Materials Engineering and Automatic Control, ICMEAC 2013, May 18, 2013 - May 19, 2013, pp. 485-493.

187. R.M. Measures. Structural Monitoring with Fiber Optic Technology. Academic Press, Waltham, MA, USA. 2001.

188. R.C. Foedinger, D.L. Rea, J.S. Sirkis, C.S. Baldwin, J.R. Troll, R. Grande, C.S. Davis, T.L. VanDiver, Embedded fiber optic sensor arrays for structural health monitoring of filament wound composite pressure vessels, Proceedings of SPIE - The International Society for Optical Engineering 3670(1999) 289-301.

189. Y.M. Gebremichael, W. Li, W.J.O. Boyle, B.T. Meggitt, K.T.V. Grattan, B. McKinley, G.F. Fernando, G. Kister, D. Winter, L. Canning, S. Luke, Integration and assessment of fibre Bragg grating sensors in an all-fibre-reinforced polymer composite road bridge, Sensors and Actuators, A: Physical 118 (1) (2005) 78-85.

190. J. Hao, J. Leng, Z. Wei, Non-destructive evaluation of composite pressure vessel by using FBG sensors, Chinese Journal of Aeronautics 20 (2) (2007) 120-123.

191. M. Selezneva, J. Montesano, V. Kulisek, C. Poon, Z. Fawaz, K. Behdinan, Application of FBG sensors to monitor stiffness degradation and damage progression in polymer matrix composites, in: SAMPE 2010 Conference and Exhibition "New Materials and Processes for a New Economy", May 17, 2010 - May 20, 2010, pp. Seattle and Eastern Canada SAMPE Chapters.

192. H. Li, D. Li, G. Song, Recent applications of fiber optic sensors to health monitoring in civil engineering, Engineering Structures 26 (11) (2004) 1647-1657.

193. F. Marazzi, P. Tagliabue, F.M. Corbani, Traditional vs innovative structural health monitoring of monumental structures: A case study, Structural Control and Health Monitoring 18 (4) (2011) 430-449.

194. P. Miller, B. Olateju, A. Kumar, A techno-economic analysis of cost savings for retrofitting industrial aerial coolers with variable frequency drives, Energy Conversion and Management 54 (1) (2012) 81-89.

195. S. Nikoofard, V. Ismet Ugursal, I. Beausoleil-Morrison, Technoeconomic assessment of the impact of window shading retrofits on the heating and cooling energy consumption and GHG emissions of the Canadian housing stock, Energy and Buildings 69 (0) (2014) 354-366.

196. CAD/USD Exchange Rate Lookup. Bank of Canada. Available at: http://www.bankofcanada.ca/rates/exchange/cad-usd-rate-lookup/. 2015. Last accessed: May 1, 2015.

197. SmartScan high perfomance FBG interrogator. opticalfibersensors.org. Available at: http://www.opticalfibersensors.org/products/be-en/1010/detail/item/99903/. 2015. Last accessed: Jun 1, 2015.

198. L. Blank, A. Tarquin. Engineering economy. 6th Ed. ed. McGraw-Hill, New York, NY, USA. 2004.

199. Quarterly Financials for Augusta Industries Inc. MarketWatch. Available at: http://www.marketwatch.com/investing/stock/fbop/financials/income/quarter. 2015. Last accessed: Jun 1, 2015.

200. P.C. Flynn, Financial Management for Engineers, 4th ed, Castle Rock Research Corporation, Edmonton, AB, Canada, 2010, pp. 21-86.

201. D. Leung, Markups in Canada: Have They Changed and Why? Working paper 2008-7, Bank of Canada (2008) .

202. R.K. Rajput, A textbook of electrical technology: Chapters I-II, Laxmi Publications Pvt Ltd, New Delhi, NCT, India, 2004, pp. 1-128.

203. A.P. Godse, U.A. Bakshi, Electronic Devices And Circuits, 2nd revised ed, Technical Publications Pune, Pune, Maharashtra, India, 2009, pp. 3-1-3-98.

204. Regulated Rates for Electricity. Government of Alberta. Available at: http://www.ucahelps.alberta.ca/historic-rates-2014.aspx. 2015. Last accessed: Jun 1, 2015.

205. A. McDonald, G. Fisher. Thermal Spraying for the Oil and Gas Industry. HALGAMM, Edmonton, AB, Canada. 2013.

206. Y.A. Cengel, M. Boles, Thermodynamics - An Engineering Approach: Chapters III-V, McGraw-Hill, Boston, MA, USA, 2006, pp. 1-164.

207. Improving Your Power Factor. Yaskawa Electric Corporation. Available at: https://www.yaskawa.com/pycprd/lookup/getdocument/jvgyvE5ZTUY_5CC1znzBoQiOPjCFHUr9NZDi5wnr0Un3LMj8gZdnbnbTLzxJHMHmmNnHktzgvp2joFXuRTqLb0VkQvmJpD29KTIW8FyLjDQ=. 2013. Last accessed: Jun 1, 2015.

208. Metco 9MC Series Controllers and Metco 9MCD Distribution Unit. Oerlikon Metco. Available at: http://www.oerlikon.com/ecomaXL/files/metco/oerlikon_DSE-0020.3_9MC_EN.pdf&download=1. 2014. Last accessed: Jun 1, 2015.

209. Metco 5MPE Series Powder Feeders. Oerlikon Metco. Available at: http://www.oerlikon.com/ecomaXL/files/metco/oerlikon_DSE-0012.5_5MPE_EN.pdf&download=1. 2014. Last accessed: Jun 1, 2015.

210. Motoman Robots. Yaskawa Motoman Robotics. Available at: http://www.motoman.com/datasheets/Robot%20Series%20Brochure.pdf. 2013. Last accessed: Jun 1, 2015.

211. Best Management Practice - Use of Reinforced Composite Pipe (Non-Metallic Pipelines), Calgary, AB, Canada, Canadian Association of Petroleum Producers, 2009.

212. P.C. Flynn, Financial Management for Engineers, 4th ed, Castle Rock Research Corporation, Edmonton, AB, Canada, 2010, pp. 187-268.

213. Classes of depreciable property. Canada Revenue Agency. Available at: http://www.cra-arc.gc.ca/tx/bsnss/tpcs/slprtnr/rprtng/cptl/dprcbl-eng.html#class46. 2015. Last accessed: Jun 1, 2015.

214. Competitive corporate taxes. Government of Alberta. Available at: http://www.albertacanada.com/business/overview/competitive-corporate-taxes.aspx. 2015. Last accessed: Jun 1, 2015.

215. NDP platform promises to reverse cuts, raise corporate taxes. CBC Radio-Canada. Available at: http://www.cbc.ca/news/elections/alberta-votes/ndp-platform-promises-to-reverse-cuts-raise-corporate-taxes-1.3039816. 2015. Last accessed: Jun 1, 2015.

216. Higher corporate tax rates worked in B.C., critics say. The Edmonton Journal. Available at:

http://www.edmontonjournal.com/Higher+corporate+rates+worked+critics/10926725/story.html. 2015. Last accessed: Jun 1, 2015.

217. I. Fisher. The theory of interest. Porcupine Press, Philadelphia, PA, USA. 1977.

218. Why has Canada's Inflation Target Been Set at 2 Per Cent?. Bank of Canada. Available at: http://www.bankofcanada.ca/wp-content/uploads/2010/11/why_canada_inflation_target.pdf. 2012. Last accessed: Jun 1, 2015.

219. D.S. Remer, A.P. Nieto, A compendium and comparison of 25 project evaluation techniques. I. Net present value and rate of return methods, International Journal of Production Economics 42 (1) (1995) 79-96.

220. G.L. Kutner, Automation in the thermal spray industry, Proceedings of the National Thermal Spray Conference (1991) 647-647.

221. E.V. Vojtsekhovskij, Automated production line for thermal spraying of anti-corrosion coatings on tubular metal structures and pipes, Avtomaticheskaya Svarka (8) (2001) 28-29.

222. Trinco Sandblasting Equipment. Sterling Machinery. Available at: http://www.sterlingmachinery.com/db-files/trinco%20sandblasting%20equipment%20brochure.pdf. 1994. Last accessed: Jun 1, 2015.

Appendix A. Estimation of the complementary direct costs of the FS SHM sensor

The following methods were used to estimate the complementary direct costs of the FS SHM sensor C_{comp} in Eq. (58). Based on these methods, a summary of the complementary cost estimates for the FS SHM sensor is presented in Table A.1.

- **Retail price quoting**

The retail price of off-the-shelf components of the FS SHM sensor, such as the Wheatstone bridge elements, provided a conservative estimate of the end user cost. Retail quotes of the off-the-shelf components were obtained from authoritative North-american suppliers.

- **Material estimation**

The cost of materials used in the fabrication of the FS SHM sensor was estimated using (1) differential weight measurements for non-layered materials (i.e. adhesive, garnet sand, Al-12Si powder, aluminium flux and solder) and (2) length measurements for layered materials (i.e. aluminium tape and masking tape).

The cost of a given non-layered material, C_{mass}, was estimated as follows:

$$C_{\text{mass}} = \frac{w_{\text{m}}}{W_{\text{m}}} \cdot U_{\text{m}} = \frac{(W_2 - W_1)}{W_{\text{m}}} \cdot U_{\text{m}} \tag{81}$$

where, U_{m} is the cost of the unit of purchase (i.e. adhesive cartridge, sandbag, etc.) of the given material, W_{m} is the net weight of the unit of purchase of the given material, W_1 and W_2 are the weights of the FS SHM sensor before and after the integration of the given material, respectively, and $w_{\text{m}}=W_2-W_1$ is the mass of the given material that is incorporated to the FS SHM sensor.

The material cost of a given layered material, C_{length}, was estimated using the following formula:

$$C_{\text{length}} = \frac{l_{\text{m}}}{L_{\text{m}}} \cdot X_{\text{m}} \tag{82}$$

where l_{m} is the length of the given material incorporated into the FS SHM sensor, L_{m} is the total length of the unit of purchase (i.e. roll, sheet, etc.) of the given material, and X_{m} is the cost of the unit of purchase of the given material.

In Eqs. (81) and (82), the values of U_{m} and X_{m} in were based on retail quotes from authoritative North-American suppliers in 2015.

- **Labour time measurement**

The cost of labour was estimated using the time required to reproduce a given manual task by a trained operator. Time measurements were performed using a stopwatch. The labour cost, C_{labour}, was calculated as follows:

$$C_{\text{labour}} = t_{\text{labour}} \cdot U_{\text{labour}} \tag{83}$$

where t_{labour} is the measured operator labour time and U_{labour} is the operator cost per unit of time (i.e. salary per hour). An operator cost of \$16.80 per hour (wage and benefits) was assumed for labour costs included in the complementary direct costs of the FS SHM sensor.

- **AC electricity calculation**

The single-phase alternate current (AC) electrical cost of grit-blasting equipment (48/BP, Trinity Tool Company, Fraser, MI, USA) was estimated using the average AC power dissipated over time. The AC electricity cost of the grit blasting equipment, C_{GritAC}, was estimated using the following expression:

$$C_{\text{GritAC}} = \underline{\underline{P}}_{\text{G}} \cdot t_{\text{on\_G}} \cdot U_{\text{electr}} \tag{84}$$

where $\underline{\underline{P}}_{\text{G}}$, is the real AC power, $t_{\text{on\_G}}$ is the run time of the grit blasting equipment, and U_{electr} is the cost per unit of electricity (\$0.15 per kWh).

Table A.1: Complementary cost estimates of the FS SHM sensor

Cost	Estimation method	Input values	Estimated cost
DP-460 adhesive	Material estimation	U_m= \$24.96 /unit W_m=40.72 g w_m= 4.28 g	\$ 2.62
80-grit garnet sand	Material estimation	U_m= \$7.5x10^{-4}/g W_m=102.43g w_m= 15.53 g	\$ 0.0001
3M 438 Aluminium tape	Material estimation	X_m= \$24.63/roll L_m= 4.6 m l_m= 0.162 m	\$ 0.87
170-10S red plasma masking tape	Material estimation	X_m= \$27.76 /roll L_m= 32.91 m l_m= 1.98 m	\$ 1.67
Grit-blasting electricity	AC electricity calculation	$\underline{\underline{P}}_\mathrm{G}$ = 7.6 kW $t_\mathrm{on\_G}$ = 25.2 s	\$ 0.008
Labour - DP-460 and garnet sand	Labour time measurement	t_labour= 30 min	\$ 8.40
Labour - 3M 438 Aluminium tape	Labour time measurement	t_labour= 30 min	\$ 8.40

Cost	**Estimation method**	**Input values**	**Estimated cost**
Labour - Masking and grit-blasting	Labour time measurement	t_{labour}= 15.5 min	$ 4.34
Labour - Masking for flame spraying	Labour time measurement	t_{labour}= 3 min	$ 0.84
Wheatstone bridge off-the-shelf components	Retail price quoting	Breadboard and jumper wire kit=$12.07 2x10-Ohm resistors=$ 2.88	$ 14.95
Constantan wire	Material estimation	X_{m}= $17.00 /roll L_{m}= 15.24 m l_{m}= 0.15 m	$ 0.17
Aluminium flux	Material estimation	U_{m}=$ 20.50/unit W_{m}= 14.17 g w_{m}= 0.19 g	$ 0.27
Solder	Material estimation	U_{m}= $ 5.43/unit W_{m}=85 g w_{m}=1.25 g	$ 0.08
Labour - Wheatstone bridge	Labour time measurement	t_{labour}= 19 min	$ 5.32